UNIVERSIDADE FERDERAL DE SÃO CARLOS
CENTRO DE CIÊNCIAS EXATAS E DE TECNOLOGIA
DEPARTAMENTO DE QUÍMICA
PROGRAMA DE PÓS-GRADUAÇÃO EM QUÍMICA

DEVELOPMENT OF HEMATITE-BASED PHOTOANODES

MURILLO HENRIQUE DE MATOS RODRIGUES*

Tese apresentada como parte dos requisitos para obtenção do título de DOUTOR EM CIÊNCIAS, área de concentração: FÍSICO-QUÍMICA

Orientador: EDSON ROBERTO LEITE
***Bolsista CAPES**

São Carlos- SP
2023

UNIVERSIDADE FEDERAL DE SÃO CARLOS

Centro de Ciências Exatas e de Tecnologia
Programa de Pós-Graduação em Química

Folha de Aprovação

Defesa de Tese de Doutorado do candidato Murillo Henrique de Matos Rodrigues, realizada em 17/02/2023.

Comissão Julgadora:

Prof. Dr. Edson Roberto Leite (UFSCar)

Profa. Dra. Ana Flávia Nogueira (UNICAMP)

Prof. Dr. Renato Vitalino Gonçalves (IFSC/USP)

Profa. Dra. Lúcia Helena Mascaro Sales (UFSCar)

Prof. Dr. Ernesto Chaves Pereira de Souza (UFSCar)

O Relatório de Defesa assinado pelos membros da Comissão Julgadora encontra-se arquivado junto ao Programa de Pós-Graduação em Química.

My mother Elisabeth Maria de Matos (in memoriam), my father João Célio Rodrigues, my sisters, and all the dear people who accompanied me in the best and worst moments.

“You cannot hope to build a better world without improving the individuals. To that end, each of us must work for his improvement, and at the same time share the general responsibility for all humanity, our particular duty being to those to whom we think we can be most useful.”

Marie Cure

ACKNOWLEDGEMENTS

First of all, I would like to thank GOD for giving me the strength to continue on this journey.

My mother Elisabeth, my father João Célio, and my sisters Mariana and Pietra, for being with me at all times.

To my grandparents for always giving me unconditional love and support. Thanks to all my family for always being there to encourage me.

To my supervisor, Professor Dr. Edson Roberto Leite, for the guidance, support, confidence, encouragement, patience, and opportunity in these years of joint research.

To my friends Carolina Torres, Nicolli de Freitas, João Batista de Souza Jr, Ingrid Rodriguez, Karen Bedin, and Nathalia Verissimo for putting up with me in good and bad times during this time.

To my research group colleagues Danilo Biazon, Cibele Pessan, Rebecca Albers, and Tanna Fiuza for their companionship and friendship.

I am thankful to the friends from UFSCar Fabrício Destro, Larra Kelly, Priscila Barros, and Josiane Carneiro for the good moments in São Carlos.

The Federal University of São Carlos and the National Nanotechnology Laboratory for the necessary infrastructure that made this work possible.

My thanks to all the professionals present at LNNANO/CNPEM for their contribution to my scientific and personal growth throughout the time my research was carried out.

The funding agencies CAPES, CNPq and FAPESP

Thank you all very much!

LIST OF FIGURES

LIST OF SCHEMES

LIST OF TABLES

SUMMARY

DEVELOPMENT OF HEMATITE-BASED PHOTOANODES

Hydrogen production via Water Splitting has been considered one of the best solutions for energy shortages and environmental pollution. The use of hematite (α-Fe_2O_3) as a photoanode in photoelectrochemical hydrogen production processes has been increasingly studied due to its high stability, non-toxicity, absorption in the region up to 600 nm (covering up to 40% of the solar energy spectrum), low bandgap values (between 1.9 - 2.2 eV), high accessibility and low cost, considering that iron is the fourth most abundant element in the Earth's crust. Current density studies show that hematite has a photocurrent of 12.6 mA cm^{-2} under solar irradiation, reaching 16% efficiency in photoelectrochemical processes in water separation. However, it has some limitations in its effectiveness due to low electronic mobility, low electrical conductivity, between 10^{-14} - 10^{-6} $\Omega^{-1}cm^{-1}$, high surface state density, and slow reaction kinetics. Among the methods used for processing the hematite photoanode, we can highlight the thin films from the colloidal deposition of magnetic nanoparticles. This technique leads to the production of high-performance hematite photoanode. However, little is known about the influence of the magnetic field and heat treatment parameters on the final properties of hematite photoanodes. Thus, the first part of the work evaluated how these processing parameters in the morphology and photoelectrochemical properties of nanostructured hematite anodes. The thickness analysis demonstrated a relationship between the magnetic field and the concentration of nanoparticles used to prepare the thin films, showing that larger magnetic fields decrease the thickness. J_{abs}'s results corroborate the existence of the influence of the magnetic field since the use of a larger magnetic field decreases the amount of deposited material, consequently decreasing the optical absorption of thin films. PEC measurements showed that at higher concentrations, using higher magnetic fields increases J_{PH} values, and lower magnetic fields cause a decrease in J_{PH} when using higher concentrations of nanoparticles. Even controlling the thickness and morphology of the iron oxide-based films, the pure material has a high recombination of photogenerated charge due to its low charge separation efficiency, which can generate poor electronic transport, which has hindered its commercial application. Based on the limitations of hematite, the second part of the study was to study germanium as a potentially ideal element that combines improved charge transfer efficiency and

morphology control for high-performance hematite-based photoanode. Intensity-modulated photocurrent spectroscopy (IMPS) results demonstrated that the addition of Ge increased charge mobility, leading to superior charge separation efficiency compared to pure hematite photoanode. C-AFM (Conductive Atomic Force Electron Microscopy) measurements demonstrate that Ge improves electron conductivity and increases majority carrier mobility. Photoelectrochemical measurements performed at different wavelengths show that Ge interferes with the formation of small polarons, making the charges more mobile (delocalized), thus favoring the separation process of photoinduced charges. The synergistic role played by the addition of Ge resulted in a significant improvement in photoelectrochemical performance from 0.5 to 3.2 mA cm^{-2} at 1.23 V_{RHE}, comparing original and Ge-hematite-based photoanodes, respectively.

RESUMO

DESENVOLVIMENTO DE FOTOANODOS A BASE D HEMATITA

A produção de hidrogênio via Water Splitting tem sido considerada uma das melhores soluções para a escassez de energia e poluição ambiental. A utilização da hematita (α-Fe_2O_3) como fotoanodo em processos fotoeletroquímicos de produção de hidrogênio tem sido cada vez mais estudada devido a sua alta estabilidade, não toxicidade, absorção na região de até 600 nm (abrangendo até 40% do espectro de energia solar), baixos valores de bandgap (entre 1,9 - 2,2 eV), alta acessibilidade e baixo custo, considerando que o ferro é o quarto elemento mais abundante na crosta terrestre. Estudos atuais de densidade mostram que a hematita possui uma fotocorrente de 12,6 mA cm^{-2} sob irradiação solar, atingindo 16% de eficiência em processos fotoeletroquímicos na separação de água. No entanto, apresenta algumas limitações em sua eficácia devido à baixa mobilidade eletrônica, baixa condutividade elétrica, entre 10^{-14} - 10^{-6} $\Omega^{-1}cm^{-1}$, alta densidade de estado de superfície e cinética de reação lenta. Dentre os métodos utilizados para o processamento do fotoânodo de hematita, podemos destacar os filmes finos provenientes da deposição coloidal de nanopartículas magnéticas. Esta técnica leva à produção de fotoânodo de hematita de alto desempenho. No entanto, pouco se sabe sobre a influência do campo magnético e dos parâmetros de tratamento térmico nas propriedades finais dos fotoanodos de hematita. Assim, a primeira parte do trabalho avaliou como esses parâmetros de processamento na morfologia e nas propriedades fotoeletroquímicas de ânodos de hematita nanoestruturados. A análise de espessura demonstrou uma relação entre o campo magnético e a concentração de nanopartículas utilizadas para preparar os filmes finos, mostrando que campos magnéticos maiores diminuem a espessura. Os resultados de J_{abs} corroboram a existência da influência do campo magnético, pois a utilização de um campo magnético maior diminui a quantidade de material depositado, diminuindo consequentemente a absorção óptica dos filmes finos. As medições de PEC mostraram que em concentrações mais altas, o uso de campos magnéticos mais altos aumenta os valores de J_{PH}, e campos magnéticos mais baixos causam uma diminuição no J_{PH} ao usar concentrações mais altas de nanopartículas. Mesmo controlando a espessura e morfologia dos filmes à base de óxido de ferro, o material puro possui alta recombinação de carga fotogerada devido a sua baixa eficiência de separação de carga, o que pode gerar transporte eletrônico ruim, o que tem dificultado sua aplicação comercial. Com base nas

limitações da hematita, a segunda parte do estudo foi estudar o germânio como um elemento potencialmente ideal que combina eficiência de transferência de carga aprimorada e controle de morfologia para fotoânodo de alto desempenho à base de hematita. Os resultados da espectroscopia de fotocorrente de intensidade modulada (IMPS) demonstraram que a adição de Ge aumentou a mobilidade da carga, levando a uma eficiência de separação de carga superior em comparação com o fotoânodo de hematita puro. As medições C-AFM (Microscopia eletrônica de força atômica condutiva) demonstram que o Ge melhora a condutividade eletrônica e aumenta a mobilidade dos portadores majoritários. Medidas fotoeletroquímicas realizadas em diferentes comprimentos de onda mostram que o Ge interfere na formação de pequenos polarons, tornando as cargas mais móveis (deslocalizadas), favorecendo assim o processo de separação das cargas fotoinduzidas. O papel sinérgico desempenhado pela adição de Ge resultou em uma melhora significativa no desempenho fotoeletroquímico de 0,5 para 3,2 mA cm^{-2} a 1,23 V_{RHE}, comparando fotoanodos originais e baseados em Ge-hematita, respectivamente.

LIST OF SYMBOLS

J_{PH}	Photocurrent density total
J_{DL}	Photocurrent density obtained to charge separation in the depletion
J_{DIFF}	Photocurrent density obtained to hole diffusion
J_{abs}	Absorbed photocurrent density
V_{fb}	Flat band potential
W	Depletion Layer
E_G	bandgap energy
E_F	Fermi energy
$E_{F\ (solution)}$	Fermi energy for electrolyte solution
h^+	holes
e^-	electrons
q	elementary charge
$\eta_{overall}$	absorption efficiency
V_{RHE}	volts vs. RHE
Nd	donor density
ε_0	permittivity under vacum
ε_r	relative permittivity
μ	mobility
σ	conductivity

LIST OF CONTENDS

Chapter 1

INTRODUCTION

1. AIM AND ORGANIZATION OF THE THESIS

The main goal of this thesis is to explore the development of hematite photoanodes, the preparation method and, the effect of the dopant on the photoelectrochemical performance of these materials compose the two pillars that sustain this thesis, scheme 1.1.

The thesis is divided into four chapters and two appendices. Chapter 1 is a general introduction to the water splitting process, utilized to produce of H_2 and O_2 species. Subsequently, we discuss the use of hematite as a photoanode in this process, discussing the material's structure and properties and the mechanism of charge generation in the electrochemical process.

Chapter 2 focuses on understanding the influence of the magnetic field on colloidal nanoparticle deposition and how the deposition method affects the hematite properties, Scheme 1.1a.

Chapter 3 explores the use of a Germanium as a hematite dopant for the preparation of the photoanodes and how the dopant modifies the hematite, promoting an improvement of the photoelectrochemical performance of the hematite photoanodes, Scheme 1.1b. Furthermore, a new methodology for the doping process of the hematite was studied to compare with a methodology consolidated for the Leite group.

Appendices A and B provide supplementary information to chapters 2 and 3, respectively. Finally, chapter 4 describes the conclusions and an outlook with open questions for further investigations.

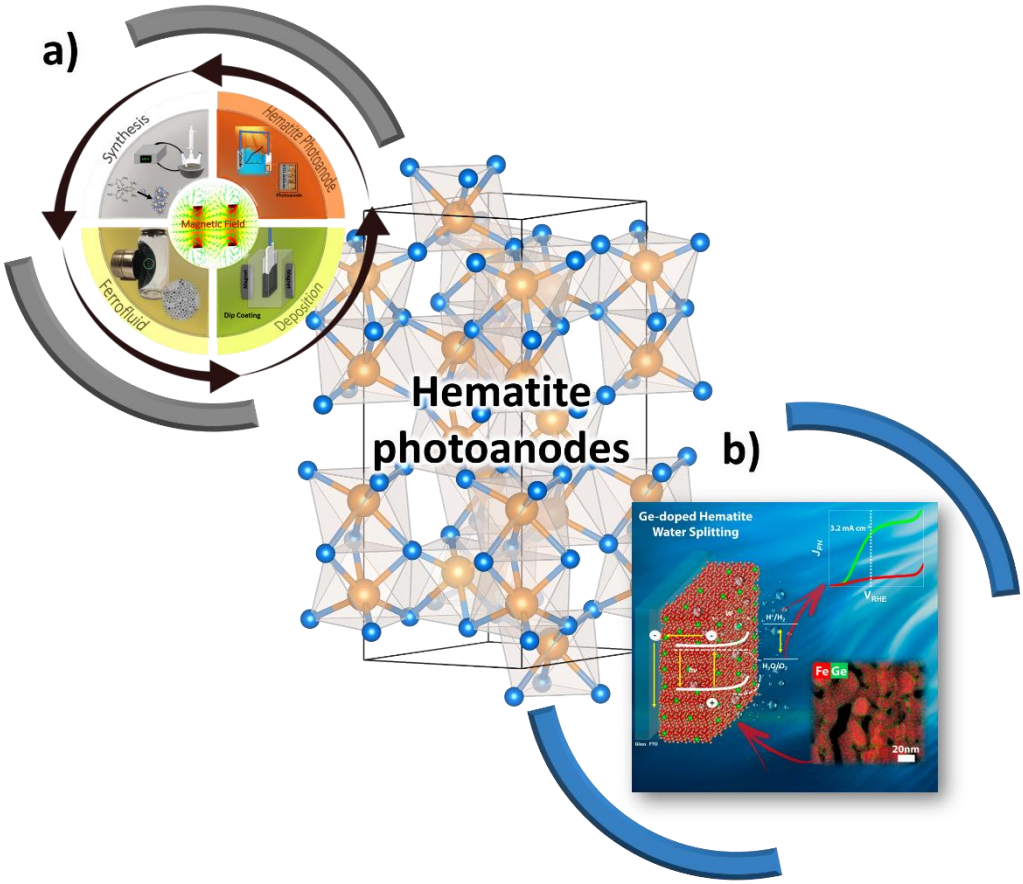

Scheme 1. 1 Organization of the thesis. a) The influence of the magnetic field and nanoparticle concentration on the thin film colloidal deposition process of magnetic nanoparticles: The search for high-efficiency hematite photoanodes. b) Ideal dopant to increase charge separation efficiency in Hematite photoanodes: Germanium.

2. BIBLIOGRAPHIC REVIEW

Currently, one of the world's concerns is the critical energy and environmental crises through the depletion of fossil resources, attenuated climate variation, and dangers associated with the use of nuclear energy. Because of that, there has been an increase in the development of clean projects that seeks to reduce the energy crisis and the environmental impacts generated nowadays. Based on this, renewable energy sources have gained strength in this scenario, and hydrogen has gained attention as a source of energy since it can be obtained from renewable sources and is considered promising. [1-6]

Nowadays, hydrogen production is acquired by two routes. One of them is from fossil sources through the steam reforming of natural gas by partial oxidation of hydrocarbons and coal. The other one, a small amount, is through the electrolysis of alkaline water. So, hydrogen production by renewable methods has intensified due to the

scarcity of fossil sources. However, renewable means commonly have a higher cost when compared to fossil sources. But with the increase in energy demand and technological advances, it is possible to reduce the costs of these processes, such as the use of solar energy, which is considered the most abundant resource of renewable energy, as a precursor for the production of hydrogen. [7-12]

The first report of the formation of hydrogen gas through the water molecule via photoelectrochemical processes was in 1972 by A. Fujishima and K. Honda, using a TiO_2 anode and a platinum cathode, and when the system was illuminated, the formation of both hydrogen gas and oxygen gas. [13-15] Through this result obtained, several researchers became interested in the study of H_2 formation and began the search for new materials capable of improving the yield of the process. In addition to seeking a greater understanding of how it occurred, elucidating what the occurrence of the oxidation of the water molecule requires the presence of a potential difference greater than 1.23V between the two electrodes used in the process, a value which can be equivalent to the energy of radiation with a wavelength of approximately 1000 nm, making it possible to decomposition under visible light in the photoelectrochemical system. [16-21]

2.1. WATER SPLITTING

Water splitting is a process considered thermodynamically unfavorable due to the necessity of photochemical energy to promote the reactions to generate the H2 and O2 molecules, so commonly, photocatalysts are used to help the process. Three components are needed to perform water-splitting: a photoelectrode, an electrolyte, and an external electric circuit. [2,5,17] In terms of the reactional mechanisms, for H_2 generation is necessary two pairs of electrons/holes for each molecule, and four pairs of electrons/holes for each O_2 generation according to electrolyte pH, as demonstrated in the equations below.

For lower pH:

$$2H_2O + 4h^+ \rightarrow 4H^+ + O_2 \quad \text{oxidation reaction} \tag{1.1}$$

$$4H^+ + 4e^- \rightarrow 2H_2 \quad \text{reduction reaction} \tag{1.2}$$

For higher pH:

$$4OH^- + 4h^+ \rightarrow O_2 + 2H_2O \quad \text{oxidation reaction} \tag{1.3}$$

$4H_2O + 4e^- \rightarrow 4OH^- + 2H_2$ reduction reaction (1.4)

The photocatalytic whole is the generation of the charges. In this case, when photoexcited with energy equal to or higher than the bandgap of the material, the electron (e^-) and hole (h^+) charge are generated. The energy provided capable of exciting the electrons from the valence band (VB) to the conduction band (CB) and consequently forming holes in the VB. The charge generation through photoexcitation of the semiconductors is responsible for oxidation and reduction reactions, showed in equations 1.1, 1.2, 1.3, and 1.4 for different pH's. From this idea, several materials began to gain prominence, for having good performance against photoelectrochemical processes, in addition to having low cost, non-toxicity, and high stability, as examples, electrodes made of nanostructured semiconductors of TiO_2, WO_3, $BiVO_4$, Fe_2O_3, SrO_2, ZrO_2, ZnO, CDs, and ZnS. Commonly in the literature, TiO_2 has relevance due to its price and favorable results in the presence of UV irradiation, but its use compared to the use of sunlight has shown lower results than the use of UV because, in the absorption spectrum of this region, sunlight comprises only 5%, increasing the focus on the production of new materials with better responses to the direct use of sunlight.[22-25]

Broadly, new catalysts can be produced by different processes, whether they are capable of improving the properties of these materials, such as surface area of contact; morphology; particle size, which can be related to the results obtained in the degradation process of these compounds. There are numerous methods of synthesis used to obtain catalysts and photocatalysts, among which stand out: method of polymeric precursors; precipitation using carbonates, oxalates, hydroxides; conventional or microwave coupled hydrothermal precipitation and processing; Sol-Gel method; Pechini method; calcination, chemical combustion, thermal decomposition of metallic precursors and hot injection of metallic precursors. [28-32]

2.2. THE HEMATITE (α-Fe2O3) PHOTOANODE

The use of hematite (α-Fe_2O_3) as a photoanode in photoelectrochemical processes for hydrogen production, and water splitting, has been increasingly studied due to its high stability, non-toxicity, absorption in the region of up to 600 nm, covering up to 40% of the spectrum solar energy, low band gap values, between 1.9 - 2.2 eV, in addition to having high accessibility, as it is made of iron considered the fourth most abundant element in the earth's crust. [33-35]

Hematite's structure is formed by octahedrons of Oxygen with iron in the central position. In the (001) direction, pairs of octahedrons share faces, capable to forms Fe_2O_9 structures, shown in Figure 1.1, promoting proximity of the iron atoms leading to a distortion of the octahedron, resulting in two different lengths for the Fe-O bond, a factor in the which reflects on the optical properties of hematite. [36-40]

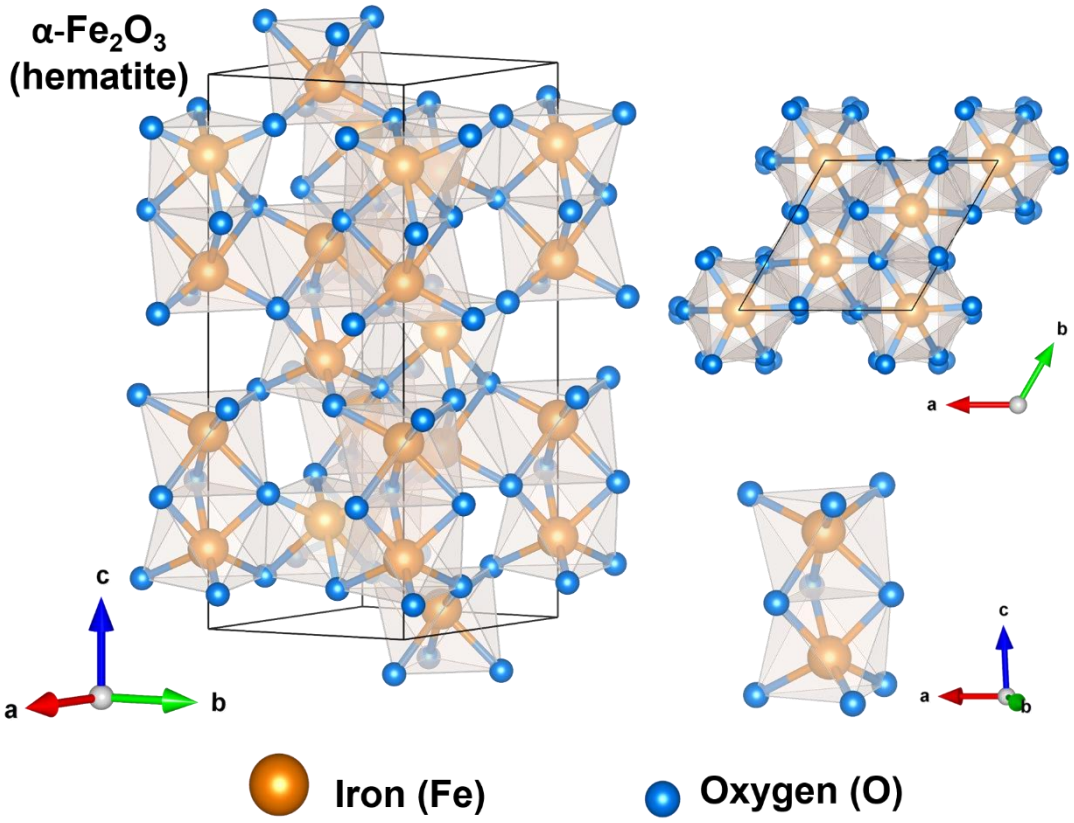

Figure 1. 1 Hematite Crystal structure.

Theoretical studies of current density demonstrate that hematite has 12.6 mA cm^{-2} under solar irradiation, having an efficiency of 16% in photoelectrochemical processes in water splitting, but it has some limitations in its efficiency due to the low mobility of electronic holes, its short half-life, high density of surface states, low response to the oxygen evolution step during photoelectrochemical processes, in addition to a low electrical conductivity between 10^{-14} - 10^{-6} $\Omega^{-1}cm^{-1}$. [40-44] To address these challenges and improve the results of hematite photoanodes, several methodologies have been explored:

Nanostructuring: Nanostructuring hematite photoanodes has been shown to significantly improve their PEC performance. Nanostructuring involves reducing the dimensions of hematite to the nanoscale, typically through methods such as sol-

gel synthesis, hydrothermal synthesis, or electrodeposition. This results in increased surface area, improved light absorption, and reduced charge transport distances, leading to enhanced charge carrier generation and collection efficiency. Nanostructured hematite photoanodes have been shown to exhibit higher photocurrents, lower onset potentials, and improved stability compared to bulk hematite.

Doping: Doping, or the intentional introduction of impurities into the hematite lattice, has been explored as a strategy to modify its properties and improve PEC performance. As mentioned earlier, dopants such as germanium, titanium, silicon, tin, and antimony can be incorporated into hematite to alter its electronic structure, bandgap, and charge transport properties. Dopants can reduce recombination losses, enhance visible light absorption, and improve charge carrier mobility, leading to improved PEC performance.

Co-catalyst deposition: Co-catalyst deposition involves the introduction of a co-catalyst, typically a metal or metal oxide, onto the surface of hematite to facilitate the charge transfer processes at the electrode-electrolyte interface. Co-catalysts can act as electron or hole scavengers, reducing recombination losses and improving charge carrier transfer efficiency. Commonly used co-catalysts for hematite include platinum (Pt), cobalt oxide (CoOx), and nickel oxide (NiOx). Co-catalyst deposition has been shown to significantly enhance the PEC performance of hematite photoanodes by improving the charge transfer kinetics and reducing charge carrier recombination.

Surface passivation: Surface passivation involves the treatment of hematite photoanodes with passivating agents to reduce surface defects and trap states that can lead to charge carrier recombination. Passivating agents can include organic molecules, inorganic salts, or thin films of metal oxides. Surface passivation can improve the charge transport properties of hematite by reducing surface recombination losses and increasing charge carrier lifetimes, resulting in improved PEC performance.

Bandgap engineering: Modifying the bandgap of hematite has been explored as a strategy to enhance its visible light absorption and improve PEC performance. Bandgap engineering can be achieved through various methods such as alloying hematite with other metal oxides, changing the crystal structure, or modifying the electronic structure through doping or strain engineering. Bandgap engineering can broaden the spectral response of hematite, allowing it to absorb a wider range of solar wavelengths and improve its PEC performance under visible light irradiation.

Electrochemical treatments: Electrochemical treatments, such as anodization or electrochemical etching, have been used to modify the surface morphology and properties of hematite photoanodes. Electrochemical treatments can result in the formation of porous or nanostructured hematite films, which can enhance light absorption, improve charge transport properties, and reduce charge carrier recombination. Electrochemical treatments can also be used to deposit co-catalysts or passivating agents onto the hematite surface, further improving its PEC performance.

Tandem configurations: Tandem configurations, where two or more photoactive materials with complementary absorption spectra are combined, have been explored as a strategy to improve the PEC performance of hematite. Hematite has a relatively narrow bandgap, limiting its absorption to the UV region of the solar spectrum. By combining hematite with other photoactive materials that absorb in the visible or near-infrared region, tandem configurations can increase the overall solar absorption and enhance the PEC performance of hematite.

2.3. ELECTROCHEMISTRY OF THE HEMATITE PHOTOANODES

Figure 1.2 shows the VB, CD, Fermi level (E_F), and bandgap energy (E_G) of the hematite photoanode before and after the electrolyte contact, besides the shows the redox states (oxidation (Ox) and reduction (Red)) in solution with their corresponding Fermi level ($E_{F\ (solution)}$). Before the contact between the photoanode and electrolyte (Figure 1.2a), their level bands have different energy. After the contact (Figure 1.2b), an equilibrium occurs between the two materials. The E_F and $E_{F(solution)}$ are aligned due to the internal photovoltage. For this alignmed the VB and CB edges are bent to align with the

interface photoanode/electrolyte. The region of band bending is known as the depletion layer (*W*).

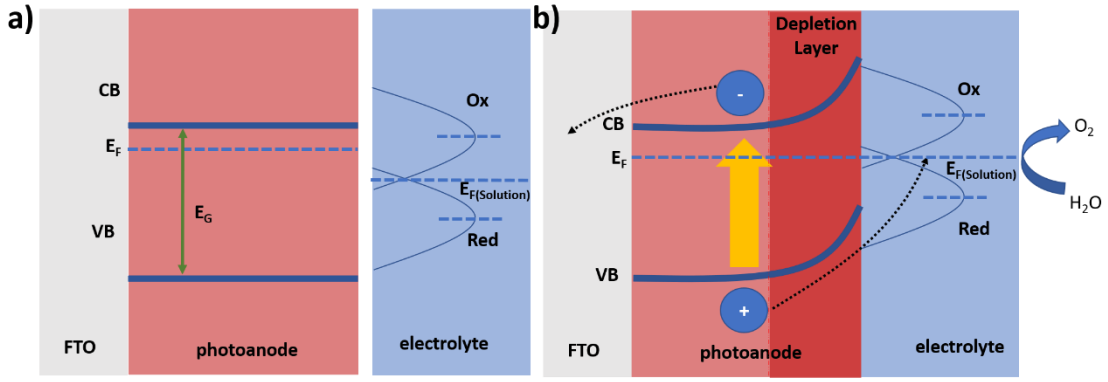

Figure 1. 2 Energy diagram of hematite photoanode and electrolyte solution under a) the contact and b) after the contact under illumination showing the process of charge generation.

The flat band potential (V_{fb}) is the potential before the band bending. The determination of the V_{fb} is possible to carry out studies of the materials ~~used~~, such as the determination of the depletion region and the charge accumulation, analyze the efficiency of the processes, determination of the kinetic parameters of the reactions involved in the charge transfer process being able to compare with different materials to be added and consequently the choice of the best one.

The determination of the V_{fb} is crucial since the V_{fb} can be considered essential parameters used to understand the materials' performance in photogeneration and how to be employed in this process, in addition, to assisting in the determination of energy bands. When the semiconductor is immersed in the electrolyte solution of interest, the flat-band potential is usually determined experimentally using electrochemical and photoelectrochemical methods. Unfortunately, the flat-band potential cannot be measured directly; it is determined indirectly by fitting certain parameters, measurable on the electrode potential scale, to models of the semiconductor/electrolyte interface. Commonly, the V_{fb} is determined experimentally through electrochemical and photoelectrochemical methods and measured indirectly, being necessary for the fitting specific parameters, measurable on the electrode potential scale, to models of the semiconductor/electrolyte interface. [40,48]

Hankin *et al.* [51] demonstrated the use of three different methods to the obtention of the V_{fb}, Mott-Schottky method; Gartner-Butler model; potentiodynamic scan under

chopped illumination; and open circuit electrode potential under high irradiance, and showed that all these methods could be used to determine, and the Gartner-butler presented the best confidence. The Gartner-butler model determines the V_{fb} for the square of the photocurrent as a function of electrode potential in the presence of the hole scavenger utilizing monochromatic irradiation. [52]

In addition to determining the V_{fb}, Gartner-Butler showed the J_{PH} for photoanodes can be expressed according to the equation below.

$$J_{PH} = J_{DL} + J_{DIFF} \tag{1.5}$$

where J_{PH} is the photocurrent density total of the material, J_{DL} is the photocurrent obtained to charge separation in the depletion layer, and J_{DIFF} is the photocurrent density obtained to hole diffusion in the semiconductors. For hematite photoanodes in equation 1.5 the J_{DIFF} as inconsiderate due to the low hole mobility, then the J_{PH} for hematite is governed by a depletion layer region.[52]

2.4. DEPOSITION PROCESS

The deposition process plays a crucial role in the production of hematite (α-Fe_2O_3) photoanodes for photoelectrochemical (PEC) water splitting. Hematite photoanodes are typically fabricated using a variety of deposition techniques, which include:

Physical Vapor Deposition (PVD): PVD is a deposition technique that involves the vaporization of a solid material and subsequent condensation onto a substrate to form a thin film. In the context of hematite photoanodes, PVD techniques such as thermal evaporation and sputtering have been used to deposit hematite thin films onto substrates. These techniques offer precise control over the deposition parameters, such as temperature, pressure, and deposition rate, allowing for the production of thin films with tailored thicknesses and compositions. PVD techniques are particularly suitable for depositing hematite thin films onto conductive substrates, such as fluorine-doped tin oxide (FTO) or indium tin oxide (ITO) coated glass, to create functional PEC electrodes.

Chemical Vapor Deposition (CVD): CVD is a deposition technique that involves the reaction of precursor gases to form a solid film on a substrate. CVD techniques,

such as metal-organic chemical vapor deposition (MOCVD) and plasma-enhanced chemical vapor deposition (PECVD), have been used to deposit hematite thin films onto substrates. CVD techniques offer the advantage of being able to deposit thin films at lower temperatures compared to PVD, which can be beneficial for certain substrate materials that are not thermally stable at high temperatures. CVD techniques also allow for the deposition of complex multi-layered thin films with precise control over the film composition and thickness.

Electrodeposition: Electrodeposition is a deposition technique that involves the use of an electric field to drive the deposition of ions from a solution onto a substrate. In the context of hematite photoanodes, electrodeposition has been used to deposit hematite thin films onto conductive substrates. Electrodeposition offers several advantages, including low cost, ease of scalability, and the ability to deposit thin films with controlled morphology and composition. It also allows for the incorporation of dopants or co-catalysts during the deposition process, which can enhance the PEC performance of hematite photoanodes.

Sol-Gel Method: The sol-gel method is a wet chemical synthesis technique that involves the formation of a colloidal suspension (sol) followed by gelation to form a solid network (gel), which is subsequently heated to form a solid thin film. In the context of hematite photoanodes, sol-gel methods have been used to deposit hematite thin films onto substrates. Sol-gel methods offer several advantages, including the ability to deposit thin films at relatively low temperatures, the ability to easily control the film thickness and composition, and the ability to incorporate dopants or co-catalysts into the film during the synthesis process.

Spray Pyrolysis: Spray pyrolysis is a deposition technique that involves the atomization of a precursor solution into fine droplets, which are then sprayed onto a heated substrate. The solvent evaporates, leaving behind the precursor material, which is subsequently heated to form a solid thin film. In the context of hematite photoanodes, spray pyrolysis has been used to deposit hematite thin films onto substrates. Spray pyrolysis offers several advantages, including the ability to easily scale up the deposition process, the ability to deposit thin films with controlled thickness and composition, and the ability to deposit films on large-area substrates.

Solvothermal Synthesis: Solvothermal synthesis is a wet chemical method that involves the use of high temperature and pressure in a solvent to promote the nucleation and growth of nanoparticles. In the context of hematite photoanodes, solvothermal synthesis has been used to produce hematite nanoparticles with controlled size, shape, and crystallinity. Solvothermal synthesis typically involves the use of precursors, such as iron salts or iron-containing complexes, which are dissolved in a solvent and then heated under controlled conditions to promote the formation of hematite nanoparticles. The resulting nanoparticles can be subsequently collected and deposited onto a suitable substrate to form a hematite photoanode.

Chemical Precipitation: Chemical precipitation is a simple and widely used method for the production of nanoparticles, including hematite nanoparticles. Chemical precipitation involves the reaction of precursor salts with a suitable precipitating agent to form nanoparticles. In the case of hematite, iron salts, such as iron(III) chloride or iron(III) nitrate, can be used as precursors, and a precipitating agent, such as ammonia or sodium hydroxide, can be used to induce the formation of hematite nanoparticles. The resulting nanoparticles can be collected and deposited onto a substrate to form a hematite photoanode.

Co-precipitation: Co-precipitation is a variation of the chemical precipitation method that involves the simultaneous precipitation of two or more precursors to form nanoparticles with controlled composition and properties. In the context of hematite photoanodes, co-precipitation has been used to produce hematite nanoparticles with controlled doping or co-catalyst incorporation. For example, dopant ions or co-catalysts, such as titanium, silicon, tin, or antimony, can be co-precipitated with iron salts to form doped or co-catalyst-containing hematite nanoparticles. The resulting nanoparticles can then be deposited onto a substrate to form a hematite photoanode with improved PEC performance.

Hydrothermal Synthesis: Hydrothermal synthesis is a method that involves the use of high temperature and pressure in a water-based solution to promote the nucleation and growth of nanoparticles. In the context of hematite photoanodes, hydrothermal

synthesis has been used to produce hematite nanoparticles with controlled size, shape, and crystallinity. Hydrothermal synthesis typically involves the use of precursors, such as iron salts or iron-containing complexes, which are dissolved in a water-based solution and then heated under controlled conditions in a sealed container to promote the formation of hematite nanoparticles. The resulting nanoparticles can be collected and deposited onto a substrate to form a hematite photoanode.

2.5. COLLOIDAL DEPOSITION

A colloidal deposition is a popular method for producing hematite (α-Fe2O3) photoanodes using colloidal nanoparticles. Colloidal nanoparticles are small particles suspended in a liquid medium, typically water or an organic solvent, and can be synthesized with controlled size, shape, and composition. Colloidal deposition of hematite nanoparticles offers several advantages for photoanode production. Firstly, it allows for precise control over the size, shape, and composition of the nanoparticles, which can influence the properties of the resulting hematite film. Secondly, colloidal nanoparticles provide a large surface area for enhanced light harvesting and improved charge transport, leading to higher photoelectrochemical performance.

Additionally, the colloidal deposition process is relatively simple, scalable, and compatible with different substrate materials, making it suitable for large-scale production of hematite photoanodes for water-splitting applications. The colloidal deposition process involves the deposition of these nanoparticles onto a substrate to form a thin film or a thick layer of hematite for use in photoanodes. The colloidal deposition process typically involves the following steps:

Synthesis of Colloidal Nanoparticles: Colloidal nanoparticles of hematite are synthesized using methods such as sol-gel synthesis, chemical precipitation, or co-precipitation in a liquid medium. These methods allow for precise control over the size, shape, and composition of the nanoparticles, which can influence the performance of the resulting photoanode. Surface functionalization of the nanoparticles with ligands or surfactants can also be done to improve their stability, dispersion, and adhesion properties during the deposition process.

Preparation of Substrate: The substrate on which the hematite photoanode will be deposited needs to be prepared accordingly. This may involve cleaning the substrate to remove any contaminants, applying a conductive coating or layer (e.g., fluorine-doped tin oxide, FTO) to promote charge transfer, and patterning the substrate if desired.

Deposition of Colloidal Nanoparticles: The colloidal nanoparticles are then deposited onto the substrate using various techniques, such as spin coating, dip coating, spray coating, or drop-casting. In spin coating, the colloidal solution is applied to the substrate, which is then spun at high speeds to uniformly spread the nanoparticles and form a thin film. Dip coating involves immersing the substrate in a colloidal solution and then slowly withdrawing it to deposit the nanoparticles onto the substrate. Spray coating involves spraying the colloidal solution onto the substrate using a spray nozzle, and drop casting involves placing droplets of the colloidal solution onto the substrate and allowing them to evaporate, leaving behind the nanoparticles.

Post-Deposition Treatment: After the colloidal nanoparticles are deposited onto the substrate, post-deposition treatment steps may be employed to enhance the properties of the hematite film. For example, annealing or calcination at high temperatures may be carried out to promote the crystallization of hematite and improve its structural integrity. Annealing can also help in the removal of residual ligands or surfactants from the colloidal nanoparticles, leading to increased electrical conductivity and improved photoelectrochemical performance of the hematite photoanode.

Characterization and Testing: Once the colloidal nanoparticles are deposited and post-deposition treatments are completed, the hematite photoanode can be characterized and tested for its properties and performance. This may involve techniques such as scanning electron microscopy (SEM), X-ray diffraction (XRD), UV-Vis spectroscopy, electrochemical impedance spectroscopy (EIS), and photocurrent-voltage measurements to evaluate the morphology, crystallinity, optical absorption, charge transport, and photoelectrochemical activity of the hematite film.

2.6. USE OF DOPANTS

Dopants are foreign atoms intentionally introduced into the crystal lattice of a material to modify its properties. In the case of hematite photoanodes, dopants can be used to alter the electronic structure, optical properties, and charge transport characteristics of the material, thereby improving its performance as a photoanode in PEC water splitting. The incorporation of dopants into hematite can be achieved through various methods, such as doping during synthesis, post-synthesis doping, or surface modification.

One of the primary motivations for using dopants in hematite photoanodes is to improve their charge transport properties. Hematite is known to have poor electron mobility due to its large bandgap and short electron diffusion length, which results in low charge collection efficiency and high recombination rates. Dopants can be used to modify the electronic structure of hematite, reducing its bandgap and increasing its electron mobility, thus facilitating more efficient charge transport.

Doping with dopants that have a 4+ valence state can modify the electronic structure, charge transport properties, and visible light absorption properties of hematite, which can lead to improved PEC performance. These dopants can introduce intermediate energy levels within the bandgap of hematite, which can facilitate charge carrier transfer and reduce recombination losses, improving the overall charge transport properties. Additionally, doping with these dopants can modify the bandgap of hematite, reducing its energy barrier for light absorption and enhancing its visible light absorption properties, which can result in improved PEC performance.

Tantalum (Ta): Tantalum doping in hematite has been studied as a dopant for improving its PEC performance. Tantalum ions (Ta^{4+}) can substitute for iron ions (Fe^{3+}) in the hematite lattice, forming Ta-doped hematite ($Ta:Fe_2O_3$). Tantalum doping can introduce intermediate energy levels within the bandgap of hematite, which can act as energy states for efficient charge carrier transfer, reducing recombination losses and improving the overall charge transport properties.

Niobium (Nb): Niobium doping in hematite has also been investigated as a dopant for enhancing its PEC performance. Niobium ions (Nb^{5+}) can substitute for iron ions (Fe^{3+}) in the hematite lattice, resulting in the formation of Nb-doped hematite

($Nb:Fe_2O_3$). Niobium doping can modify the electronic structure of hematite, reducing its bandgap and increasing its electron mobility, which can improve its charge transport properties.

Germanium (Ge): Germanium doping in hematite has been studied for its potential to improve the PEC performance of hematite photoanodes. Germanium ions (Ge^{4+}) can substitute for iron ions (Fe^{3+}) in the hematite lattice, forming Ge-doped hematite ($Ge:Fe_2O_3$). Germanium doping can modify the electronic structure of hematite, reducing its bandgap and improving its visible light absorption properties.

Titanium (Ti): Titanium doping in hematite has been investigated as a dopant for enhancing its PEC performance. Titanium ions (Ti^{4+}) can substitute for iron ions (Fe^{3+}) in the hematite lattice, resulting in the formation of Ti-doped hematite ($Ti:Fe_2O_3$). Titanium doping can improve the charge transport properties of hematite by increasing its electron mobility and reducing recombination losses. This can lead to more efficient charge carrier transfer and improved PEC performance.

Silicon (Si): Silicon doping in hematite has also been studied as a dopant for improving its PEC performance. Silicon ions (Si^{4+}) can substitute for iron ions (Fe^{3+}) in the hematite lattice, forming Si-doped hematite ($Si:Fe_2O_3$). Silicon doping can modify the electronic structure of hematite, reducing its bandgap and improving its visible light absorption properties.

Tin (Sn): Tin doping in hematite has been investigated as a dopant for enhancing its PEC performance. Tin ions (Sn^{4+}) can substitute for iron ions (Fe^{3+}) in the hematite lattice, resulting in the formation of Sn-doped hematite ($Sn:Fe_2O_3$). Tin doping can introduce intermediate energy levels within the bandgap of hematite, which can facilitate charge carrier transfer and reduce recombination losses. This can result in improved charge transport properties and enhanced PEC performance.

Antimony (Sb): Antimony doping in hematite has also been studied as a dopant for improving its PEC performance. Antimony ions (Sb^{5+}) can substitute for iron ions (Fe^{3+}) in the hematite lattice, forming Sb-doped hematite ($Sb:Fe_2O_3$). Antimony

doping can modify the electronic structure of hematite, reducing its bandgap and improving its visible light absorption properties.

3. REFERENCES

1. B. Dudley, “BP Statistical Review of World Energy June 2016”, no June, p. 1–48, 2016.

2. T. Hisatomi, J. Kubota, e K. Domen, “Recent advances in semiconductors for photocatalytic and photoelectrochemical water splitting.”, Chem. Soc. Rev., vol. 43, p. DOI: 10.1039/C3CS60378D, 2014.

3. D. a. Wheeler, G. Wang, Y. Ling, Y. Li, e J. Z. Zhang, “Nanostructured hematite: synthesis, characterization, charge carrier dynamics, and photoelectrochemical properties”, Energy Environ. Sci., vol. 5, no 5, p. 6682, 2012.

4. A. G. Tamirat, J. Rick, A. A. Dubale, W.-N. Su, e B.-J. Hwang, “Using hematite for photoelectrochemical water splitting: a review of current progress and challenges”, Nanoscale Horiz., vol. 1, p. 243–267, 2016.

5. M. Gratzel, “Photoelectrochemical cells”, Nature, vol. 414, p. 338–344, 2001.

6. N. M. Rashid, N. Kishi, e T. Soga, “Effects of nanostructures on iron oxide based dye sensitized solar cells fabricated on iron foils”, 2016.

7. F. L. Souza, K. P. Lopes, P. A. P. Nascente, e E. R. Leite, “Nanostructured hematite thin films produced by spin-coating deposition solution: Application in water splitting”, Sol. Energy Mater. Sol. Cells, vol. 93, no 3, p. 362–368, 2009.

8. R. H. Gonçalves, B. H. R. Lima, e E. R. Leite, “Magnetite colloidal nanocrystals: A facile pathway to prepare mesoporous hematite thin films for photoelectrochemical water splitting”, J. Am. Chem. Soc., vol. 133, no 15, p. 6012–6019, 2011.

9. K. Sivula, R. Zboril, F. Le Formal, R. Robert, A. Weidenkaff, J. Tucek, J. Frydrych, M. Grätzel, K. Sivula, R. Zboril, F. Le Formal, R. Robert, A. Weidenkaff, J. Tucek, J. Frydrych, e M. Gra, “Photoelectrochemical Water Splitting with Mesoporous Hematite Prepared by a Solution-Based Colloidal Approach Photoelectrochemical Water Splitting with Mesoporous Hematite Prepared by a Solution-Based Colloidal Approach”, vol. 7444, no 3, p. 7436–7444, 2010.

10. R. H. Goncalves e E. R. Leite, “Nanostructural characterization of mesoporous hematite thin film photoanode used for water splitting”, J. Mater. Res., vol. 29, no 01, p. 47–54, 2013.

11. R. H. Goncalves e E. R. Leite, “The colloidal nanocrystal deposition process: an advanced method to prepare high performance hematite photoanodes for water splitting”, Energy Environ. Sci., vol. 7, no 7, p. 2250– 2254, 2014.
12. V. A. N. De Carvalho, R. A. D. S. Luz, B. H. Lima, F. N. Crespilho, E. R. Leite, e F. L. Souza, “Highly oriented hematite nanorods arrays for photoelectrochemical water splitting”, J. Power Sources, vol. 205, p. 525– 529, 2012.
13. M. R. S. Soares, R. H. Gonçalves, I. C. Nogueira, J. Bettini, A. J. Chiquito, e E. R. Leite, “Understanding the fundamental electrical and photoelectrochemical behavior of a hematite photoanode”, Phys. Chem. Chem. Phys., 2016.
14. Fujishima e K. Honda, “Electrochemical photolysis of water at a semiconductor electrode.”, Nature, vol. 238, no 5358, p. 37–38, 1972.
15. K. Sivula, F. Le Formal, e M. Grätzel, “Solar water splitting: Progress using hematite (a-Fe 2O3) photoelectrodes”, ChemSusChem, vol. 4, no 4, p. 432–449, 2011.
16. V. De, R. Krol, e M. Gratzel, Photoelectrochemical Hydrogen Production.
New York: Springer, 2012.
17. A. Kudo e Y. Miseki, “Heterogeneous photocatalyst materials for water splitting.”, Chem. Soc. Rev., vol. 38, no 1, p. 253–278, 2009.
18. W. Fan, C. Chen, H. Bai, B. Luo, H. Shen, e W. Shi, “Photosensitive polymer and semiconductors bridged by Au plasmon for photoelectrochemical water splitting”, Appl. Catal. B Environ., vol. 195, p. 9–15, 2016.
19. W. D. J. Callister, Ciência e Engenharia dos Materiais, 7 ed. Rio de Janeiro: LTC-Livros Técnicos e Científicos, 2008.
20. A. J. Chiquito e F. Lanciotti Jr., “Super-redes semicondutoras: um laboratório de Mecânica Quântica”, Rev. Bras. Ensino Física, vol. 26, no 4, p. 315–322, dez. 2004.
21. H. J. Song, Y. Sun, and X. H. Jia, “Hydrothermal synthesis, growth mechanism and gas sensing properties of Zn-doped α-Fe2O3 microcubes,” Ceram. Int., vol. 41, no. 10, pp. 13224–13231, 2015.
22 S. Grigorescu, C. Y. Lee, K. Lee, S. Albu, I. Paramasivam, I. Demetrescu, and P. Schmuki, “Thermal air oxidation of Fe: Rapid hematite nanowire growth and photoelectrochemical water splitting performance,” Electrochem. commun., vol. 23, no. 1, pp. 59–62, 2012.
23. Z. Zhang, M. F. Hossain, and T. Takahashi, “Self-assembled hematite (??-Fe2O3) nanotube arrays for photoelectrocatalytic degradation of azo dye under simulated solar light irradiation,” Appl. Catal. B Environ., vol. 95, no. 3–4, pp. 423–429, 2010.

24. C. Zhu, C. Li, M. Zheng, and J. J. Delaunay, “Plasma-Induced Oxygen Vacancies in Ultrathin Hematite Nanoflakes Promoting Photoelectrochemical Water Oxidation,” ACS Appl. Mater. Interfaces, vol. 7, no. 40, pp. 22355–22363, 2015.
25. R. Rajendran, Z. Yaakob, M. Pudukudy, M. S. A. Rahaman, and K. Sopian, “Photoelectrochemical water splitting performance of vertically aligned hematite nanoflakes deposited on FTO by a hydrothermal method,” J. Alloys Compd., vol. 608, pp. 207–212, 2014.
26. C. Colombo, G. Palumbo, E. Di Iorio, X. Song, Z. Jiang, Q. Liu, and R. Angelico, “Influence of hydrothermal synthesis conditions on size, morphology and colloidal properties of Hematite nanoparticles,” Nano- Structures and Nano-Objects, vol. 2, pp. 19–27, 2015.
27. Q. Meng, Z. Wang, X. Chai, Z. Weng, R. Ding, and L. Dong, “Fabrication of hematite (α-Fe2O3) nanoparticles using electrochemical deposition,” Appl. Surf. Sci., vol. 368, pp. 303–308, 2016.
28. M. Tadic, M. Panjan, V. Damnjanovic, and I. Milosevic, “Magnetic properties of hematite (a-Fe2O3) nanoparticles prepared by hydrothermal synthesis method.,” Appl. Surf. Sci., vol. 320, pp. 183– 187, 2014.
29. C. Wu, P. Yin, X. Zhu, C. OuYang, and Y. Xie, “Synthesis of hematite (alpha-Fe2O3) nanorods: diameter-size and shape effects on their applications in magnetism, lithium ion battery, and gas sensors.,” J. Phys. Chem. B, vol. 110, no. 36, pp. 17806–12, Sep. 2006.
30. C. Wu, P. Yin, X. Zhu, C. OuYang, and Y. Xie, “Synthesis of hematite (alpha-Fe2O3) nanorods: diameter-size and shape effects on their applications in magnetism, lithium ion battery, and gas sensors.,” J. Phys. Chem. B, vol. 110, no. 36, pp. 17806–12, Sep. 2006.
31. Z. Li, X. Lai, H. Wang, D. Mao, C. Xing, and D. Wang, “Direct hydrothermal synthesis of single-crystalline hematite nanorods assisted by 1,2-propanediamine.,” Nanotechnology, vol. 20, p. 245603, 2009.
32. H. K. Mulmudi, N. Mathews, X. C. Dou, L. F. Xi, S. S. Pramana, Y. M. Lam, and S. G. Mhaisalkar, “Controlled growth of hematite (??-Fe2O3) nanorod array on fluorine doped tin oxide: Synthesis and photoelectrochemical properties,” Electrochem. commun., vol. 13, no. 9, pp. 951–954, 2011.
33. V. A. N. De Carvalho, R. A. D. S. Luz, B. H. Lima, F. N. Crespilho, E. R. Leite, and F. L. Souza, “Highly oriented hematite nanorods arrays for photoelectrochemical water splitting,” J. Power Sources, vol. 205, pp. 525–529, 2012.

34. P. V Adhyapak, U. P. Mulik, D. P. Amalnerkar, and I. S. Mulla, “Low Temperature Synthesis of Needle-like alpha-FeOOH and Their Conversion into alpha-Fe2O3 Nanorods for Humidity Sensing Application,” J. Am. Ceram. Soc., vol. 96, no. 3, pp. 731–735, 2013.

35. Gurudayal, S. Y. Chiam, M. H. Kumar, P. S. Bassi, H. L. Seng, J. Barber, and L. H. Wong, “Improving the efficiency of hematite nanorods for photoelectrochemical water splitting by doping with manganese.,” ACS Appl. Mater. Interfaces, vol. 6, no. 8, pp. 5852–9, Apr. 2014.

36. T. S. Atabaev, “Facile hydrothermal synthesis of flower-like hematite microstructure with high photocatalytic properties,” J. Adv. Ceram., vol. 4, no. 1, pp. 61–64, 2015.

37. J. Y. Kim, G. Magesh, D. H. Youn, J.-W. Jang, J. Kubota, K. Domen, and J. S. Lee, “Single-crystalline, wormlike hematite photoanodes for efficient solar water splitting.,” Sci. Rep., vol. 3, p. 2681, 2013.

38. F. Zhang, H. Yang, X. Xie, L. Li, L. Zhang, J. Yu, H. Zhao, and B. Liu, “Controlled synthesis and gas-sensing properties of hollow sea urchinlike ??-Fe2O3 nanostructures and ??-Fe2O3 nanocubes,” Sensors Actuators, B Chem., vol. 141, no. 2, pp. 381–389, 2009.

39. S. Shen, J. Zhou, C.-L. Dong, Y. Hu, E. N. Tseng, P. Guo, L. Guo, and S. S. Mao, “Surface engineered doping of hematite nanorod arrays for improved photoelectrochemical water splitting.,” Sci. Rep., vol. 4, p. 6627, 2014.

40. S. S. Shinde, R. a Bansode, C. H. Bhosale, and K. Y. Rajpure, “Physical properties of hematite α-Fe 2 O 3 thin films: application to photoelectrochemical solar cells,” J. Semicond., vol. 32, no. 1, p. 13001, 2011.

41. S. Grigorescu, C. Y. Lee, K. Lee, S. Albu, I. Paramasivam, I. Demetrescu, and P. Schmuki, “Thermal air oxidation of Fe: Rapid hematite nanowire growth and photoelectrochemical water splitting performance,” Electrochem. commun., vol. 23, no. 1, pp. 59–62, 2012.

42. K. Sivula, F. Le Formal, M. Grätzel, Solar water splitting: progress using hematite (A-Fe2O3) photoelectrodes, ChemSusChem 4 (2011) 432–449.

43. C. Li, Z. Luo, T. Wang, J. Gong, Surface, bulk, and interface: rational design of hematite architecture toward efficient photo-electrochemical water splitting, Adv. Mater. 30 (2018) 1707502.

44. O. Zandi, T.W. Hamann, The potential versus current state of water splitting with hematite, Phys. Chem. Chem. Phys. 17 (2015) 22485–22503.

45. X. Zhang, A. Bieberle-Hütter, Modeling and simulations in photoelectrochemical water oxidation: from single level to multiscale modeling, ChemSusChem 9 (2016) 1223–1242.
46. S. Nicola, Ab initio simulations of water splitting on hematite, J. Phys.: Condens. Matter 29 (2017) 463002.
47. M.E. McBriarty, J.E. Stubbs, P.J. Eng, K.M. Rosso, Potential-specific structure at the hematite-electrolyte interface, Adv. Funct. Mater. 28 (2018) 1705618.
48. D.A. Grave, N. Yatom, D.S. Ellis, M.C. Toroker, A. Rothschild, The "Rust" challenge: on the correlations between electronic structure, excited state dynamics, and photoelectrochemical performance of hematite photoanodes for solar water splitting, Adv. Mater. 30 (2018) 1706577.
49. P. Liao, E.A. Carter, Testing variations of the GW approximation on strongly correlated transition metal oxides: hematite (A-Fe2O3) as a benchmark, Phys. Chem. Chem. Phys. 13 (2011) 15189–15199.
50. P. Merchant, R. Collins, R. Kershaw, K. Dwight, A. Wold, The electrical, optical and photoconducting properties of Fe2−XCrxO3 (0≤X≤0.47), J. Solid State Chem. 27 (1979) 307–315.
51. Hankin, A.; Bedoya-Lora, F. E.; Alexander, J. C.; Regoutz, A.; Kelsall, G. H., Flat band potential determination: avoiding the pitfalls. Journal of Materials Chemistry A 2019, 7 (45), 26162-26176.
52. Butler, M. A.; Ginley, D. S., Temperature dependence of flatband potentials at semiconductor–electrolyte interfaces. Nature 1978, 273 (5663), 524-525.

Chapter 2

The influence of the magnetic field and nanoparticle concentration on the thin film colloidal deposition process of magnetic nanoparticles: The search for high-efficiency hematite photoanodes

Murillo H. M. Rodrigues, [a,b] João B. Souza Junior, [b] Edson R. Leite [a,b*]

[a]Department of Chemistry, Federal University of São Carlos, Via Washington Luiz, km 235, São Carlos, SP, 13565-905, Brazil

[b]Brazilian Nanotechnology National Laboratory (LNNano), Brazilian Center for Research in Energy and Materials (CNPEM), Campinas, São Paulo, 13083-970, Brazil.

This chapter was published in:

Nanomaterials, **2022**, *12*, 1636. https://doi.org/10.3390/nano12101636

Supplementary Information is attached in Appendix A in Chapter 5.

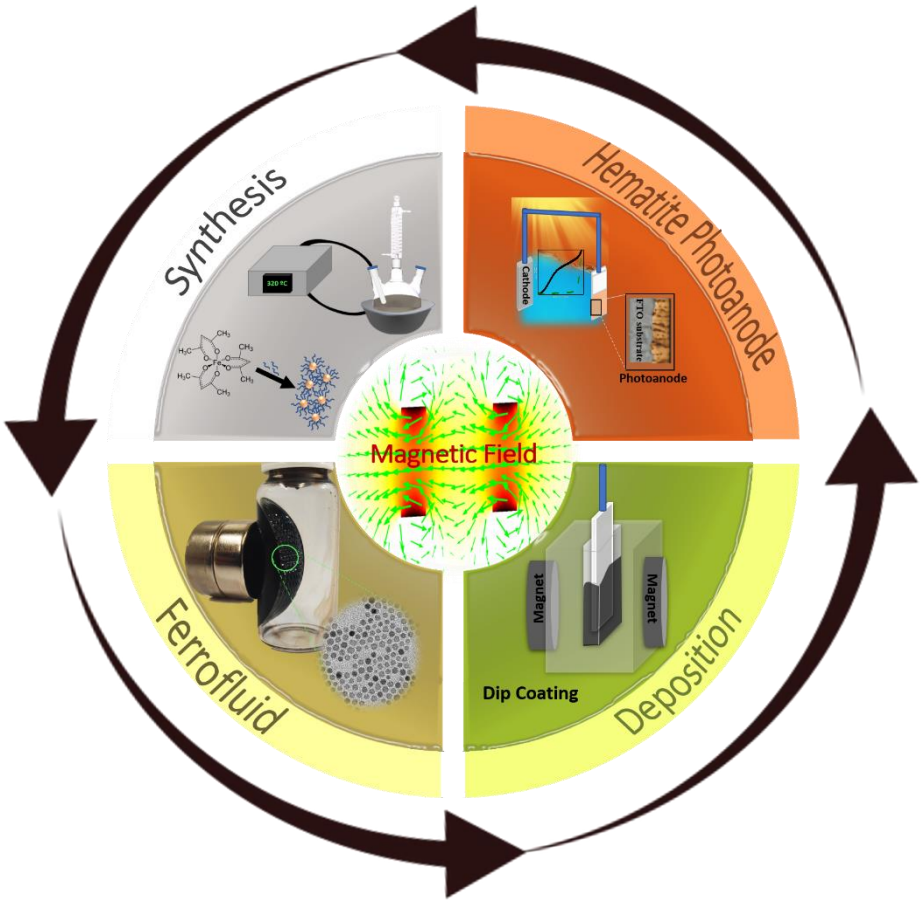

1. ABSTRACT

Hematite is considered a promising photoanode material for photoelectrochemical water splitting, and the literature has shown that the photoanode production process has an impact on the final efficiency of hydrogen generation. Among the methods used to process hematite photoanode, we can highlight the thin films from the colloidal deposition process of magnetic nanoparticles. This technique leads to the production of high-performance hematite photoanode. However, little is known about the influence of the magnetic field and heat treatment parameters on the final properties of hematite photoanodes. Here, we will evaluate those processing parameters in the morphology and photoelectrochemical properties of nanostructured hematite anodes. The analysis of thickness demonstrated a relationship between the magnetic field and nanoparticles concentration utilized to prepare the thin films, showing that the higher magnetic fields decrease the thickness. The J_{abs} results corroborate to influence of the magnetic field since the use of a higher magnetic field decreases the deposited material amount, consequently decreasing the absorption of the thin films. The PEC measurements showed that at higher concentrations, the use of higher magnetic fields increases the J_{PH} values, and lower magnetic fields cause a decrease in J_{PH} when using the higher nanoparticle concentrations.

2. INTRODUCTION

With the development of hematite (α-Fe_2O_3) photoanodes for photoelectrochemical cell (PEC) devices, the use of inexpensive, naturally abundant, and electrochemically stable materials can become a reality.[1,2] Recently, considerable progress was made in the improvement of hematite photoanodes for promoting water photoelectrolysis via sunlight.[3] For instance, for a columnar hematite photoanode, a photocurrent as high as 6 mA cm^{-2} was reported.[4] However, despite recent advancements, further research is essential to extract the full potential of hematite photoanodes and establish this material as a viable alternative for producing hydrogen (H_2) by applying PEC water splitting.

The technique of tuning the nanostructure of hematite thin films to enhance PEC performance is documented in the literature.[5] Although several methods for producing hematite thin films are reported, the colloidal nanoparticle deposition (CND) technique has demonstrated the most promising results.[6,7] In contrast to methods that require an iron precursor or compound (molecular or salt compounds) for producing the hematite phase above a transparent conducting oxide (TCO) substrate, such as atmospheric pressure chemical vapor deposition (APCVD)[8], atomic layer chemical vapor deposition[4], the Pechini method[9], electrochemical deposition[10], and hydrothermal synthesis, the CND method utilizes iron oxide nanoparticles in the preparation of PEC. This process generally involves the thermal treatment of nanoparticles to generate a hematite structure, followed by adhesion to the TCO substrate.

The overall process involves three steps: the synthesis of the iron oxide colloidal solution, the deposition of nanoparticles onto the TCO substrate, and high-temperature sintering. Iron-oxide nanoparticles of different sizes, shapes, size distributions, and surface chemical compositions can be synthesized using various techniques. In addition, the crystallographic structure of iron oxide nanoparticles can undergo a phase transformation from Fe_3O_4 ($Fe^{+2}O, Fe_2^{+3}O_3$, magnetite) to γ-Fe_2O_3 (maghemite). This adaptability in adjusting the iron oxide precursor for the production of hematite PEC makes the CND method a candidate for achieving the desired maximum photocurrent extraction for water splitting. The obtained colloidal solution can be deposited using various techniques, typically spin or dip coating, and the final PEC is obtained by thermally treating the nanoparticles as deposited.

Sivula *et al.*[7] were the first to prepare hematite photoanode thin films using the CND method and reported a strong dependence of the photocurrent on the sintering

temperature. Gonçalves *et al.*[6] developed an alternative method for preparing hematite photoanodes using the CND process. Magnetite nanocrystals were used as a precursor to producing a hematite photoanode by oxidizing the magnetite structure to hematite at high temperatures. After sintering was performed at 820 °C, the hematite photoanode exhibited a homogeneous orange transparent film in which no magnetite remained.

In 2014, Leite *et al.*[11] devised an innovative route for producing nanostructured hematite thin films by coupling the CND method with a magnetic field. This method involved the use of two permanent magnets outside the colloidal magnetite solution to generate a static ferrofluid, and the TCO substrate was deposited via dip coating. Thus, columnar hematite films with a textured orientation in the <110> direction were produced, exhibiting exceptional photoelectrochemical properties.[11] This innovative deposition method was employed to demonstrate that hematite thin films with thicknesses ranging from 30 to 300 nm can be tailored.

In contrast to the multiple reported deposition processes for increasing the film thickness, the magnetite colloidal solution technique employs a single deposition and sintering cycle to achieve a thickness of 300 nm.[11] However, the parameters of the CND method employing magnetic nanoparticles aided by a magnetic field to produce hematite nanostructures are not yet fully understood. For example, how the concentration of nanoparticles and the strength of the magnetic field affect the morphological properties of hematite thin films (thickness, degree of texturing, and optical and electrochemical properties) is unclear. Here, we intend to expand on our understanding of this technique and determine the roles of the magnetic field, nanoparticle concentration in the film morphology, and photoelectrochemical performance of the hematite photoanodes.

3. MATERIALS AND METHODS

3.1. SYNTHESIS OF MAGNETITE NANOPARTICLES

Magnetite nanoparticles (Fe_3O_4) were synthesized by dissolving 3 mmol of iron acetylacetonate (III) (Aldrich Chemical 99.99%) in 35 mL of oleylamine (Aldrich Chemical 70%, St. Louis, MO, USA) in a three-necked round-bottomed flask (100 mL). The solution was initially heated to 100 °C for 30 min under a vacuum. Subsequently, the temperature was raised to 320 °C for 1 h in an N_2 atmosphere. After the reaction was complete, the colloidal solution was allowed to cool to room temperature. The magnetite nanoparticles were washed with acetone, ethanol, and isopropyl alcohol. Finally, the

nanoparticles were redispersed in toluene, yielding colloidal dispersions with varying concentrations (150, 300, 400, and 500 mg mL^{-1}).

3.2. THIN FILM PREPARATION

Commercial FTO substrates used in this study were manufactured by Solaronix (F-doped SnO_2 transparent conductor oxide layer deposited in an aluminum–boron–silicate glass with a typical size of 2 cm × 1 cm) and employed in the film deposition process. Before deposition, the FTO substrate was cleaned with soap, isopropyl alcohol, acetone, and toluene and stored in toluene.

The colloidal magnetite solution was deposited on FTO by applying dip-coating assisted by a magnetic field, as shown in Figure 2.1. Two magnets were separated by 2.7 cm, 5.6 cm, and 7.9 cm in a Teflon container, and 1 mL of colloidal solution was loaded into the container (see scheme in Figure 2.1). The obtained ferrofluid was used to tune the CND process using three different magnetic fields by varying the distance between the two magnets. The magnetic fields were then simulated using COMSOL Multiphysics software[12] to obtain the approximate strength used in the experiments. Round neodymium iron boron magnets with a remanence of 12.1 kG (Magtek, São Caetano do Sul, Brazil, the diameter of 25 mm × 10 mm, N35) were used in the simulation. The applied magnetic fields were 5, 15, and 50 mT.

The films were produced by controlling the dip-coating parameters, such as immersion speed (60 mm min^{-1}) and withdrawal speed (60 mm min^{-1}), but not the immersion permanence time. The deposited films were then sintered for 20 min at 850 °C in a tubular furnace. The substrate was then swiftly removed and cooled to room temperature.

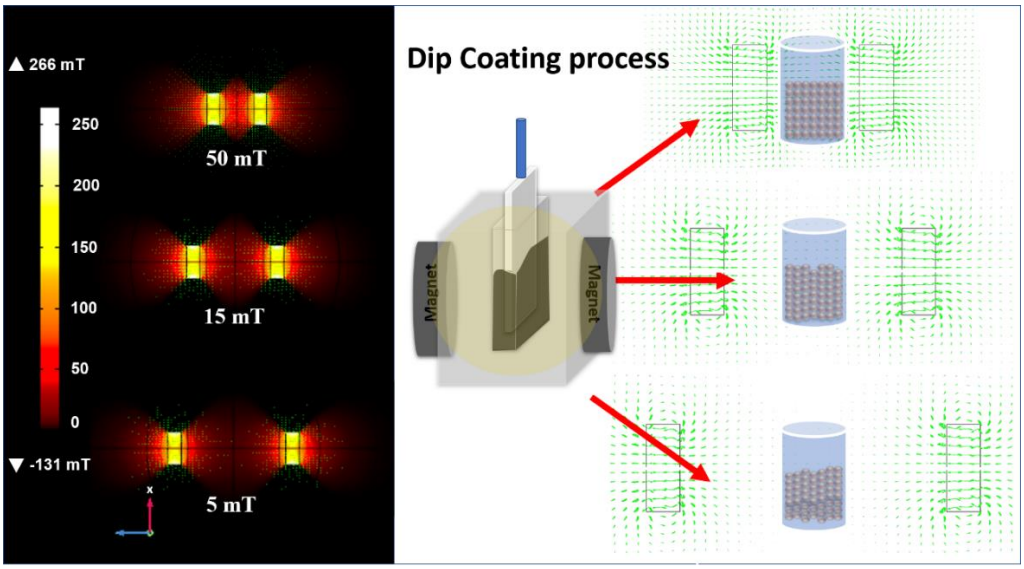

Figure 2.1. Magnetic field simulation was applied in the process of deposition of the magnetite nanoparticles by dip-coating.

3.3. CHARACTERIZATION

The thin films were characterized by X-ray diffraction (XRD, Bruker (Billerica, MA, USA), D8 Advance ECO) using CuKα radiation (λ = 0.15406 nm), a linear detector LYNXEYE XE (PSD of 2.948°), primary optics (2.5° axial soller and 0.6 mm slit), and secondary optics (2.5° axial soller and 5.4 mm slit). Transmission electron microscopy (TEM) was performed at 300 kV using a JEOL JEM 2100F instrument (Tokyo, Japan). The TEM sample was prepared by in situ milling using a focused ion beam system. The film thickness was determined using field-emission scanning electron microscopy (FESEM; F50 INSPECT, FEI, Hillsboro, OR, USA).

3.4. PHOTOELECTROCHEMICAL CHARACTERIZATION

Photoelectrochemical measurements were performed in a standard three-electrode cell with the hematite film as the working electrode (0.28 cm^2 area), Ag/AgCl in a saturated KCl solution as the reference electrode, and a platinum plate as the counter electrode. A 1.0 M NaOH solution (NaOH ACS Aldrich, 99.99%, St. Louis, MO, USA) in highly pure water (pH = 13.6, at 25 °C) was used as the electrolyte. A scanning potentiostat (potentiostat/galvanostat μAutolab III, Metrohm, Herisau, Switzerland) with a 20 mV s^{-1} scan rate was used to measure the dark and illuminated currents. A 250 W ozone-free xenon lamp (Osram, Munich, Germany) and an AM 1.5 filter were used to simulate sunlight (100 mW cm^{-2}) (Newport Corp., Irvine, CA, USA).

4. RESULTS

4.1. NANOPARTICLES SYNTHESIS

Thermal decomposition of a $Fe(acac)_3$ precursor in oleylamine as a solvent and ligand agent produced magnetite nanoparticles. $Fe(acac)_3$ decomposition and Fe_3O_4 nanoparticle nucleation occurred at 170 °C.[13] The presence of excess oleylamine stimulated the formation of a strong reducing environment, which was sufficient to partially reduce the Fe^{3+} cations to Fe^{2+}, resulting in the formation of magnetite. XRD data were easily classified as cubic *fcc* (inverse spinel structure, $Fd\bar{3}m$ (Figure A1), based on magnetite norms (JCDPS Card no. 19-0629).[14] Rietveld refinement (Figure A1 and Table A1) was performed utilizing the TOPAS software 5.4 (Bruker), yielding a refined lattice parameter of a = 8.378 Å, which is close to the observed standard parameter in the literature (a = 8.396 Å). Comparatively, the maghemite structure (a = 8.3461 Å, JCDPS Card no. 39-1346), which contains only Fe^{2+} cations, has a lower lattice parameter than the magnetite nanoparticles synthesized in this study. This result indicated the presence of both Fe^{2+} and Fe^{3+} in the formation of magnetite. According to the literature, oleylamine acts as a reducing agent for Fe^{3+} cations but is very effective at forming crystalline structures in the presence of iron in two valence states, as determined by XRD.[14]

Transmission electron microscopy (TEM) was used to analyze the nanoparticle size, size distribution, structure, and morphology. Figure 2.2a,b display micrographs and size distribution histograms depicting the formation of nanoparticles with uniform morphology and diameter of approximately 7.6 nm (D_{TEM}). The selected area electron diffraction (SAED) patterns (Figure 2.2c) reveal diffraction rings typical of polycrystalline nanoparticles, which correspond to crystallographic planes indexed with Miller indices (*hkl*) of the magnetite phase. This result confirms the XRD measurements of magnetite nanoparticles. For a comparison with D_{XRD_r}, the nanoparticle diameter D_{TEM} must be interpolated using a number-weighted log-normal distribution. The volume-weighted mean diameter D_{XRD_v} was computed according to Equation (1.1), as the XRD-obtained particle size was derived from volumetric diffraction data.[15]

$$D_{TEM\_V} = D_{TEM} e^{3(\sigma_{D_{TEM}})^2} \quad (1.1)$$

where, $\sigma_{D_{TEM}}$ is the standard deviation of the log-normal distribution. Then, D_{TEM_V} = 7.9 nm was calculated and compared to D_{XRD_r} (7.8 nm), revealing an error of less than 2%

between the two diameters, correlating the morphological D_{TEM} with the volumetric D_{XRD}. This comparative result demonstrates that the magnetite nanoparticle region is predominantly made up of single-crystalline particles, *i.e.*, each nanoparticle has a low crystallographic defect concentration and could be referred to as a nanocrystal.

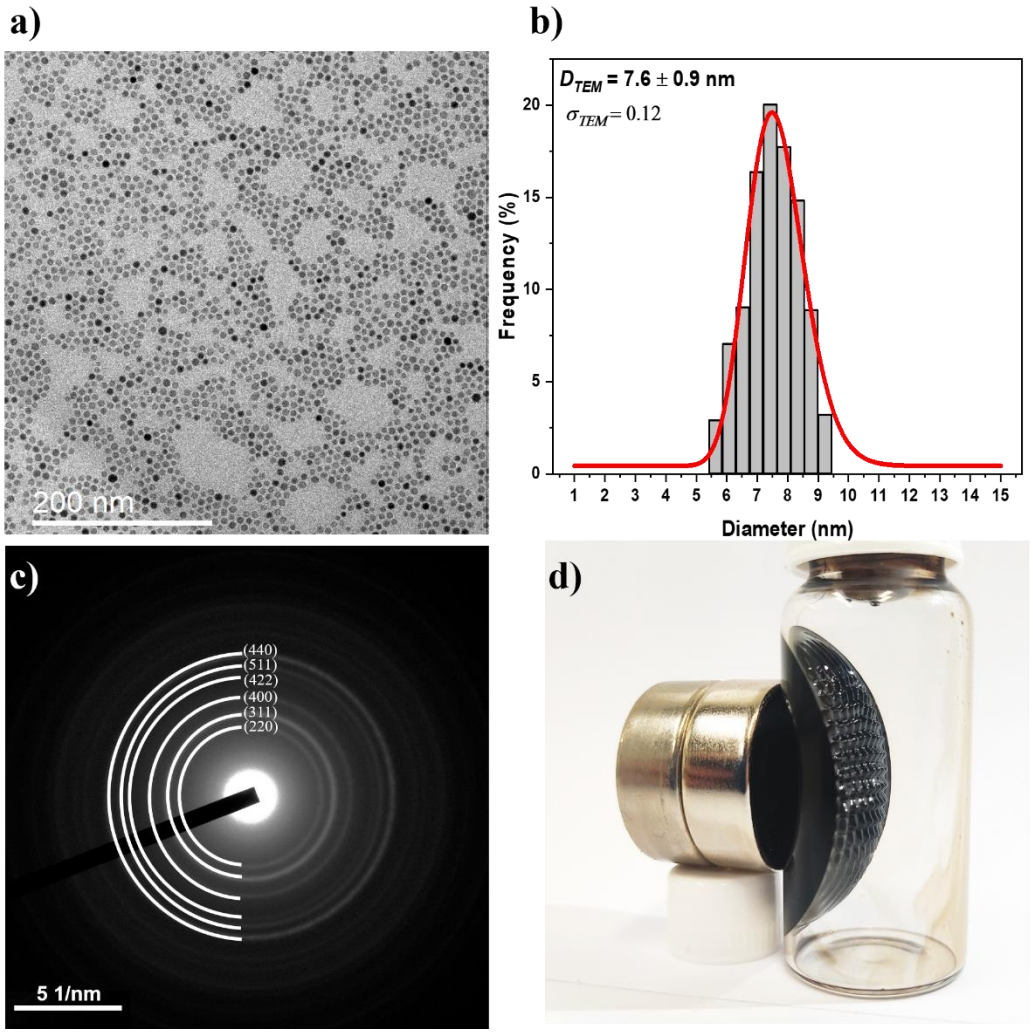

Figure 2.2. TEM characterization of Fe_3O_4 nanoparticles. (a) TEM micrograph, (b) histogram of size distribution. (c) SAED pattern, and (d) behavior of nanoparticles in the presence of a magnetic field.

Figure 2.2d depicts the qualitative magnetic properties of the colloidal nanoparticles, which indicate ferrofluid formation. In the presence of a magnetic field, the spikes observed in the colloidal solution indicate classical ferrofluid behavior, in which superparamagnetic nanoparticles exhibit a preferred magnetic orientation along the magnetic field lines. Small nanoparticles with diameters smaller than the superparamagnetic radius (<70 nm) lack the reminiscence field required for a stable colloidal solution of Fe_3O_4 nanoparticles in toluene.[16] In the presence of an externally

applied magnetic field, these nanoparticles exhibit a rapid magnetic response by aligning themselves with the field and exhibiting their magnetism. This behavior was used to tune the preparation of thin films using the dip-coating method. The viscosity of a ferrofluid solution increases in the presence of a magnetic field. This process occurs as a result of the nanoparticles' partially aligned magnetic moments. In contrast, when there is no magnetic field, the nanoparticles exhibit random Brownian motion.[17–19]

4.2. NANOPARTICLE DEPOSITION

The morphology and thickness of the hematite thin films were analyzed using scanning electron microscopy (SEM) (Figures 2.3 and A2). Using the CND method with varying magnetic fields and nanoparticle concentrations, the thickness of thin films could be modified. The cross-sectional and top-view images depict elongated hematite grains with open porosity, also known as mesoporous films, and a range of thicknesses between 60 and 370 nm. By adjusting the magnetic field and concentration of the colloidal solution, the typical appearance of columnar grains was achieved.

Figure 2.3 demonstrate that, according to SEM images, increasing the nanoparticle concentration led to an increase in thickness, while increasing the magnetic field led to a decrease in thickness. The thickness of the thin films is directly proportional to the particle concentration and inversely proportional to the magnetic field strength applied during deposition. During the deposition processes, the thickness and mesoporous formation varied due to the presence of different magnetic fields. At lower concentrations and higher magnetic fields, pores of 10–30 nm were observed, whereas, at higher concentrations and lower magnetic fields, these pores grew to 30–50 nm.

The magnetic field and concentration affect grain growth and thickness. With an increase in the magnetic field, samples synthesized with 500 mg mL^{-1} exhibited thinner thicknesses and smaller pore sizes. This behavior can be rationally explained by the viscosity of the solution, which decreases in the presence of a weaker magnetic field. However, an excessive increase in viscosity caused by a strong magnetic field tends to keep nanoparticles in the area where the field acts, resulting in a decrease in thickness for stronger magnetic fields. For photoelectrochemical applications, the thickness of the film can be viewed as a crucial factor. Freitas *et al.*[20] correlated the different thicknesses of hematite obtained by the hydrothermal method, demonstrating that the influence of

surface modification promotes polarized states, improves surface trapping, and consequently decreases the lifetime of photogenerated charge.

The APCVD method described by Gratzel *et al.*[21] demonstrates the formation of films with varying thicknesses based on deposition time, as well as the effect of thickness on the low hematite diffusion length (5 nm). The use of a dopant to enhance the film's electronic transport is a possible solution to this issue.

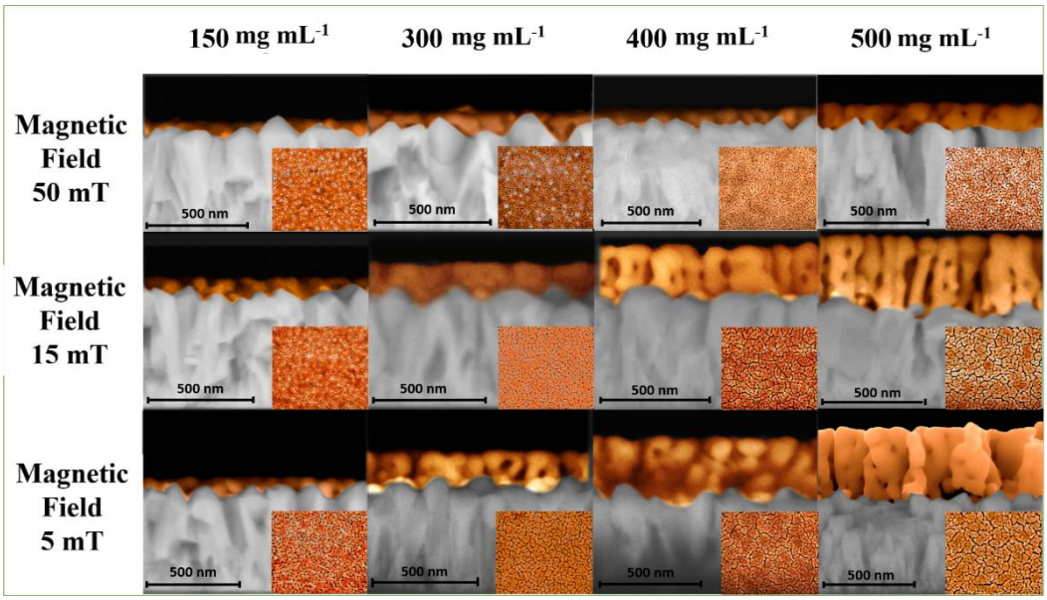

Figure 2.3. Cross-sectional SEM images and top-view (inset figures) of hematite nanostructures obtained for different magnetic fields and nanoparticle concentrations.

Due to the significance of film thickness for PEC performance, the correlation between the magnetic field and the growth of thin films was analyzed. The relationship between concentration, magnetic field, and film thickness is depicted in Figure 2.4. The relationship between film thickness and applied magnetic field (B) for a fixed solution concentration is linear: $thickness = a - b\,B$. Additionally, fixing the magnetic field at different concentrations results in a nonlinear behavior, wherein the $thickness = a + b[C]^d$, where a, b, and d are fitted constants. The linear regression with the negative angular coefficient demonstrated in Figure 2.4a can be readily observed by the inversely proportional behavior of the thickness with applied B. The nonlinear regression presented in Figure 2.4b indicates that the thickness is proportional to the concentration multiplied by a constant d. Several factors, such as solution viscosity, concentration, superficial tension, film take-off speed, and meniscus curvature, govern the thickness of films produced by dip-coating. [22–25]

The scientific literature contains mathematical equations describing the formation of films and their thicknesses based on these variables.[22,26–28] However, these dip-coating equations cannot be used because they do not account for the magnetic field's influence. Due to the influence of the field on film formation parameters such as viscosity, density, and surface tension of the solution, it was not possible to discover a simple equation that describes the results presented here. As shown in Equation (2.2), a relationship expression can be specified.

$$Thickness \propto \frac{[\mathrm{Fe_3O_4}\ NCs]^{\gamma}}{B} \tag{2.2}$$

where $[\mathrm{Fe_3O_4}\ NCs]$ is the concentration of the nanoparticle solution, B is the applied magnetic field, and γ is a coefficient related to the influence of the field on the proportion of nanoparticles present in the solution.

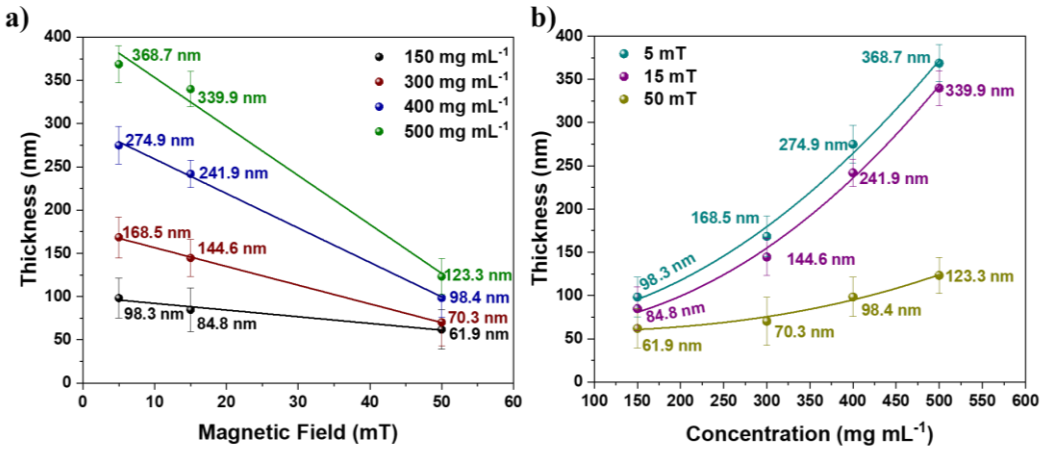

Figure 2.4. Relationship of film thickness with (a) magnetic field and (b) nanoparticle concentration.

4.3. THIN-FILM CHARACTERIZATION

For structural analysis of the hematite films, XRD analysis of the thin films was performed; see Figures A2a–c. All samples were confirmed to be indexable for the rhombohedral hematite phase with space group $R\bar{3}c$. On the FTO substrate, characteristic peaks of the cassiterite phase were also observed, with no evidence of other iron oxide phases. In general, the (104) peak is the most intense diffraction peak for hematite

particles with random crystallographic facet orientations. However, the scientific literature indicates that hematite nanostructures with preferred orientation in the [110] direction have superior photoelectrochemical properties (higher photocurrent densities).[29–31] Thus, the XRD results are essential for analyzing and establishing the connection between the hematite photoanode response and the observed PEC results.

The crystallite size was estimated using the Scherrer equation based on the full width at half maximum (FWHM) of the (110) peak; see Table A2. All samples had a crystallite size of approximately 37–43 nm. The insignificant differences between the samples indicate that the magnetic field has little effect on the crystallite size. As previously mentioned, a decrease in the magnetic field favored the coalescence of the grains, as evidenced by the SEM and TEM images.[10,32,33]

Figure 2.5 is a cross-sectional TEM image of the hematite film synthesized at 5 and 50 mT using 500 mg mL^{-1} at 5 and 50 mT. Observable is the active layer formed by the mesoporous hematite and the FTO substrate layer. The HRTEM analysis revealed a preferential growth of hematite in the [110] direction, corroborating the XRD analysis' findings. The HRTEM images were acquired at the FTO/α-Fe_2O_3 interface (areas A and B in Figure 2.5a and areas C and D in Figure 2.5b at magnetic fields of 5 mT and 50 mT, respectively). To index the hematite crystallographic orientation, a fast Fourier transform (FFT) was applied to the HRTEM images of areas A, B, C, and D (see insets for each area in Figure 2.5a, b).

The sample obtained under a stronger magnetic field displayed a growth orientation in the direction of [110], whereas region D displayed a growth orientation in the direction of [104] for a weaker magnetic field. Although statistical analyses of the HRTEM images are impractical for some FTO/α-Fe_2O_3 interfaces, these results indicate that an increase in the magnetic field aids in the orientation of the hematite crystals, which is consistent with Figure A2d. The HRTEM images in Figure 2.6 depict the atomic lattice fringes of hematite, which coincide precisely with the 3D lattice model along the [104] and [110] directions of the rhombohedral hematite, further demonstrating that the hematite thin films consist of (110) and (104) planes.

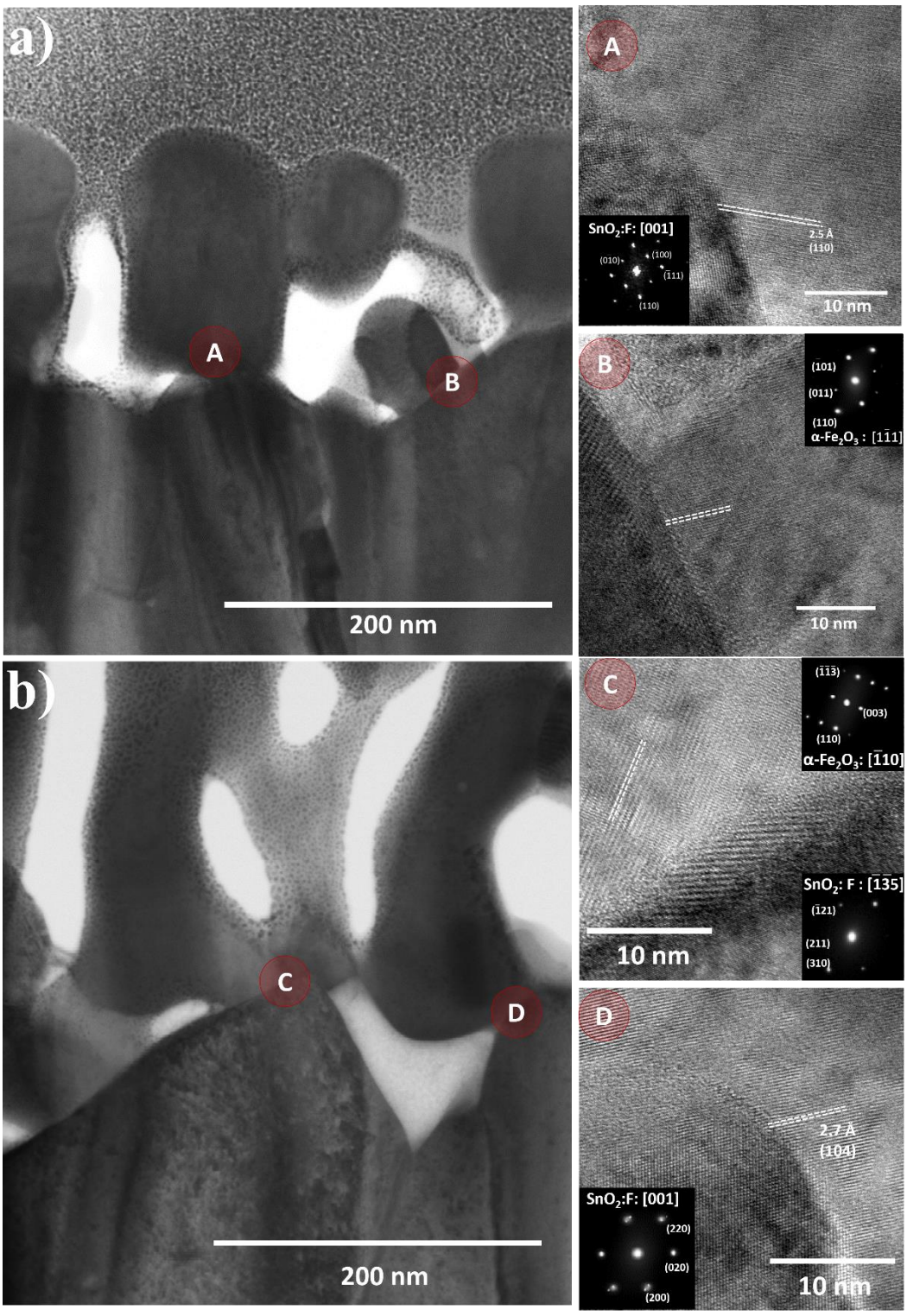

Figure 2.5. TEM images of the hematite/FTO interface obtained with 500 mg·mL^{-1} at (**a**) 5 mT magnetic field and inset show HRTEM images and Fast Fourier Transform images of hematite and FTO (SnO_2) indexed with the crystallographic planes along the zone axis of points A and B. (**b**) 50 mT magnetic field, and inset show HRTEM images and Fast Fourier Transform images of hematite and FTO (SnO_2) indexed with the crystallographic planes along the zone axis of points C and D.

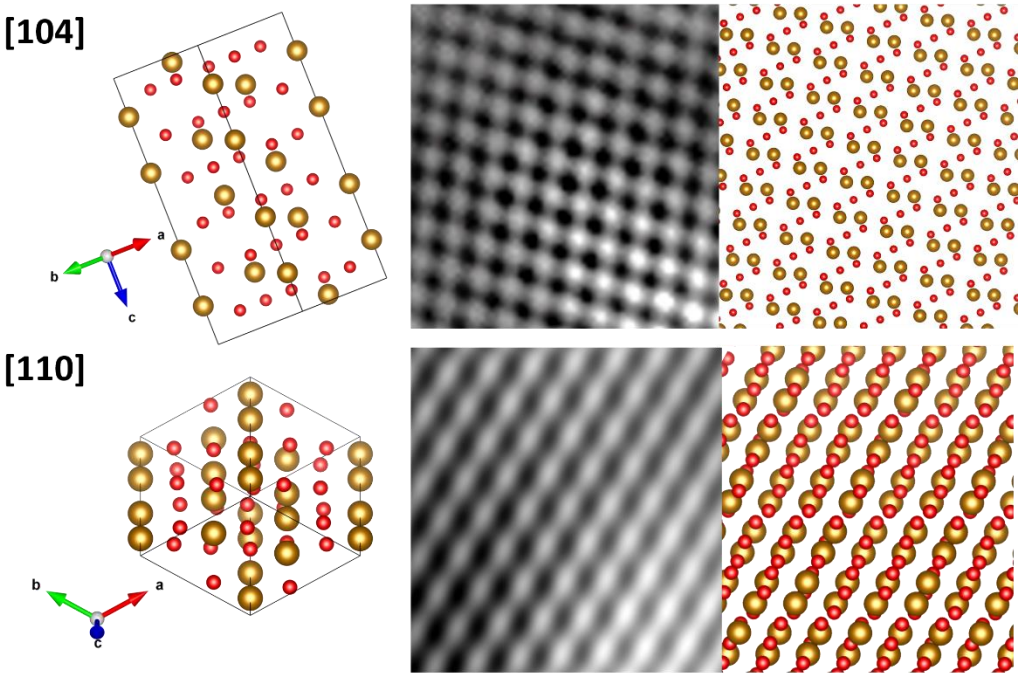

Figure 2.6. HRTEM images showing the atomic lattice fringes of hematite, which precisely coincide with the 3D lattice model along the [104] and [110] directions of rhombohedral hematite.

The optical properties of the hematite thin films were characterized by UV-vis spectroscopy. Figure A4a–c depicts the absorbance spectra of the films obtained at various magnetic fields and concentrations. All samples exhibited absorption up to 600 nm, corroborating the literature-reported bandgap of 2.1–2.2 eV.[34] Using the UV-vis spectra and the irradiance spectrum under a light source with 1.5 AM–100 mW cm^{-2}, it is possible to calculate the absorbed photocurrent density J_{abs} under the condition of a 100% quantum yield (each photon generates one electron-hole pair, *i.e.*, one charge carrier), according to the equation:

$$J_{abs} = q \int_{350}^{600} f(\lambda) A(\lambda) d\lambda \tag{2.3}$$

where q is the electron charge, $f(\lambda)$ is the irradiance spectrum of the light source used for the photoelectrochemical measurements, and $A(\lambda)$ is the absorbance spectrum obtained from UV-vis spectroscopy.

The J_{abs} values of hematite thin films are illustrated by comparing the effects of the magnetic field (Figure 2.7a), the concentration of the colloidal solution (Figure 2.7b),

and the maximum theoretical J_{abs} (Figure 2.7c).[4] According to the SEM and TEM analyses, an increase in magnetic field causes a decrease in hematite thickness, and it is anticipated that J_{abs} will decrease as the magnetic field increases. Due to the quantity of material deposited on the FTO substrate, this behavior occurred. Figure 2.7d depicts the correlation between thickness, J_{abs} and magnetic field, demonstrating that there is an inversely proportional relationship between them, *i.e.*, an increase in the magnetic field causes a decrease in the thickness of the hematite films and their J_{abs} values. This correlation is significant because greater thicknesses and J_{abs} necessitate greater amounts of photoactive material deposition.

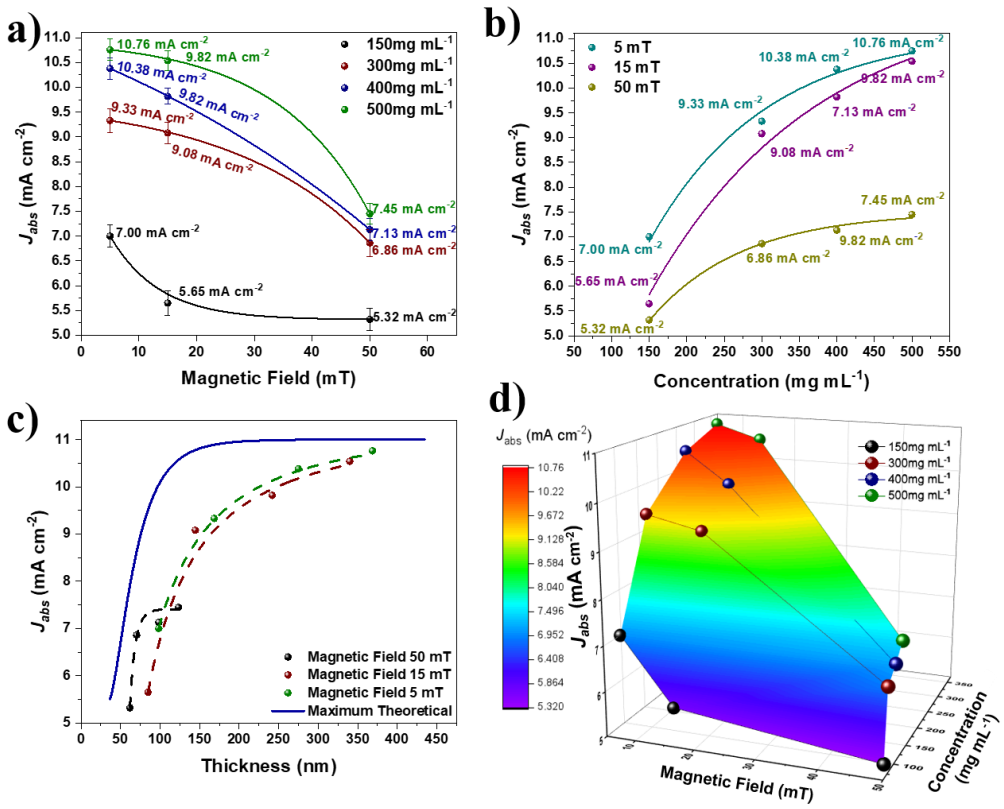

Figure 2.7. Relationship of film J_{abs} with (**a**) magnetic field; (**b**) nanoparticle concentration; (**c**) thickness of hematite films; and (**d**) graph of response surface showing the relationship of the magnetic field, thickness, and J_{abs}.

The process of forming thin films in the presence of higher magnetic fields promotes a higher-density nanoparticle film (compacted), and the process of sintering and removing the organic ligand can increase the porosity of the film, a factor associated with a decrease in J_{abs}.

Figure A5 depicts the photocurrent densities (V curves) obtained under the front and rear illumination. The relationship between the linear sweep measurement of the thin film at 1.23 V RHE (Reference Hydrogen Electrode) and the magnetic field and concentration under front illumination is depicted in Figure 8a. In comparison, the performance under back illumination was marginally higher than under front illumination, which may be attributable to bulk recombination and electron transport issues.[33]

The magnetic field and nanoparticle concentration have a clear effect on the photoelectrochemical outcomes. The use of stronger magnetic fields increases the J_{PH} values, as depicted in Figure 2.8a, which reveals that higher concentrations can be observed when using stronger magnetic fields. This result can be attributed to the proportion of the deposited material that is affected by the presence of a magnetic field, which affects both the absorption values and photoelectrochemical results of the film. For pure hematite, a stronger magnetic field promotes the formation of thinner films, resulting in greater photocurrent density values. When the films begin to thicken, photocurrent is diminished. This could be explained by the higher rate of charge recombination and low electron mobility[34–37].

In contrast, different nanoparticle concentrations also affect the photocurrent density, with J_{PH} decreasing in the case of higher nanoparticle concentrations in lower magnetic fields. We observed that optimal performance was achieved with a lower concentration deposition or greater magnetic fields. To obtain thicker films with higher nanoparticle concentrations, a stronger magnetic field must be applied. Conversely, at lower concentrations, weaker magnetic fields can be used.

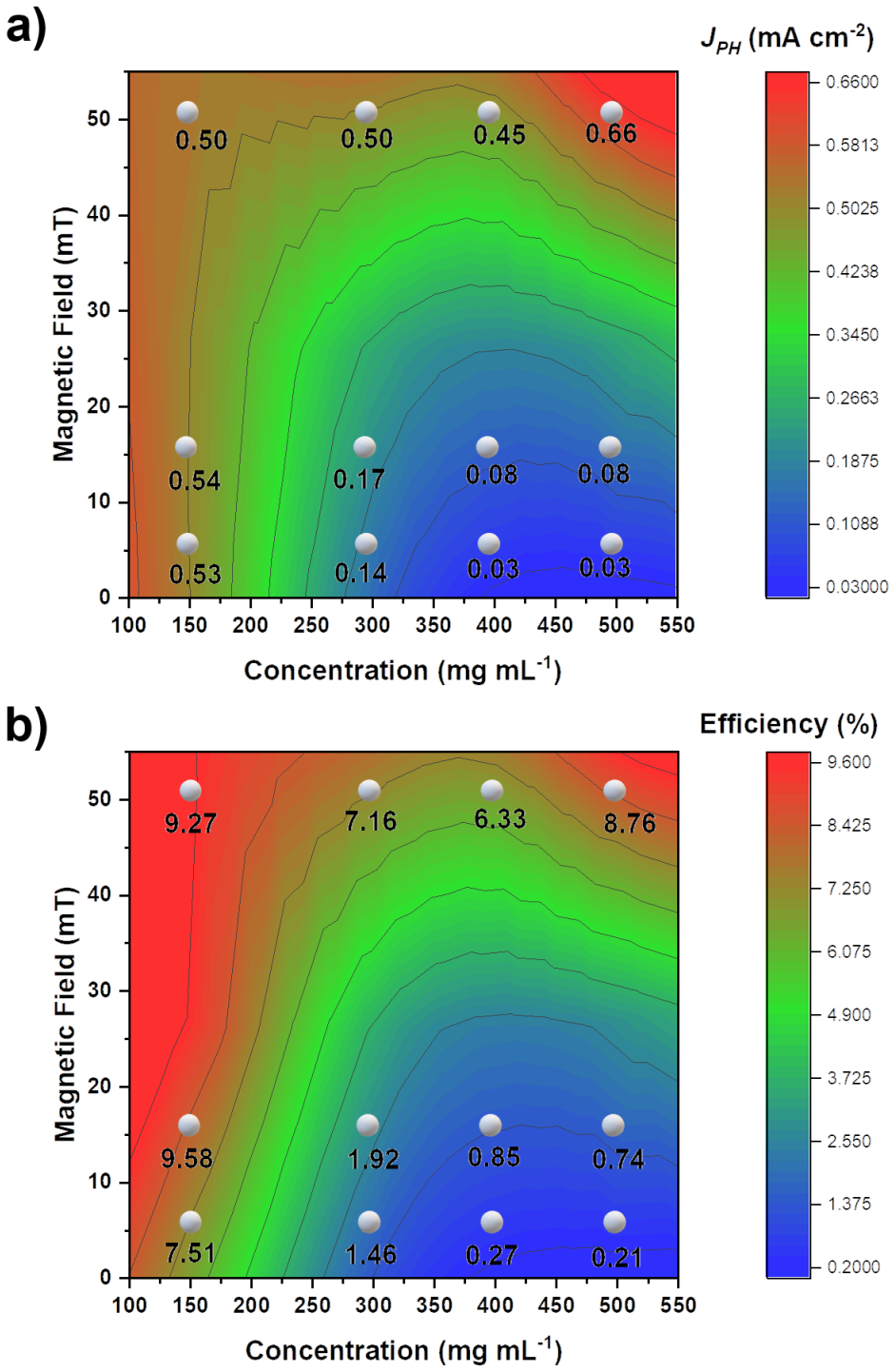

Figure 2.8. Response of photoelectrochemical measurements for (**a**) front illumination and (**b**) efficiency for different magnetic fields and nanoparticle concentrations.

Figure 2.8b illustrates the correlation between the efficiency of thin films and the magnetic field and concentration under front illumination. Using Equation (2.4), the global efficiency of the thin-films $\eta_{overall}$ was calculated.

$$J_{PH} = J_{abs} * \eta_{overall} \quad ; \quad \eta_{overall(\%)} = \frac{J_{PH}}{J_{abs}} * 100 \tag{2.4}$$

The relationship between the efficiency's dependence on the magnetic field and concentration and the photocurrent density is essentially identical. The magnetic field had a two-step effect on the performance of hematite thin films. At higher magnetic fields, all thin films exhibited a similar efficiency of approximately 7.9%, whereas the film with the lowest concentration achieved an efficiency of 9.3%. In contrast, for lower magnetic fields, the efficiency of these films was highly dependent on their concentration during preparation. The efficiency of the thin films prepared at high concentrations in weaker magnetic fields was poor. To achieve greater efficiency at different nanoparticle concentrations, it is necessary to employ strong magnetic fields; if a weaker magnetic field is employed, lower nanoparticle concentrations are required. Another possible explanation for the effect of magnetism is the presence of a magnetic field that aligns magnetic nanoparticles, which, when the material is converted to hematite, promotes the film's texturing in the <110> directions, resulting in excellent photoelectrochemical properties. Future research will focus on the dip-coating rise and fall velocity, which could affect the formation of thin films, as well as how the presence of a magnetic field influences this process.

5. CONCLUSIONS

Our findings indicate that the magnetic-field-assisted CND method produces superior hematite thin-film control and high-performance PEC devices. Moreover, we believe that the magnetic field deposition process is a viable alternative to the active hematite benchmark efficiency. The magnetite nanoparticles that were synthesized were monodispersed with a narrow size distribution, presenting a stable colloidal solution and forming a ferrofluid. A comparison of the film thicknesses of the applied magnetic field demonstrated that the magnetic field intensity could be used to regulate the formation and thickness of these films. In the presence of a stronger magnetic field, the SEM analysis revealed a reduction in the size of the pores. Intriguingly, the PEC results revealed that a

stronger magnetic field is required to achieve a higher J_{PH} and efficiency performance, regardless of the nanoparticle concentration. Applying a weaker magnetic field requires a lower nanoparticle concentration to activate a greater J_{PH} and efficiency.

6. ACKNOWLEDGMENTS

All Brazilian agencies gratefully acknowledged, the project by FAPESP (projects CEPID—2013/07296-2, 2017/02317-2, 2017/03135, and 2018/05159-1) and CAPES—Finance Code 001.

7. REFERENCES

1. Sivula, K.; Le Formal, F.; Gratzel, M. Solar water splitting: Progress using hematite (α-Fe_2O_3) photoelectrodes. *ChemSusChem* **2011**, *4*, 432–449.
2. Bora, D.K.; Braun, A.; Constable, E.C. "In rust we trust". Hematite—the prospective inorganic backbone for artificial photosynthesis. *Energy Environ. Sci.* **2013**, *6*, 407–425.
3. He, Y.; Hamann, T.; Wang, D. Thin film photoelectrodes for solar water splitting. *Chem. Soc. Rev.* **2019**, *48*, 2182–2215.
4. Warren, S.C.; Voïtchovsky, K.; Dotan, H.; Leroy, C.M.; Cornuz, M.; Stellacci, F.; Hébert, C.; Rothschild, A.; Grätzel, M. Identifying champion nanostructures for solar water-splitting. *Nat. Mater.* **2013**, *12*, 842–849.
5. I. S. Cho, H. S. Han, M. Logar, J. Park and X. Zheng, Advanced Energy Materials, 2016, 6, 1501840.
6. Gonçalves, R.H.; Lima, B.H.R.; Leite, E.R. Magnetite Colloidal Nanocrystals: A Facile Pathway To Prepare Mesoporous Hematite Thin Films for Photoelectrochemical Water Splitting. *J. Am. Chem. Soc.* **2011**, *133*, 6012–6019.
7. S. D. Tilley, M. Cornuz, K. Sivula and M. Grätzel, *Angewandte Chemie International Edition*, 2010, **49**, 6405-6408.
8. Sivula, K.; Zboril, R.; Le Formal, F.; Robert, R.; Weidenkaff, A.; Tucek, J.; Frydrych, J.; Grätzel, M. Photoelectrochemical Water Splitting with Mesoporous Hematite Prepared by a Solution-Based Colloidal Approach. *J. Am. Chem. Soc.* **2010**, *132*, 7436–7444.
9. de Lima, F.C.; Schleder, G.R.; Souza Junior, J.B.; Souza, F.L.; Destro, F.B.; Miwa, R.H.; Leite, E.R.; Fazzio, A. Unveiling the dopant segregation effect at hematite interfaces. *Appl. Phys. Lett.* **2021**, *118*, 201602.

10. Matsuhisa, M.; Tsubaki, S.; Kishimoto, F.; Fujii, S.; Hirano, I.; Horibe, M.; Suzuki, E.; Shimizu, R.; Hitosugi, T.; Wada, Y. Hole Accumulation at the Grain Boundary Enhances Water Oxidation at α-Fe_2O_3 Electrodes under a Microwave Electric Field. *J. Phys. Chem. C* **2020**, *124*, 7749–7759.
11. Gonçalves, R.H.; Leite, E.R. The colloidal nanocrystal deposition process: An advanced method to prepare high performance hematite photoanodes for water splitting. *Energy Environ. Sci.* **2014**, *7*, 2250–2254.
12. Comsol, A.B. COMSOL Multiphysics® v. 5.6. Stockholm, Sweden. Available online: http://www.comsol.com (accessed on 28 March 2022).
13. Xu, Z.; Shen, C.; Hou, Y.; Gao, H.; Sun, S. Oleylamine as Both Reducing Agent and Stabilizer in a Facile Synthesis of Magnetite Nanoparticles. *Chem. Mater.* **2009**, *21*, 1778–1780.
14. Sun, S.; Zeng, H. Size-Controlled Synthesis of Magnetite Nanoparticles. *J. Am. Chem. Soc.* **2002**, *124*, 8204–8205.
15. Pacakova, B.; Kubickova, S.; Salas, G.; Mantlikova, A.R.; Marciello, M.; Morales, M.P.; Niznansky, D.; Vejpravova, J. The internal structure of magnetic nanoparticles determines the magnetic response. *Nanoscale* **2017**, *9*, 5129–5140.
16. Al Harraq, A.; Lee, J.G.; Bharti, B. Magnetic field–driven assembly and reconfiguration of multicomponent supraparticles. *Sci. Adv.* **2020**, *6*, eaba5337.
17. Rosensweig, R.E.; Kaiser, R.; Miskolczy, G. Viscosity of magnetic fluid in a magnetic field. *J. Colloid Interface Sci.* **1969**, *29*, 680–686.
18. Shen, J.P.; Doi, M. Effective Viscosity of Magnetic Fluids. *J. Phys. Soc. Jpn.* **1990**, *59*, 111–117.
19. Shliomis, M.I.; Morozov, K.I. Negative viscosity of ferrofluid under alternating magnetic field. *Phys. Fluids* **1994**, *6*, 2855–2861.
20. Freitas, A.L.M.; Tofanello, A.; Souza, F.L.; Li, Y. Insights on Thickness-Dependent Charge Transfer Efficiency Modulated by Ultrasonic Treatment in Hematite Photoanodes. *J. Phys. Chem. C* **2021**, *125*, 9981–9989.
21. Cesar, I.; Sivula, K.; Kay, A.; Zboril, R.; Grätzel, M. Influence of Feature Size, Film Thickness, and Silicon Doping on the Performance of Nanostructured Hematite Photoanodes for Solar Water Splitting. *J. Phys. Chem. C* **2009**, *113*, 772–782.
22. Brinker, C.J. Dip Coating. In *Chemical Solution Deposition of Functional Oxide Thin Films*, Schneller, T., Waser, R., Kosec, M., David Payne, D., Eds.; Springer-Verlag: Wien, Austria, 2013; pp. 233–261.

23. Jilani, A.; Abdel-wahab, M.S.; Hammad, A.H. Advance Deposition Techniques for Thin Film and Coating. In *Modern Technologies for Creating the Thin-film Systems and Coatings*, Nikitenkov, N.N., Ed.; IntechOpen: London, UK, 2017.
24. Maillard, M.; Bleyer, J.; Andrieux, A.L.; Boujlel, J.; Coussot, P. Dip-coating of yield stress fluids. *Phys. Fluids* **2016**, *28*, 053102.
25. Tang, X.; Yan, X. Dip-coating for fibrous materials: Mechanism, methods and applications. *J. Sol-Gel Sci. Technol.* **2016**, *81*, 378–404.
26. Wu, L.; Yang, D.; Fei, L.; Huang, Y.; Wu, F.; Sun, Y.; Shi, J.; Xiang, Y. Dip-Coating Process Engineering and Performance Optimization for Three-State Electrochromic Devices. *Nanoscale Res. Lett.* **2017**, *12*, 390.
27. Mbam, S.O.; Nwonu, S.E.; Orelaja, O.A.; Nwigwe, U.S.; Gou, X.-F. Thin-film coating; historical evolution, conventional deposition technologies, stress-state micro/nano-level measurement/models and prospects projection: A critical review. *Mater. Res. Express* **2019**, *6*, 122001.
28. Figueira, R.; Silva, C.; Pereira, E. Influence of Experimental Parameters Using the Dip-Coating Method on the Barrier Performance of Hybrid Sol-Gel Coatings in Strong Alkaline Environments. *Coatings* **2015**, *5*, 124–141.
29. Dias, P.; Vilanova, A.; Lopes, T.; Andrade, L.; Mendes, A. Extremely stable bare hematite photoanode for solar water splitting. *Nano Energy* **2016**, *23*, 70–79.
30. Kment, S.; Schmuki, P.; Hubicka, Z.; Machala, L.; Kirchgeorg, R.; Liu, N.; Wang, L.; Lee, K.; Olejnicek, J.; Cada, M.; et al. Photoanodes with Fully Controllable Texture: The Enhanced Water Splitting Efficiency of Thin Hematite Films Exhibiting Solely (110) Crystal Orientation. *ACS Nano* **2015**, *9*, 7113–7123.
31. Cornuz, M.; Grätzel, M.; Sivula, K. Preferential Orientation in Hematite Films for Solar Hydrogen Production via Water Splitting. *Chem. Vap. Depos.* **2010**, *16*, 291–295.
32. Xu, Y.; Jian, J.; Li, F.; Liu, W.; Jia, L.; Wang, H. Porous $CuBi_2O_4$ photocathodes with rationally engineered morphology and composition towards high-efficiency photoelectrochemical performance. *J. Mater. Chem. A* **2019**, *7*, 21997–22004.
33. Liao, P.; Toroker, M.C.; Carter, E.A. Electron Transport in Pure and Doped Hematite. *Nano Lett.* **2011**, *11*, 1775–1781.
34. Soares, M.R.S.; Costa, C.A.R.; Lanzoni, E.M.; Bettini, J.; Ramirez, C.A.O.; Souza, F.L.; Longo, E.; Leite, E.R. Unraveling the Role of Sn Segregation in the Electronic Transport of Polycrystalline Hematite: Raising the Electronic Conductivity by

Lowering the Grain-Boundary Blocking Effect. *Adv. Electron. Mater.* **2019**, *5*, 1900065.

35. Souza, F.L.; Lopes, K.P.; Longo, E.; Leite, E.R. The influence of the film thickness of nanostructured α-Fe_2O_3 on water photooxidation. *Phys. Chem. Chem. Phys.* **2009**, *11*, 1215–1219.
36. Soares, M.R.; Goncalves, R.H.; Nogueira, I.C.; Bettini, J.; Chiquito, A.J.; Leite, E.R. Understanding the fundamental electrical and photoelectrochemical behavior of a hematite photoanode. *Phys. Chem. Chem. Phys. PCCP* **2016**, *18*, 21780–21788.
37. Wang, Y.; Zhang, J.; Balogun, M.-S.; Tong, Y.; Huang, Y. Oxygen vacancy–based metal oxides photoanodes in photoelectrochemical water splitting. *Mater. Today Sustain.* **2022**, *18*, 100118.

Chapter 3

Ideal dopant to increase charge separation efficiency in Hematite photoanodes: Germanium

Murillo Henrique de Matos Rodrigues,[ab] Ingrid Rodriguez-Gutierréz,[bc] Carlos Alberto Ospina Ramirez,[b] Carlos Alberto Rodrigo Costa,[b] Cleyton Alexandre Biffe,[b] João Batista de Souza Junior,[b] Flavio Leandro Souza,[bc] and Edson Roberto Leite[ab]*

[a]Departamento de Química, Universidade Federal de São Carlos 13565-905, Brazil.

[b]Laboratório Nacional de Nanotecnologia (LNNano), CNPEM 13083-100, Brazil

[c]Centro de Ciências Naturais e Humanas, Universidade Federal do ABC 09606-070, Brazil.

This chapter was published in:

*J. Mater. Chem. A, 2022,**10**, 13456-13466*. https://doi.org/10.1039/D2TA03932J

Supplementary Information is attached in Appendix B in Chapter 6.

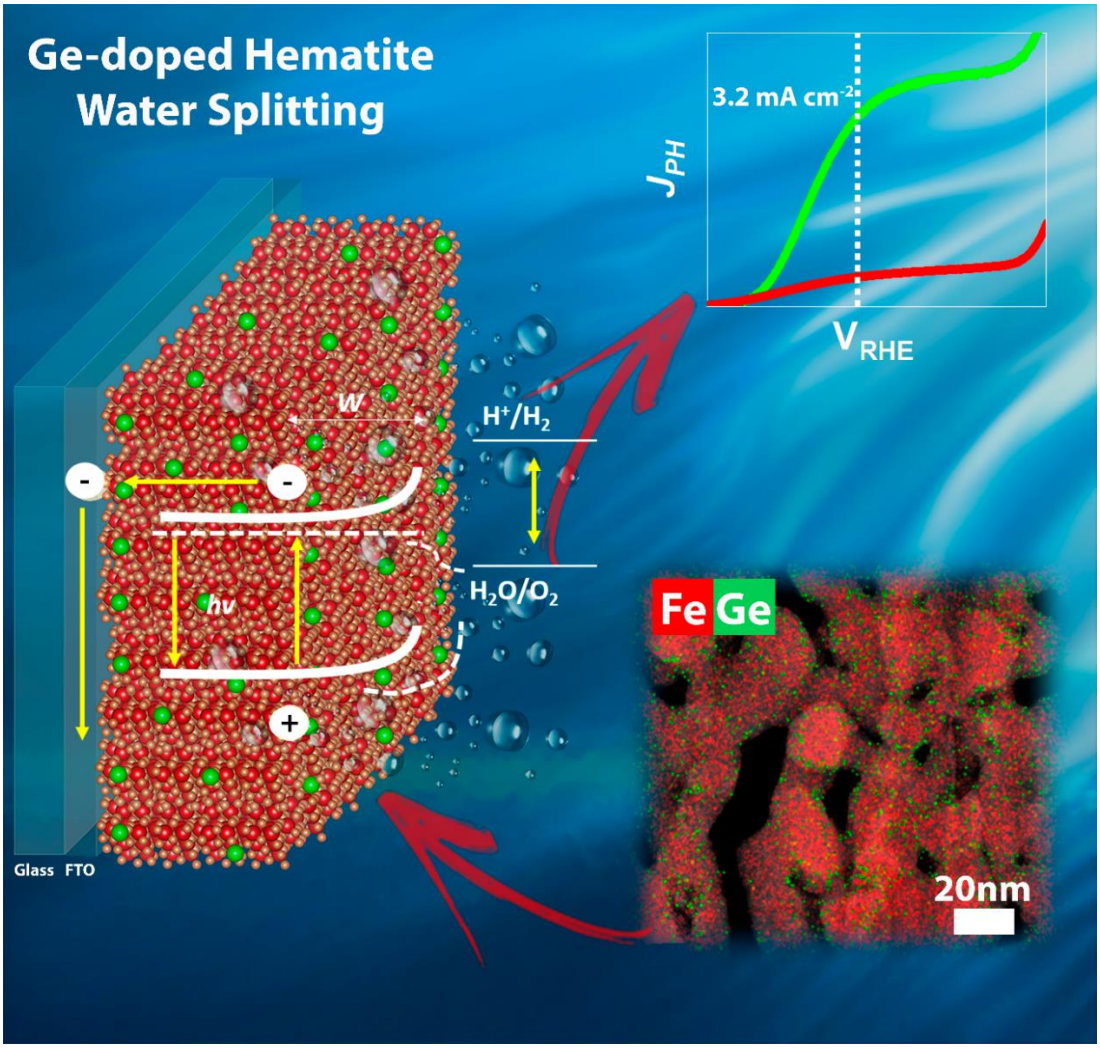

1. ABSTRACT

Hematite, owing to its ideal physical properties, chemical stability, and abundance on Earth, has become a potential candidate as a photoanode in solar water-splitting device applications. However, the high photogenerated charge recombination due to its low efficiency of charge separation as a consequence of poor electronic transport and collection at the back contact has hindered its commercial application. Based on the limitations of hematite, this study describes germanium as a potentially ideal element that combines the beneficial improvement in charge transfer efficiency and morphology control toward high hematite-based photoanode performance. Intensity-modulated photocurrent spectroscopy results demonstrated that the addition of Ge enhanced the charge mobility, leading to a superior charge separation efficiency than the pristine hematite photoanode. C-AFM measurements demonstrate that Ge improves the electronic conductivity and increases the majority carrier mobility. Photoelectrochemical measurements performed at different wavelengths shows the Ge interferes with the formation of small polarons, making the charges more mobile (delocalized), thus favoring the process of photoinduced charge separation. The combined role played by Ge addition resulted in a significant improvement in the photoelectrochemical performance from 0.5 to 3.2 mA cm^{-2} at 1.23 V_{RHE} by comparing the pristine and Ge–hematite-based photoanodes.

2. INTRODUCTION

The storage of solar energy as a hydrogen fuel, obtained from water splitting through a photoelectrochemical cell (PEC), can provide a clean and renewable energy alternative for the increasing demand of the world.[1, 2] However, to reach competitive levels, PEC-based devices depend on robust and efficient semiconductors (n-type semiconductors, for instance) formed by abundant elements on our planet and with adequate bandgap positions to absorb solar radiation. Hematite (α-Fe_2O_3) satisfies most of these requirements for use as a photoanode in PEC device applications. However, owing to recombination processes between photogenerated pairs of electrons (e^-) and holes (h^+) that occur at the surface, bulk, and semiconductor-electrolyte interface, the efficiency of the hematite photoanode is still far less than the theoretically predicted value.[3]

In the last decades, intense studies have been devoted to surpassing the aforementioned limitations by employing a complex rational design mainly involving multiple modifications[4, 5] that caused the photocurrent response to exceeding values of 3.0 mA/cm^2 at 1.23 V_{RHE}[6-11]. These modifications include doping, deposition of an overlayer to act as a passivating or co-catalyst layer, formation of heterojunctions on the electrode surface, morphology control, and optimization of the hematite/substrate interface (transparent conductive oxide).[4, 5, 12]

Several attempts dedicated to improving the performance of hematite photoanodes have focused on charge transfer processes in the liquid-semiconductor interface of PEC devices, that is, they have been concerned with minority charge carriers (h^+).[5, 12, 13] Doping is a mechanism that aims to improve electronic transport and acts on the majority of charge carriers (e^-) in an n-type semiconductor. The increase in electronic conductivity is a rational way to design highly active hematite photoanodes because it increases the extraction of electrons in back-contact electrodes (transparent conductor oxide materials), resulting in an increase in the charge separation efficiency (CSE) between e^- and h^+.

The doping of foreign atoms, such as groups IV and XIV of the periodic table, into the hematite lattice, has been extensively discussed in previous studies.[3-5, 14, 15] However, there is no consensus on how dopants work to improve the performance of photoanodes. It is common to find experimental results demonstrating that hematite doping does not increase the donor density (N_d) in the literature.[3, 16, 17]

Perhaps the origin of the lack of agreement on the action mechanism of dopants lies in the fact that small polaron hopping determines carrier transport and limits electron

transport in α-Fe_2O_3.[18] Furthermore, as discovered by Leone et al.[19], the small-polaron localization of photoexcited carriers is wavelength-dependent. Small polarons can be efficiently formed near the band-edge excitation, resulting in fewer mobile carriers. However, fewer polarons are generated through higher-energy excitation, resulting in more mobile carriers and a longer lifetime.[19] A clear relationship is observed between the charge carrier mobility and optical properties, which leads us to believe that the function of some dopants is to increase the mobility of charge carriers and not their concentration. Another reason for the lack of agreement on the action of dopants is the strong dependence of foreign atom incorporation in the hematite lattice on the photoanode synthesis method.

As discussed recently by Souza Junior *et al.*, the protocol used to incorporate dopants has a strong impact on the performance of PEC devices[20]. In addition to its beneficial effects, the doping of hematite also has side effects, such as surface states, which modify the electrochemical properties of the pristine hematite (mainly the flat band potential (V_{fb}) and charge transfer resistance). The formation of surface states occurs because of the segregation of dopants on the hematite surface.[21, 22]

Several prior publications have reported the incorporation of additives in hematite films and demonstrated that the segregation of these elements is a critical factor in improving photoelectrochemical properties.[21-24] For instance, the segregation of Sb and Sn at solid–solid interfaces (grain boundaries) decreases the grain boundary resistance, facilitating electronic transport and consequently increasing the conductivity of hematite.[23, 24] Recently, several theoretical and experimental studies have highlighted the beneficial effect of germanium (Ge) as an additive to improve the photocurrent of hematite photoanodes.[25-31] After analyzing the experimental studies, we observed a clear dependence of the photoelectrochemical performance of the hematite photoanodes on the synthesis route used to introduce Ge.[31] This dependence is associated with the low chemical compatibility between α-Fe_2O_3 and GeO_2.[32]

As shown in the phase diagram of this binary system (Figure 6.1 in the Appendix B), at equilibrium, Ge is not soluble in the hematite lattice and vice versa. Thus, from thermodynamic arguments, we expect the segregation and formation of Ge clusters.[30-32] The low reactivity between α-Fe_2O_3 and GeO_2 made us believe that to maximize the benefits of Ge, it is necessary to use synthetic routes that enable the control of Ge incorporation, generating a metastable solid solution.

In this study, we explore two different approaches that lead to greater control of Ge incorporation in the hematite photoanode. These approaches are combined with a colloidal nanocrystal deposition (CND) process using magnetite nanocrystals (Fe_3O_4) as the α-Fe_2O_3 precursor.[21, 22, 33] Photoanodes prepared through this novel strategy were systematically characterized to evaluate the role of the additive and its impact on sunlight-driven water oxidation. We will demonstrate that Ge, owing to its chemical characteristics, will act as an "ideal dopant" to increase the CSE of hematite photoanodes. We coined the term "ideal dopant" to describe a dopant that increases the efficiency of the charge separation process by acting on the majority of the charge carriers with minimum interference in the charge transfer process at the semiconductor–electrolyte interface.

In previous works, we described that dopants such as Sn and Sb also promote a better charge separation process, improving the hematite photoanode performance.[21-22] However, these dopants promote the formation of surface states, increasing the on-set and the flat band potential, thus hindering the charge transfer process. In addition, an ideal dopant can also control the morphology of the hematite photoanode (as a beneficial side effect).

3. EXPERIMENTAL METHODS

3.1. CHEMICALS AND MATERIALS

Iron (III) acetylacetonate (99%), oleyl alcohol (85%), oleic acid (90%), germanium (IV) ethoxide (99%), and sodium hydroxide (99%) were purchased from Sigma-Aldrich. The chemicals and reagents were used as received without further purification.

3.2. SYNTHESIS OF MAGNETITE NANOPARTICLES (USED IN SAMPLES FEGE2 AND PRISTINE FE)

We synthesized magnetite (Fe_3O_4) NCs following the protocol developed by Gonçalves et al.[33] We added 35 mL of oleyl alcohol and 8.0 mmol of iron (III) acetylacetonate into a reaction vessel (a 100 mL three-necked round-bottomed flask). The flask was thereafter heated at 100 °C under vacuum for 15 min for complete solubilization of iron (III) acetylacetonate. Subsequently, the vessel was heated at 320 °C under an N_2 atmosphere for 60 min. Thereafter, the colloidal solution formed was allowed to cool to

room temperature. The NCs formed were washed three times with acetone and re-dispersed in toluene, yielding a colloidal dispersion with a concentration of 400 mg ml^{-1}.

3.3. SYNTHESIS OF GE-DOPED MAGNETITE NANOPARTICLES (USED IN THE SAMPLE FEGE1)

The Ge-doped magnetite (Fe_3O_4) NC was prepared as follows: 35 mL of oleyl alcohol and 8 mmol of iron (III) acetylacetonate were put in a three-necked round-bottomed flask (100 mL). The flask was heated at 100 °C under a vacuum for 15 min to completely solubilize iron (III) acetylacetonate. At this stage, we added 2 mL of an oleic acid solution containing 0.135 mmol of Germanium (IV) ethoxide ([Ge]/([Ge]+[Fe]=0.017), and the reaction vessel was heated at 320 °C under N_2 atmosphere for 60 min. Thereafter, the colloidal solution formed was allowed to cool to room temperature. The NC formed was precipitated three times with acetone and re-dispersed in toluene, yielding a colloidal dispersion with a concentration of 400 mg ml^{-1}.

3.4. MAGNETITE NANOPARTICLES CONTAIN GE PRECURSOR PREPARATION (USED FOR FEGE2 SAMPLE)

To prepare the FeGe2 sample, we added 0.0902 mmol of Germanium ethoxide ([Ge]/([Ge]+[Fe]=0.017) to the colloidal solution of undoped magnetite NC (400 mg of magnetite - 1.73 mmol) under N_2 atmosphere. The colloidal dispersion was homogenized in an ultrasonic bath for 30 min.

3.5. THIN FILMS PREPARATION

The thin films were prepared through the CND process using a spin-coating deposition procedure as follows: A commercial FTO substrate was used for the film deposition. Initially, the substrates were washed with soap, isopropyl alcohol, acetone, and toluene. Pure magnetite, Ge-doped magnetite, and colloidal solutions of magnetite and Ge precursors were deposited through spin-coating at a fixed rotation speed of 10 s (5000 rpm). After deposition, the films were sintered in a tubular furnace at 850 °C for 4 min for materials containing Ge and 20 min for undoped hematite.

3.6. PHOTOELECTROCHEMICAL CHARACTERIZATION

Photoelectrochemical measurements were performed in a standard three-electrode cell with the hematite film as the working electrode (0.28 cm^2 area), Ag/AgCl in a KCl-saturated solution as the reference electrode, and a platinum plate as the counter electrode.

1.0 M NaOH solution (NaOH ACS Aldrich, 99.99%) in highly pure water (pH = 13.6, at 25 °C) was used as the electrolyte. A scanning potentiostat (potentiostat/galvanostat μAutolab III) was used to measure the dark and illuminated currents, at a scan rate of 20 mV s^{-1}. Sunlight (100 mW cm^{-2}) was simulated using a 250 W ozone-free xenon lamp (Osram) and an AM 1.5 filter (Newport Corp). Several electrochemical experiments assisted by a sunlight simulator were conducted using electrolytes with the addition of H_2O_2 as a hole scavenger (using an aqueous electrolyte solution prepared with 1 M NaOH + 0.5 M H_2O_2). IMPS measurements were performed in a three-electrode cell using a Metrohm Autolab PGSTAT302 N/FRA2 setup, utilizing a 470 nm high-intensity blue LED for both the bias light intensity and sinusoidally modulated light. The modulation frequency ranged from 10.000 to 0.1 Hz, with a modulation amplitude of approximately 10% of the base light intensity, and the linearity of the response was tested and confirmed using Lissajous plots. The IMPS spectra were normalized by determining the number of modulated photons.

For the Mott–Schottky analysis, a Nyquist plot was constructed from 1.75 V_{RHE} to 0.8 V_{RHE} for both doped and undoped hematite, at a frequency of 1 kHz. Equation 3.1 and Mott–Schottky plots were used to determine the donor density (N_d).

$$\frac{1}{C^2} = \frac{2}{\varepsilon_0 \varepsilon_r e N_d}\left(V - V_{fb} - \frac{k_B T}{e}\right), \tag{3.1}$$

where ε_0 denotes the permittivity under vacuum, ε_r is the relative permittivity (hematite was taken as 80)[34], V is the applied potential, T is the absolute temperature, e is the electronic charge, and k_B is Boltzmann's constant. UV-vis absorption spectra were obtained using a Shimadzu UV-3600 Plus spectrophotometer.

The absorbed photocurrent density Jabs was calculated as expressed in Equation 3.2 as follows:

$$J_{abs} = q \int_{350}^{600} f(\lambda) A(\lambda) d\lambda, \tag{3.2}$$

where q denotes the electron charge, f(λ) is the irradiance spectrum (in units Nº of photons cm^{-2} nm^{-1} s^{-1}) of the light source used for photoelectrochemical measurements (AM 1.5 – 100 mW cm^{-2}), and A(λ) is the absorptance spectrum of the pristine Fe and FeGe1 samples.

The APCE measurements were performed using 470, 532, and 627 nm high-intensity LED irradiation and can be expressed as follows:

$$APCE(\%) = \frac{1240 J_{photo}/E(\lambda)\lambda}{1-10^{A}} x10, \quad (3.3)$$

where J_{photo} denotes the photocurrent density (mA cm^{-2}), E(λ) is the irradiance of the LED (mW cm^{-2}), λ is the LED wavelength, and A is the absorbance of the LED wavelength used.

3.7. CHARACTERIZATION

The thin films were characterized through XRD (Bruker, D8 Advance ECO) using CuKα radiation (λ = 0.15406 nm), linear detector LYNXEYE XE (PSD of 2.948°), primary optics (2.5° axial soller and 0.6 mm slit), and secondary optics (2.5° axial soller and 5.4 mm slit). TEM, HAADF-STEM, and EDS analyses were performed at 300 kV using a Titan Themis instrument with Cs correction. The analyses were performed with a spatial resolution greater than 0.1 nm. The TEM STEM/EDS sample was prepared via in-situ milling using a focused ion beam system. Chemical surface analyses were performed by an XPS (Thermo Fisher Scientific, UK) using Al–Kα X-rays under vacuum (>10-8 mbar) and charge compensation during the measurements. A resolution of 1 eV with five scans was used to gather the survey spectra, where high-resolution spectra were recorded with 0.1 eV resolution and 50 scans. The binding energies were referenced to the C 1s peak at 284.8 eV. Data analysis was performed using the Thermo Scientific™ Avantage™ software. The C-AFM measurements were performed using an AFM microscope (Park Systems NX10) under an N_2 atmosphere with a tip nanosensor PPP-EFM Pt/Ir silicon coating with 75 Khz-2.8 N m and 25 nm of radius. The scan head was mounted within an environmental chamber maintained at constant relative humidity and temperature (<10% RH and 25 °C).

4. RESULTS AND DISCUSSION

As described in Scheme 3.1, two different approaches were employed to incorporate Ge into hematite. In the first route (FeGe1), Ge was introduced during the synthesis of Fe_3O_4 nanocrystals (NCs) (Scheme 3.1a). After the synthesis, the Ge-doped Fe_3O_4 NC was deposited through spin-coating onto fluorine-doped-SnO_2 (FTO) glass substrates,

followed by a sintering process that promotes the formation of a hematite photoanode with a gradient of Ge concentration [Ge]. From this route, it is expected that the surfaces of the hematite grains are rich in Ge, with a gradual reduction in the [Ge] concentration moving away from the surface towards the hematite grain core as shown in Scheme 1a. For more details, refer to the experimental procedure. In the second route (FeGe2), Ge was added as a molecular compound that was soluble in toluene after the synthesis of Fe_3O_4 NCs (Scheme 3.1b). Herein, the sintering process led to the formation of hematite, with Ge preferentially segregating at the hematite grain surface as shown in Scheme 1b. The details of the synthesis protocol can be found in the experimental methods.

As shown in Scheme 3.1, after NC preparation and deposition onto FTO, a sintering process at 850 °C was performed. At this stage, systematic efforts were devoted to optimizing the parameters related to photoanode processing, such as Ge concentration, number of deposited layers, and time sintering treatment. In this process, the photocurrent density (J_{PH}) at 1.23 VRHE was used as a figure of merit, aiming at its maximization. The parameter optimization achieved by studying the photoanodes designed following route FeGe1 was used to fabricate photoanodes via route FeGe2. Details regarding the optimization of the parameters can be found in Appendix B (Tables B1, B2, and B3). As a result of this study, it was established that the optimal nominal Ge concentration is 1.7 at%. Then, the optimized photoanodes were fabricated by two cycles of deposition processing followed by sintering at 850 °C for 4 min. An undoped hematite photoanode (pristine Fe), as a reference for performance, was prepared as reported in previous studies[21, 22], which involved a single deposition step and thermal treatment at 850 °C for 20 min. Thus, all analyses presented in this study are related to the samples prepared under these conditions.

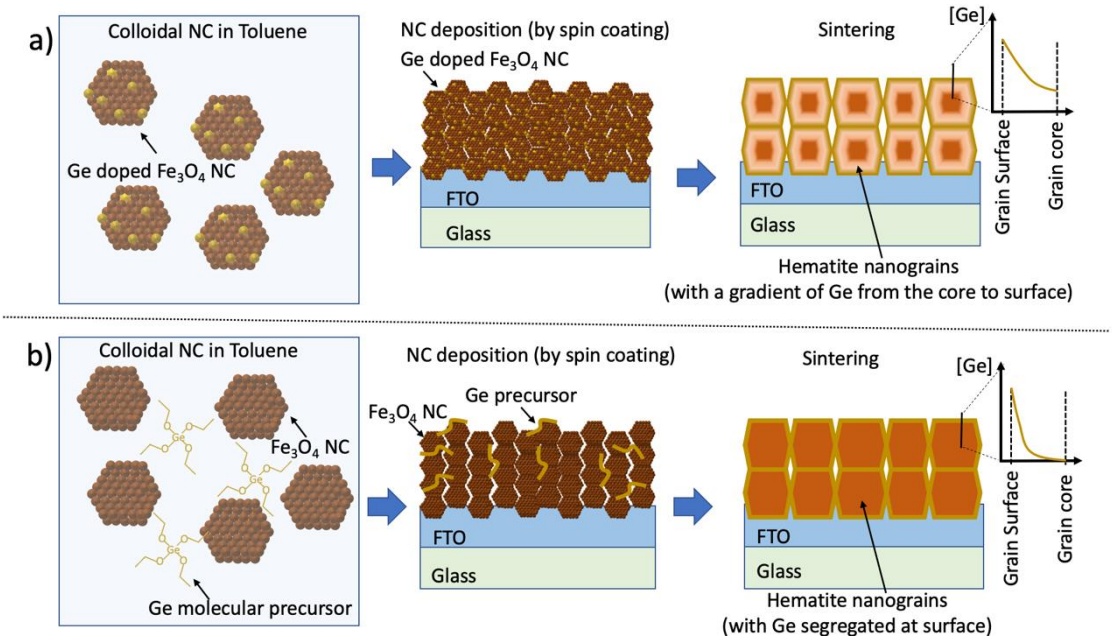

Scheme 3.1. Schematic of the routes used to process Ge-doped hematite photoanode. a) In route FeGe1, Ge is introduced during the synthesis of Fe_3O_4 nanoparticle; b) In route FeGe2, Ge is introduced after the synthesis of Fe_3O_4 NC. The sintering process leads to the hematite photoanode formation with preferential Ge segregation in the hematite grains surface as shown in Scheme 1b.

Because the incorporation of Ge during the synthesis process is an important step in the route used, we performed a detailed characterization of the NC. Figure 3.1 shows the scanning transmission electron microscopy (STEM) analysis of the nanoparticles produced through the FeGe1 route. This approach allowed us to obtain nanoparticles with controlled shape (equiaxial) and size (mean particle size of 7 nm), as illustrated in the STEM high-angle annular dark-field (HAADF) image in Figure 3.1a. Figure 3.1b and c show that these nanoparticles had a high degree of crystallinity (refer to the high-resolution HAADF image in Figure 3.1b). The fast Fourier transform (FFT) analysis (Figure 3.1c) of the oriented nanoparticles (Figure 3.1b) shows an orientation along the [111] axis zone, and it presents the symmetry of the magnetite phase (Fe_3O_4). Elemental chemical analysis, performed by energy dispersive analysis (EDS) coupled with STEM (EDS-STEM), demonstrated that Ge was incorporated in Fe_3O_4 nanoparticles (Figure 1d and insets), with a concentration of 1.7 at% of Ge. It is observed from the EDS map (Figure 3.1d) and line profile analysis (refer to the inset in Figure 3.1d) that Ge was homogeneously dispersed through the nanoparticles, with no sign of segregation. The protocol used in the FeGe2 route was followed to prepare the undoped Fe_3O_4 NC,

resulting in a similar phase, morphology, and size, as revealed by transmission electron microscopy (TEM) analysis (refer to Figure B2 in Appendix B). The undoped Fe_3O_4 nanoparticles were used to obtain a dopant-free hematite photoanode (referred to as Fe pristine).

We performed an X-ray photoemission spectroscopy (XPS) analysis in the FeGe1 and FeGe2 samples (before the sintering process). As we can notice, the sample with Ge-ethoxide (route FeGe2) shows a [Ge]/([Ge]+[Fe]) ratio equal to 0.31, *i.e.*, much higher than the nominal amount added. This result suggests that most of the Ge is located outside the magnetite particles and is not in a solid solution. Moreover, the sample in which Ge was incorporated during the magnetite nanoparticle synthesis (route FeGe1) shows a [Ge]/([Ge]+[Fe]) ratio equal to 0.016, which is close to the nominal one, corroborating the EDS analysis (the nominal [Ge]/([Ge]+[Fe]) ratio is equal to 0.017).

Doped and non-doped hematite photoanodes were systematically characterized to comprehend their chemistry, structure, and morphology. X-ray diffraction (XRD) analyses, illustrated in Figure 3.2a, for all sintered photoanodes exhibited a complete phase transformation from magnetite to hematite after the sintering process. The diffraction peaks were indexed to the hematite phase (JCPDS no. 33-0664) with preferential orientation along the [110] direction for the Fe-pristine and Ge-doped photoanodes (FeGe1 and FeGe2). No Ge-rich phase was identified after the sintering process; only the diffraction peaks assigned to SnO_2 (JCPDS no. 41-14445) were found to be associated with the FTO substrate.

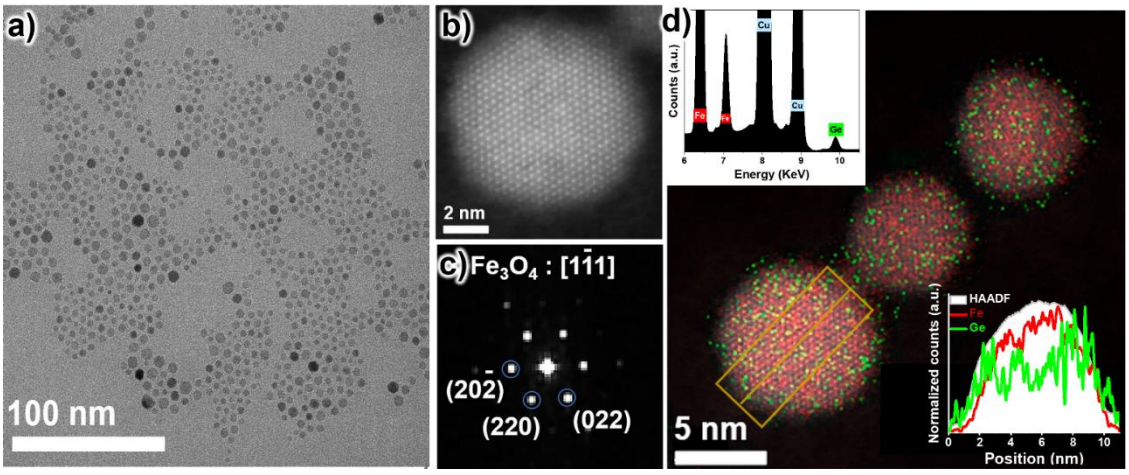

Figure 3.1. STEM characterization of Fe_3O_4 nanoparticle used in route FeGe1. a) Low magnification HAADF-STEM image of Ge-doped Fe_3O_4 nanoparticles; b) high-resolution HAADF-STEM image of Ge-doped Fe_3O_4 nanoparticle oriented along the [111] zone axis; c) FFT of Figure 1b; d) EDS-STEM map analysis of Ge-doped Fe_3O_4

nanoparticles. Insets illustrate the EDS spectrum and the line profile analysis, showing the HAADF, Ge, and Fe signals.

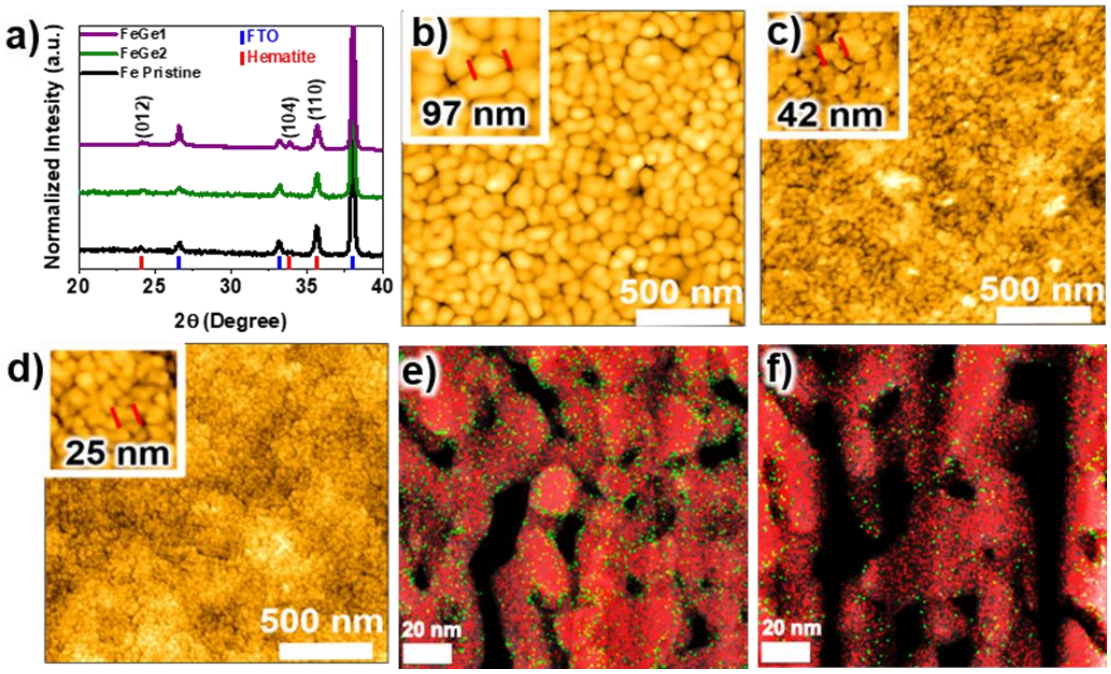

Figure 3.2. Combination of structural and microscopy characterization. a) XRD analysis of FeGe1, FeGe2, and pristine Fe films; b–d) shows non-contact topological AFM images of pristine Fe, FeGe2, and FeGe1 films, respectively. The insets show high magnification AFM images, highlighting the grain size; e) and f) superposition of HAADF-STEM image with EDS map for FeGe1 before (Figure 2e) and after (Figure 2f) the leaching treatment of the film in basic water solution (pH 13.6). The EDS-STEM images show the elemental distribution of Fe (red) and Ge (green).

The atomic force microscopy (AFM) image of the sintered photoanode, shown in Figure 3.2b–d, illustrates that the presence of Ge (samples FeGe1 and FeGe2) promotes a significant reduction in the grain size of the pristine Fe photoanode. Because the initial magnetite NC size ranged from 3 to 8 nm (refer to the TEM analysis in Figure 1 and Figure B2 in Appendix B), an extensive oriented growth process occurred during thermal treatment. This oriented growth process led to the formation of a columnar morphology with textured hematite grains oriented along the [110] direction, as indicated by the XRD results and illustrated in the HAADF STEM image shown in Figure 3.2e-f. Moreover, the

suppression of grain growth due to the presence of Ge suggests segregation at the hematite grain surface during the sintering process.[35] To assess the degree of Ge segregation on the surface of the hematite grains, XPS measurements were performed (refer to Figure B3). From the XPS analysis, the [Ge]/([Fe]+[Ge]) atomic ratio was estimated at approximately 0.32 and 0.42 for FeGe1 and FeGe2 samples, respectively, which are higher than the nominal ratio ([Ge]/([Fe]+[Ge]) = 0.017), indicating a high degree of the Ge^{+4} segregation over the hematite grains surface.

The GeO_2 chemical, which is highly soluble in basic solutions, was explored after the sintering process.[36] Ge-doped hematite photoanodes (FeGe1 and FeGe2) were immersed in 1 M NaOH water solution (pH 13.6) for 60 min. The photoanodes were thereafter washed with ultra-pure water and subjected to XPS, STEM-EDS, and photoelectrochemical measurements. XPS analysis exhibited a significant reduction of the [Ge]/([Fe]+[Ge]) atomic ratio after treatment in basic solution (from 0.32 to 0.28 for FeGe1 and from 0.42 to 0.13 for FeGe2), indicating that part of Ge^{+4}, present in the hematite grains surface, was leached. STEM-EDS analysis performed on FeGe1 photoanode before and after the leaching treatment, illustrated in Figures 3.2e and f, clearly shows the elimination of the Ge present in the hematite pore surface, agreeing well with the results of the XPS analysis.

To evaluate the impact of the added Ge on the performance of the hematite photoanode, photoelectrochemical measurements were performed under standard AM 1.5 G irradiation. The *J*–*V* curves obtained for the photoanodes illuminated on the front side of the electrochemical cell are shown in Figure 3.3a. The Ge–hematite photoanodes exhibited a high photocurrent response compared to the pristine Fe photoanode. The best performance in terms of J_{PH} (J @1.23 V vs RHE) was achieved by photoanode FeGe1 (J_{PH} = 3.2 mA cm^{-2}). This photocurrent value is one of the best among the reported high-performance hematite photoanode systems without multiple modifications, such as the deposition of an overlayer to act as a passivating or co-catalyst layer, or modification of the FTO/hematite interface.[5] The high solubility of GeO_2 in concentrated NaOH solution may raise doubts regarding the stability of this photoanode. However, chronoamperometry tests (see Figure B4, in Appendix B) reveal that this system has high stability, with negligible photocurrent variation as a function of time.

To understand the role of Ge in the PEC properties of the hematite photoanode regarding its water oxidation efficiency, Mott–Schottky analysis was performed for the pristine Fe and FeGe1 photoanodes. The Mott–Schottky plots for both photoanodes,

illustrated in Figure 3.3b, have positive slopes, indicating that electrons are the majority carriers, and we estimated the donor density (N_d) value from this plot. Because V_{fb} is an important parameter in our future analysis, we need to have confidence in this value. Thus, we determined V_{fb} based on the Gärtner–Butler analysis in the presence of a sacrificial reagent (H_2O_2; refer to the details in Figure B5 in Appendix B) to increase the confidence of this measurement.[37] Both N_d and V_{fb} values are summarized in Table 3.1. It is observed that the N_d value for the FeGe1 photoanode is approximately 1.5 times greater than the values estimated for the pristine Fe photoanode. The estimated quantities considering the Mott–Schottky model have been constantly addressed in previous studies based on their inherent uncertainties to describe materials at the nanometric scale.[38, 39] Thus, the observed difference in the N_d values was considered negligible. However, the addition of Ge promotes a small shift in V_{fb} (refer to Table 3.1), unlike other dopants such as Sn and Sb that cause a sensitive anodic shift in V_{fb}.[21, 22]

To gain more insight into the performance of the photoanode, we calculated the absorbed photocurrent density (J_{abs}, considering 100% quantum yield) and overall efficiency ($\eta_{overall} = J_{PH}/J_{abs}$) for the pristine Fe and FeGe1 photoanodes. We listed the results in Table 3.1. The values of J_{abs} were calculated from the ultraviolet-visible (UV-vis) spectra (refer to Figure B6 and the details in Appendix B). Table 3.1 summarizes the $\eta_{overall}$ values, demonstrating that the FeGe1 photoanode is five times higher than that of the undoped photoanode. Although these two systems exhibited similar light-harvesting efficiencies, their overall efficiencies were significantly different.

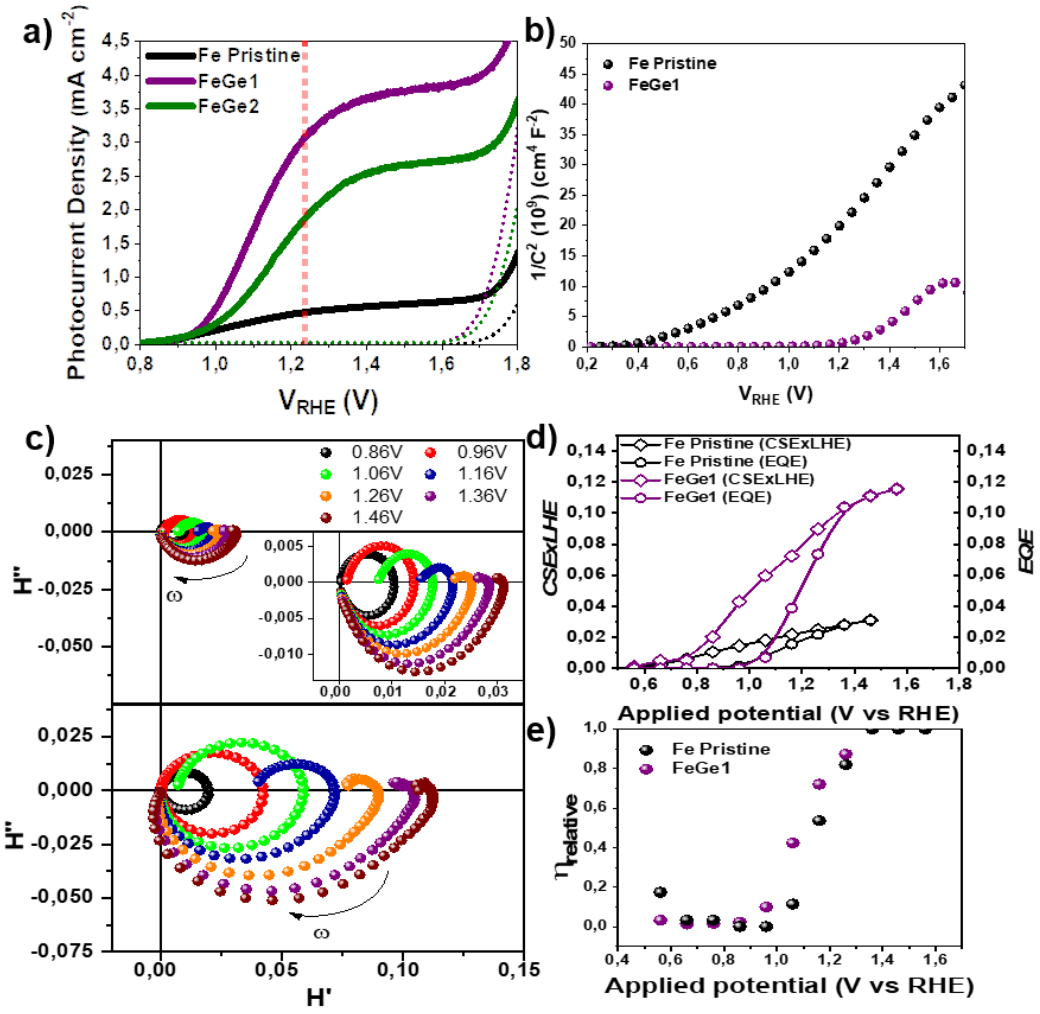

Figure 3.3. Photoelectrochemical characterization of the pristine Fe and FeGe1 samples. a) Current density versus potential curves (J x V_{RHE}) measured in darkness and under illumination for the pristine Fe, FeGe1, and FeGe2 samples. This experiment was conducted using an aqueous electrolyte with 13.6 pH (NaOH solution) and 100 mW cm^{-1} light intensity; b) Mott–Schottky plots measured at 1 kHz frequency in 1 M NaOH solution in darkness for the pristine Fe and FeGe1 samples; c) IMPS spectra obtained for pristine hematite and Ge–hematite at the potentials indicated under front-side illumination using a blue LED (470 nm) in a 1 M NaOH aqueous solution. Potential dependence of d) charge separation efficiency at a given light harvesting efficiency (*CSE* x *LHE*) and external quantum efficiency (*EQE*) and e) relative hole transfer efficiency (η_{rel}) obtained from IMPS plots.

Table 3.1. Jabs, J_{PH}, $\eta_{overall}$ ($\eta_{overall} = J_{PH}/J_{abs}$), N_d, and V_{fb} for pristine Fe and FeGe1 samples that exhibited the highest photocurrent response during sunlight-assisted water oxidation. N_d value was estimated from the Mott–Schottky plot and V_{fb} from the Gartner approach.[37,40] J_{abs}, J_{PH}, and $\eta_{overall}$ were determined from optical and photo-electrochemical measurements.

Sample	J_{abs} (mA cm^{-2})	J_{PH} (@1.23V vs V_{RHE}) (mA cm^{-2})	$\eta_{overall}$ (J_{PH}/J_{abs})	N_d (cm^{-3}) ($x10^{19}$)	V_{fb} (V/V_{RHE})
Pristine Fe	10.1	0.5	0.05	3.9	0.68
FeGe1	11.7	3.2	0.27	5.9	0.78

To better understand the role of Ge in the charge carrier dynamics of hematite photoanodes, we performed intensity-modulated photocurrent spectroscopy (IMPS) measurements. Figure 3.3c shows the IMPS plot for the pristine Fe and FeGe1 photoanodes measured from 0.56 to 1.46 V vs RHE under blue light-emitting diode (LED) irradiation. For the pristine Fe hematite (Figure 3.3c, top), it is observed that at high frequencies (ω), the IMPS transfer function (H) values are close to zero; as the frequency decreases, the H data points form a semicircle in the fourth quadrant until they intercept the real axis at the intermediate frequency, which represents the charge separation efficiency at a given light-harvesting efficiency (*LHE*), neglecting the surface recombination and charge transfer, as expressed in Equation 3.4 as follows:[41-43]

$$Intercept_{wintermediate} = CSE\ x\ LHE \quad (3.4)$$

$$Intercept_{w\to 0} = EQE \quad (3.5)$$

At lower frequencies, a second semicircle that depended on the applied potential was obtained in the first quadrant. As the applied voltage increases, the intercept at low frequency, which is also associated with the external quantum efficiency (*EQE*, Equation 3.5), moves away from the origin, thereby increasing the photocurrent, as also observed in the *J–V* curves. At V > 1.26 V, the first quadrant semicircle disappears, indicating that

the hole transfer is significantly faster than the surface recombination.[44] A similar trend is observed for FeGe1 film (Figure 3.3c, bottom) at the same potential ranges in which both semicircles are clearly distinguished from 0.8 to 1.26 V. Interestingly, at more positive potentials and high frequencies, the IMPS function crosses from the third to the fourth quadrant, suggesting that the Ge insertion increases the electron diffusion length in hematite.[45]

Although the IMPS measurements of both films present a similar potential dependence, it is noted that the intercepts, *CSE* x *LHE* and *EQE* (Equations 3.4 and 3.5), are significantly different. Figure 3.3d shows the *CSE* x *LHE* and *EQE* values extracted from Figure 3.3c as a function of the applied potential. Ranging from 0.5 to 0.8 V, the achieved *CSE* x *LHE* values are equivalent for both photoanodes, indicating an equal separation efficiency in this range. As the potential increased, the *CSE* x *LHE* of FeGe1 film became superior to that of the pristine hematite, reaching higher values (~6x at 1.46 V). The reason for this difference will be explained later. For *EQE*, both films exhibited values close to zero ranging from 0.5 to 0.96 V; at more positive potentials, an increasing trend is noticeable until *EQE* becomes equal to *CSE* X *LHE* at V > than 1.3 V. Interestingly, an area between *CSE* x *LHE* and *EQE* are observed for both films, indicating that, ranging from 0.5 to 1.25 V, an important portion of photogenerated holes are lost through surface recombination.

The IMPS spectra were also analyzed to extract the transfer and surface constants (k_{tr} and k_{sr}), and consequently, calculate the relative hole transfer efficiency (η_{rel}), defined as the ratio between k_{tr} and ($k_{tr} + k_{sr}$). The identical values and trends of η_{rel}, displayed in Figure 3.3e, show that the surface of the two photoanodes (Fe pristine and FeGe1) present surfaces with similar behavior, concerning the charge transfer process. Thus, after the leaching treatment, the surface charge transfer processes in the FeGe1 photoanode are dominated by the new hematite surface (with residual Ge), which must be like those of the pristine Fe hematite surface.

Based on previous results, the addition of Ge should improve the charge carrier separation process, increasing the conductivity of the majority carriers (e^-). To evaluate this hypothesis, conductive AFM (C-AFM) analysis was performed for the pristine Fe and FeGe1 photoanodes, as shown in Figures 3.4a and b, respectively. In C-AFM, an electrically conductive tip is placed in contact with the photoanode surface, thereby completing a circuit and allowing charge transfer through different regions of the photoanodes (refer to Figure 3.4a). A simple qualitative analysis of the C-AFM images

shows that the FeGe1 photoanode has a higher conductivity (represented by the high current and bright area in Figure 3.4c) than the pristine Fe photoanode (Figure 3.4b). However, a semiquantitative estimation of this conductivity can also be performed. Because the same conductive tip was used to perform the C-AFM measurements of both photoanode surfaces, the current density (J = nA nm^{-2}) can be estimated by considering the average value of the current in the analyzed area. Considering the applied electric field (E) (v/film thickness), the ratio between the conductivity of the pristine Fe (σFeP) and FeGe1 (σFeGe1) photoanodes (remembering that $J = \sigma E$) was estimated. This analysis demonstrates that σFeGe1~34 σFeP. The electronic conductivity of the Ge-modified sample was more than one order of magnitude higher than that of the pristine sample.

The conductivity can be described as the product of the concentration (N_d) and mobility (μ) of charge carriers (q): $\sigma = (N_d\ q)\ \mu$. Revisiting the Mott–Schottky results obtained in this study, the addition of Ge does not increase in N_d. Thus, Ge addition can be associated with a gain in the mobility of the majority carriers (e^-). Considering the values of N_d and the relationship between σFeGe1~34 σFeP, the electron mobility for the FeGe1 photoanode was estimated to range from 22 to 34 times higher than that for the pristine Fe photoanode.

The improvement in carrier mobility due to the doping effect has been reported in previous studies proposed that the high performance of Ti-doped hematite photoanodes is associated with an increase in N_d and a prolonged carrier lifetime.[46, 47] More recently, Zhang *et al.*[48] using a combination of solid-state electronic transport and PEC characterizations, reported that the improvement of electron transport and charge carrier efficiency in Mo-doped $BiVO_4$ is due to the lowered small polaron hopping barrier. Similarly, Pastor *et al.*[49] proposed that the deleterious effect and polaronic states formation could be avoided during the materials fabrication process for PEC applications.[25] The origin of the low electron mobility in hematite can be attributed to the high localization of small polarons[18,50] that require a high activation energy to hop to the adjacent atom. The addition of Ge to hematite should affect the degree of localization of the small polarons, boosting their transport and photocurrent. Because the small polaron localization of the photoexcited carrier is wavelength-dependent, we used the absorbed photon-to-current conversion efficiency (APCE) to understand the effect of Ge on the carrier mobility of hematite. The APCE as a function of potential was determined (for details about the APCE calculation, refer to the experimental procedure) by considering

three different wavelengths. Because the localization effect of small polarons is more pronounced in the wavelength near the hematite band edge, the excitation at an energy slightly higher than the bandgap (where there is an efficient small polaron formation) and two other energies where a mixture between polaron formation and charge mobility occurs were selected.[5, 19, 37, 49]

Considering that most of the charge separation process in hematite occurs in the depletion layer region, that is, for $V_{RHE} > V_{fb}$, we corrected the applied potential V_{RHE} by V_{fb} (V_{RHE} - V_{fb}). The results are shown in Figure 3.4d–h. The addition of Ge (FeGe1 photoanode) resulted in a significantly higher APCE value, regardless of the excitation wavelength used to perform the measurements. At 627 nm excitation (Figure 3.4d), we observed that FeGe1 and pristine Fe photoanodes exhibited an APCE signal only for $V_{RHE} > V_{fb}$.

However, we note that the undoped photoanode (pristine Fe) requires a higher anodic potential for the water oxidation process to occur, demonstrating that the localization effect of small polarons is more pronounced in this sample. This result strongly indicates that the addition of Ge modified the formation of small polarons, thus increasing the lifetime of the carriers. At more energetic excitations (532 and 470 nm, as shown in Figure 3.4e–h), we observed a significant increase in the APCE as a function of potential, clearly indicating an increase in the mobility of charge carriers. Moreover, we noticed that the sample with Ge (FeGe1) presents an APCE signal even at a potential lower than V_{fb} (refer to Figure 3.4g and h), suggesting that we can extract charges close to the surface of hematite, even without the aid of band bending. The pristine Fe sample exhibited only an APCE signal at $V_{RHE} > V_{fb}$, even for more energetic excitations.

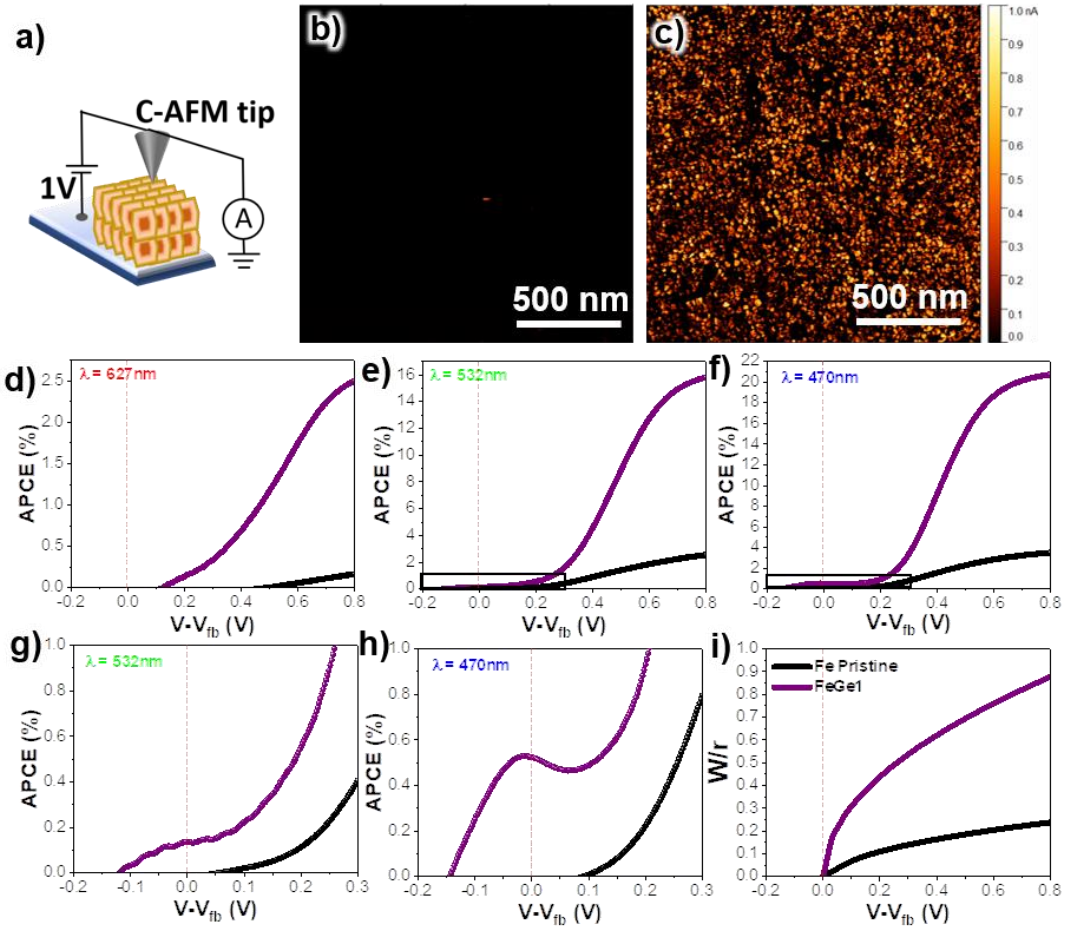

Figure 3.4. C-AFM, APCE, and depletion layer width (*W*) analysis for the pristine Fe and FeGe1 photoanodes. a) Schematic of the experimental set-up used to measure C-AFM; b) C-AFM image of the pristine Fe photoanode; c) C-AFM image of FeGe1 sample; d) APCE measurement as a function of the correctly applied potential ($V-V_{fb}$) measured with an excitation of 627 nm; e) APCE measurement as a function of ($V-V_{fb}$) measured with an excitation of 532 nm; f) APCE measurement as a function of ($V-V_{fb}$) measured with an excitation of 470 nm; g) Zoom of the APCE curve (highlighted area) of Figure 3.4e; h) Zoom of the APCE curve (highlighted area) of Figure 3.4f; and i) *W* normalized by the characteristic morphological feature size (*W*/rG, where rG denotes the mean grain radius) as a function of ($V-V_{fb}$).

Finally, we discuss the effect of grain size reduction after the sintering step, promoted by the addition of Ge (a side effect), on the photoelectrochemical performance. As illustrated in Figure B7a (refer to Appendix B), most of the photocurrent was generated at $V_{RHE} > V_{fb}$, indicating that the charge separation process occurred mostly in

the depletion layer width (*W*). Figure B7b shows the evolution of *W* (assuming classical depletion layer theory[51]) as a function of the applied potential for the pristine Fe and FeGe1 photoanodes. As the two samples differ in morphology, mainly grain size (refer to Figure 3.2b–d and Figure B3 in Appendix B), a direct comparison between the samples becomes unfeasible. Thus, we normalized *W* by a characteristic morphological feature size (mean grain radius, rG), and the results are plotted in Figure 3.4i. The *W*/rG ratio is a parameter related to the active volume fraction of the hematite used in the light-assisted water-splitting process.[51] We observed that the reduction in the grain size caused by the addition of Ge led to better use of the active volume fraction of the material (a higher W/rG ratio) when compared to non-doped hematite.

5. CONCLUSIONS

The results presented here demonstrate that the strategy of using Ge doping during nanoparticle synthesis (FeGe1 route) is fundamental for obtaining a high-performance photoanode. Moreover, we believe that efficient doping with Ge became viable because magnetite was used as the hematite precursor. Magnetite has an inverted spinel-like cubic structure that is more tolerant to the formation of defects than the corundum-like structure of hematite.[52] With the phase transformation during sintering, the FeGe1 route allowed greater control of Ge dispersion, as demonstrated by the XPS data. After the leaching treatment, we reported the elimination of part of Ge. Thereafter, we observed (through IMPS measurements) that the FeGe1 photoanode had a surface with similar behavior, concerning the charge transfer process, to that of the pristine Fe photoanode. Furthermore, C-AFM measurements demonstrate that Ge improves the electronic conductivity and increases the majority carrier mobility. Measurements of APCE as a function of the applied potential, performed at varying excitation wavelengths, show that Ge interferes with the formation of small polarons, making the charges more mobile (delocalized), thus favoring the process of photoinduced charge separation. In addition, Ge helps to control the photoanode morphology by inhibiting grain growth during the sintering process. Based on these characteristics, we conclude that Ge is an ideal dopant for improving the charge separation in hematite photoanodes.

6. ACKNOWLEDGEMENTS

The authors acknowledge financial support from FAPESP (projects CEPID – 2013/07296-2, 2017/02317-2, 2017/03135, and 2018/05159-1), and CAPES – Finance Code 001 (process 88887.310931/2018-00). All Brazilian agencies are gratefully acknowledged.

7. REFERENCES

1. A. J. Bard and M. A. Fox, Accounts of Chemical Research, 1995, 28, 141-145.
2. M. G. Walter, E. L. Warren, J. R. McKone, S. W. Boettcher, Q. Mi, E. A. Santori and N. S. Lewis, Chemical Reviews, 2010, 110, 6446-6473.
3. K. Sivula, F. Le Formal and M. Grätzel, ChemSusChem, 2011, 4, 432-449.
4. I. S. Cho, H. S. Han, M. Logar, J. Park and X. Zheng, Advanced Energy Materials, 2016, 6, 1501840.
5. C. Li, Z. Luo, T. Wang and J. Gong, Advanced Materials, 2018, 30, 1707502.
6. S. D. Tilley, M. Cornuz, K. Sivula and M. Grätzel, Angewandte Chemie International Edition, 2010, 49, 6405-6408.
7. H. Zhang, D. Li, W. J. Byun, X. Wang, T. J. Shin, H. Y. Jeong, H. Han, C. Li and J. S. Lee, Nature Communications, 2020, 11, 4622.
8. Z. Luo, T. Wang, J. Zhang, C. Li, H. Li and J. Gong, Angewandte Chemie International Edition, 2017, 56, 12878-12882.
9. Z. Zhang, H. Nagashima and T. Tachikawa, Angewandte Chemie International Edition, 2020, 59, 9047-9054.
10. J. Y. Kim, G. Magesh, D. H. Youn, J.-W. Jang, J. Kubota, K. Domen and J. S. Lee, Scientific Reports, 2013, 3, 2681.
11. T. H. Jeon, G.-h. Moon, H. Park and W. Choi, Nano Energy, 2017, 39, 211-218.
12. J. Li, H. Chen, C. A. Triana and G. R. Patzke, Angewandte Chemie International Edition, 2021, 60, 18380-18396.
13. A. L. M. Freitas, D. N. F. Muche, E. R. Leite and F. L. Souza, Journal of the American Ceramic Society, 2020, 103, 6833-6846.
14. A. G. Hufnagel, H. Hajiyani, S. Zhang, T. Li, O. Kasian, B. Gault, B. Breitbach, T. Bein, D. Fattakhova-Rohlfing, C. Scheu and R. Pentcheva, Advanced Functional Materials, 2018, 28, 1804472.

15. C. X. Kronawitter, I. Zegkinoglou, S. H. Shen, P. Liao, I. S. Cho, O. Zandi, Y. S. Liu, K. Lashgari, G. Westin, J. H. Guo, F. J. Himpsel, E. A. Carter, X. L. Zheng, T. W. Hamann, B. E. Koel, S. S. Mao and L. Vayssieres, Energy & Environmental Science, 2014, 7, 3100-3121.

16. M. Cornuz, M. Grätzel and K. Sivula, Chemical Vapor Deposition, 2010, 16, 291-295.

17. S. C. Warren, K. Voïtchovsky, H. Dotan, C. M. Leroy, M. Cornuz, F. Stellacci, C. Hébert, A. Rothschild and M. Grätzel, Nature materials, 2013, 12, 842-849.

18. A. J. E. Rettie, W. D. Chemelewski, D. Emin and C. B. Mullins, The Journal of Physical Chemistry Letters, 2016, 7, 471-479.

19. L. M. Carneiro, S. K. Cushing, C. Liu, Y. Su, P. Yang, A. P. Alivisatos and S. R. Leone, Nature Materials, 2017, 16, 819-825.

20. J. B. Souza Junior, F. L. Souza, L. Vayssieres and O. K. Varghese, Applied Physics Letters, 2021, 119, 200501.

21. R. H. Gonçalves and E. R. Leite, Energy & Environmental Science, 2014, 7, 2250-2254.

22. A. E. Nogueira, M. R. Santos Soares, J. B. Souza Junior, C. A. Ospina Ramirez, F. L. Souza and E. R. Leite, Journal of Materials Chemistry A, 2019, 7, 16992-16998.

23. M. R. S. Soares, C. A. R. Costa, E. M. Lanzoni, J. Bettini, C. A. O. Ramirez, F. L. Souza, E. Longo and E. R. Leite, Advanced Electronic Materials, 2019, 5, 1900065.

24. F. C. de Lima, G. R. Schleder, J. B. Souza Junior, F. L. Souza, F. B. Destro, R. H. Miwa, E. R. Leite and A. Fazzio, Applied Physics Letters, 2021, 118, 201602.

25. J. Liu, C. Liang, G. Xu, Z. Tian, G. Shao and L. Zhang, Nano Energy, 2013, 2, 328-336.

26. L. Zhao, J. Xiao, H. Huang, Q. Huang, Y. Zhao and Y. Li, International Journal of Hydrogen Energy, 2018, 43, 12646-12652.

27. P. Liao, M. C. Toroker and E. A. Carter, Nano Letters, 2011, 11, 1775-1781.

28. Z. Zhou, P. Huo, L. Guo and O. V. Prezhdo, The Journal of Physical Chemistry C, 2015, 119, 26303-26310.

29. J. Liu, C. Liang, H. Zhang, Z. Tian and S. Zhang, The Journal of Physical Chemistry C, 2012, 116, 4986-4992.

30. T. J. Smart, V. U. Baltazar, M. Chen, B. Yao, K. Mayford, F. Bridges, Y. Li and Y. Ping, Chemistry of Materials, 2021, 33, 4390-4398.

31. K.-Y. Yoon, J. Park, M. Jung, S.-G. Ji, H. Lee, J. H. Seo, M.-J. Kwak, S. Il Seok, J. H. Lee and J.-H. Jang, Nature Communications, 2021, 12, 4309.

32. V. Agafonov, D. Michel, M. Perez, Jorba and M. Fedoroff, Materials Research Bulletin, 1984, 19, 233-239.

33. R. H. Gonçalves, B. H. R. Lima and E. R. Leite, Journal of the American Chemical Society, 2011, 133, 6012-6019.

34. J. H. Kennedy and K. W. Frese, Journal of The Electrochemical Society, 1978, 125, 723-726.

35. E. R. Leite, A. P. Maciel, I. T. Weber, P. N. Lisboa-Filho, E. Longo, C. O. Paiva-Santos, A. V. C. Andrade, C. A. Pakoscimas, Y. Maniette and W. H. Schreiner, Advanced Materials, 2002, 14, 905-908.

36. O. H. Johnson, Chemical Reviews, 1952, 51, 431-469.

37. A. Hankin, F. E. Bedoya-Lora, J. C. Alexander, A. Regoutz and G. H. Kelsall, Journal of Materials Chemistry A, 2019, 7, 26162-26176.

38. K. Sivula, ACS Energy Letters, 2021, 6, 2549-2551.

39. M. G. Walter, E. L. Warren, J. R. McKone, S. W. Boettcher, Q. Mi, E. A. Santori and N. S. Lewis, Chemical Reviews, 2011, 111, 5815-5815.

40. W. W. Gärtner, Physical Review, 1959, 116, 84-87.

41. I. Rodríguez-Gutiérrez, R. García-Rodríguez, M. Rodríguez-Pérez, A. Vega-Poot, G. Rodríguez Gattorno, B. A. Parkinson and G. Oskam, The Journal of Physical Chemistry C, 2018, 122, 27169-27179.

42. I. Rodriguez-Gutierrez, J. B. Souza Junior, E. R. Leite, L. Vayssieres and F. L. Souza, Applied Physics Letters, 2021, 119, 071602.

43. C. Y. Cummings, F. Marken, L. M. Peter, A. A. Tahir and K. G. U. Wijayantha, Chemical Communications, 2012, 48, 2027-2029.

44. L. M. Peter, K. G. U. Wijayantha and A. A. Tahir, Faraday Discussions, 2012, 155, 309-322.

45. A. Bou, H. Āboliņš, A. Ashoka, H. Cruanyes, A. Guerrero, F. Deschler and J. Bisquert, ACS Energy Letters, 2021, 6, 2248-2255.

46. B. Zhao, T. C. Kaspar, T. C. Droubay, J. McCloy, M. E. Bowden, V. Shutthanandan, S. M. Heald and S. A. Chambers, Physical Review B, 2011, 84, 245325.

47. G. Wang, Y. Ling, D. A. Wheeler, K. E. N. George, K. Horsley, C. Heske, J. Z. Zhang and Y. Li, Nano Letters, 2011, 11, 3503-3509.

48. W. Zhang, F. Wu, J. Li, D. Yan, J. Tao, Y. Ping and M. Liu, ACS Energy Letters, 2018, 3, 2232-2239.
49. E. Pastor, J.-S. Park, L. Steier, S. Kim, M. Grätzel, J. R. Durrant, A. Walsh and A. A. Bakulin, Nature Communications, 2019, 10, 3962.
50. Y. Fan, Y. Lin, K. Wang, K. H. L. Zhang and Y. Yang, Physical Review B, 2021, 103, 085206.
51. S.C. Warren, K. Voitchovsky, H. Dotan, C.M. Leroy, M. Cornuz, F. Stellaci, C. Hérbet, A. Rothschild and M. Graetzel, Natute Materials, 2013, 12, 842-849
52. R. M. a. S. Cornell, U., in The Iron Oxides, ed. R. M. a. S. Cornell, U., 2003, DOI: https://doi.org/10.1002/3527602097.ch2, pp. 9-38.

Chapter 4

CONCLUSIONS AND OUTLOOK

1. GENERAL CONCLUSIONS

Firstly, using the magnetic field in colloidal nanoparticle deposition is a promising route to produce thin films for photoelectrochemical applications. Our group has an experience with this method of deposition. However, it was necessary to carry out a detailed study of how the effect of the magnetic field affects the fabrication of hematite films. In general, the process with the magnetic field showed that its use contributes to better control of the morphology and efficiency of pure hematite films.

Finally, the strategy of the doping process for improving the hematite photoanodes through Germanium dopant presented excellent results. A dopant is essential for better efficiency of hematite-based films since it has some limitations that can be overcome by adding some elements. The doping architecture studied showed a route for manufacturing hematite films in addition to the one already known by our group. This new route showed good results regarding the doping effect of the hematite films with germanium, showing high photocurrent results. The use of germanium provided an increase in the conductivity and electronic mobility of the films properties directly linked to the performance of these photoanodes.

2. FUTURE DIRECTIONS

The doped hematite photoanode performance reported in the thesis can be compared with the best literature results, considering only doped hematite films without other layers and cocatalysts. However, these results are still far from the ideal photocurrent values expected from hematite, making new studies necessary to improve these values. Doping with germanium promoted the increase of electronic conductivity and increased the majority carrier mobility. However, the dopant demonstrated a different behavior with different wavelength photon flux irradiation. Front this, a new detailed study about the influence of the wavelength photon flux can be realized. We believe these different behaviors may be associated with improving the mobility of hematite holes.

Chapter 5

APPENDIX A

Supplementary information for "The influence of the magnetic field and heat treatment on the thin film colloidal deposition process of magnetic nanoparticles: The search for high-efficiency hematite photoanodes"

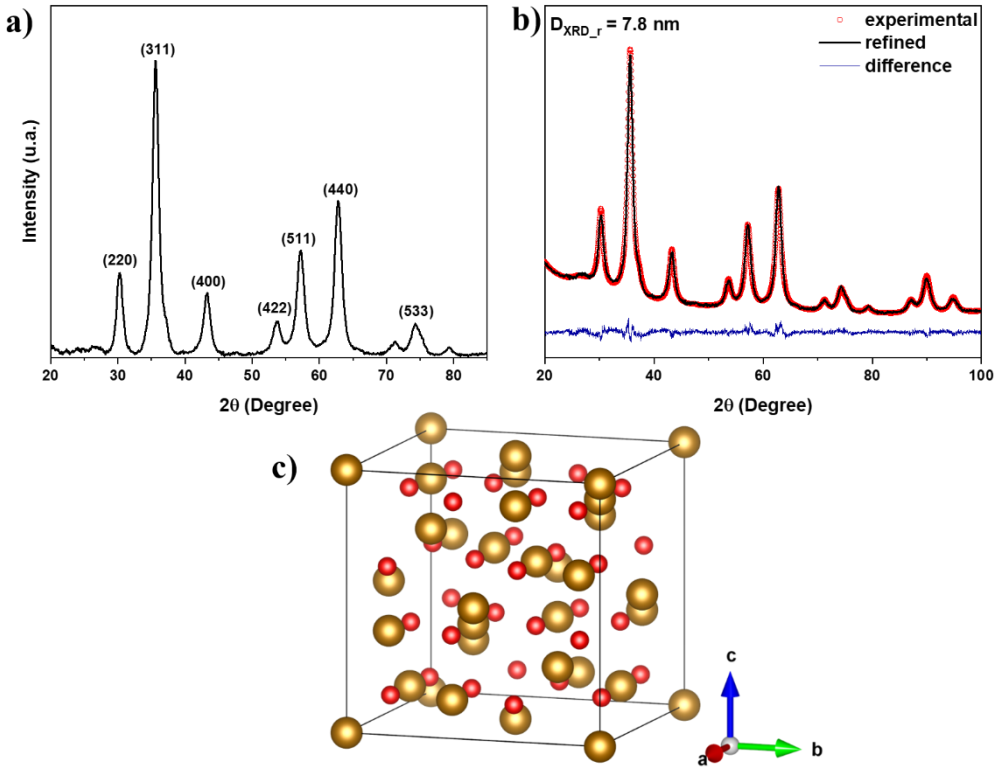

Figure 5.1. (a) X-ray diffraction patterns of magnetite nanoparticles: (a) experimental; (b) Rietveld refinement; and (c) unit cell of magnetite.

Table 5.1. Rietveld size, lattice parameter, Rwp extracted from simulated data, and R-Bragg.

	Rietveld size (nm)	**Lattice parameter (Å)**	**Rwp (%)**	**R-Bragg**
Magnetite nanoparticles	7.8	8.378	8.54	0.956

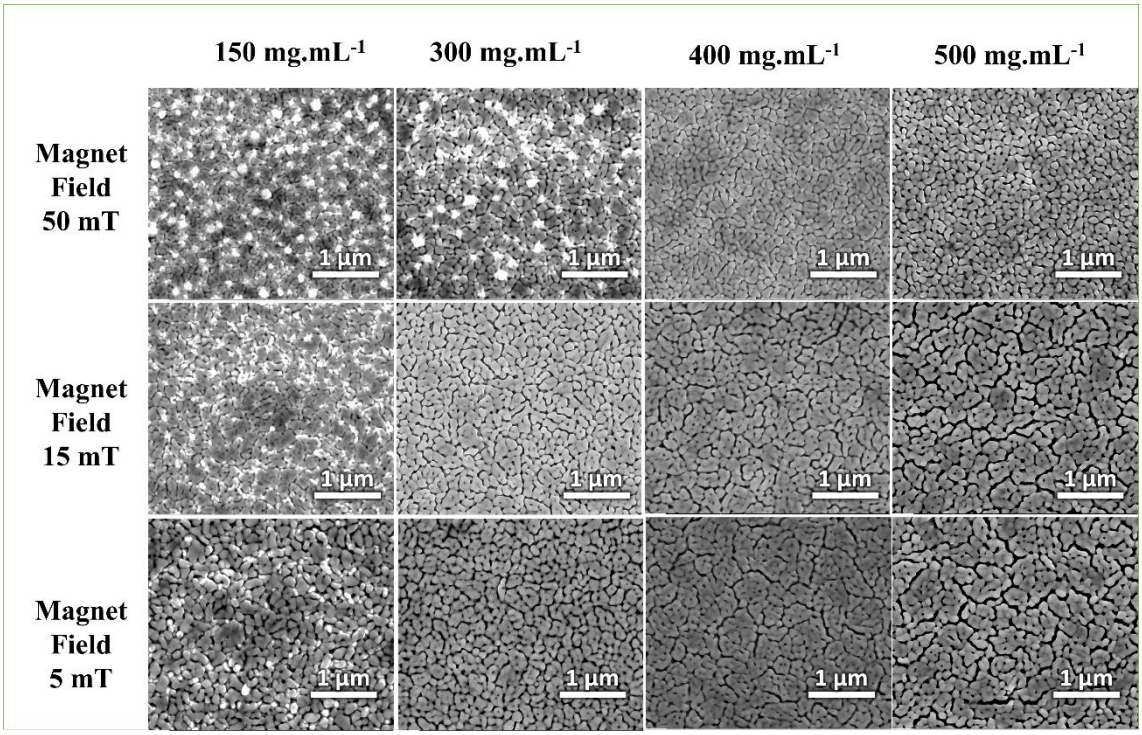

Figure 5.2. SEM images (top-view) of hematite nanostructures obtained with different magnetic fields and nanoparticles concentrations.

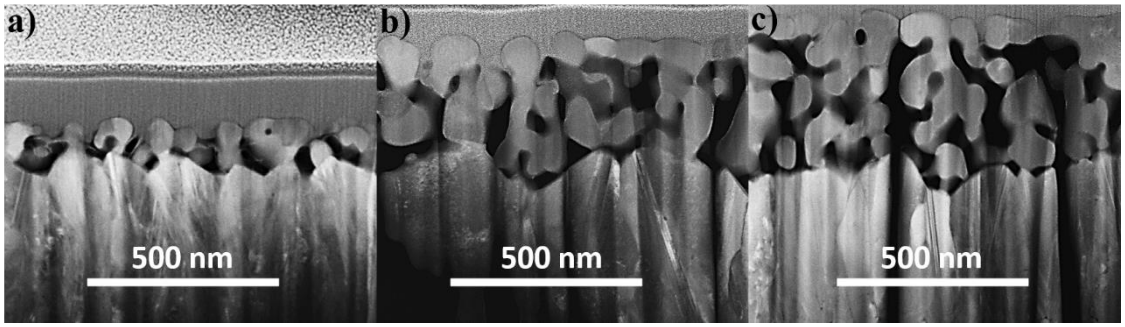

Figure 5.3. SEM images cross section of hematite nanostructures obtained with 500 mg mL-1 at: (a) 50 mT magnetic field; 15 mT magnetic field; and 5 mT magnetic field.

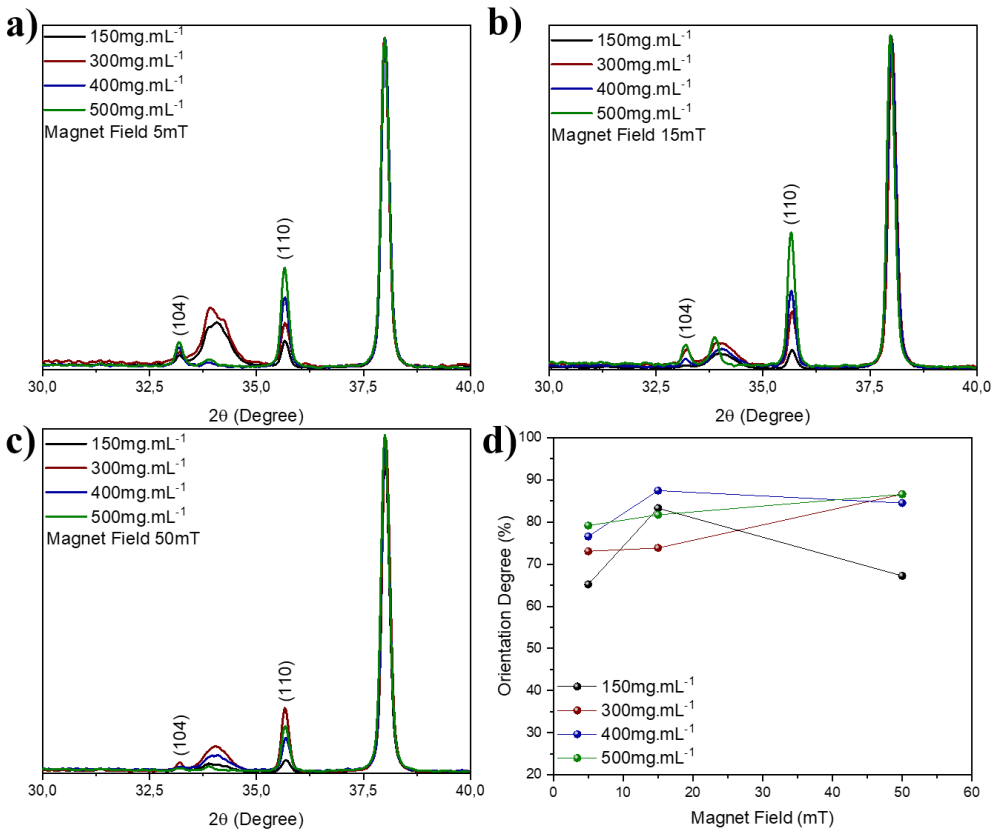

Figure 5.4. X-ray diffraction peaks of hematite thin films obtained at: (a) 5 mT magnetic field; (b) 15 mT magnetic field; 50 mT magnetic field; and (d) percentage of film orientation along the 110 plane as a function of the magnetic field.

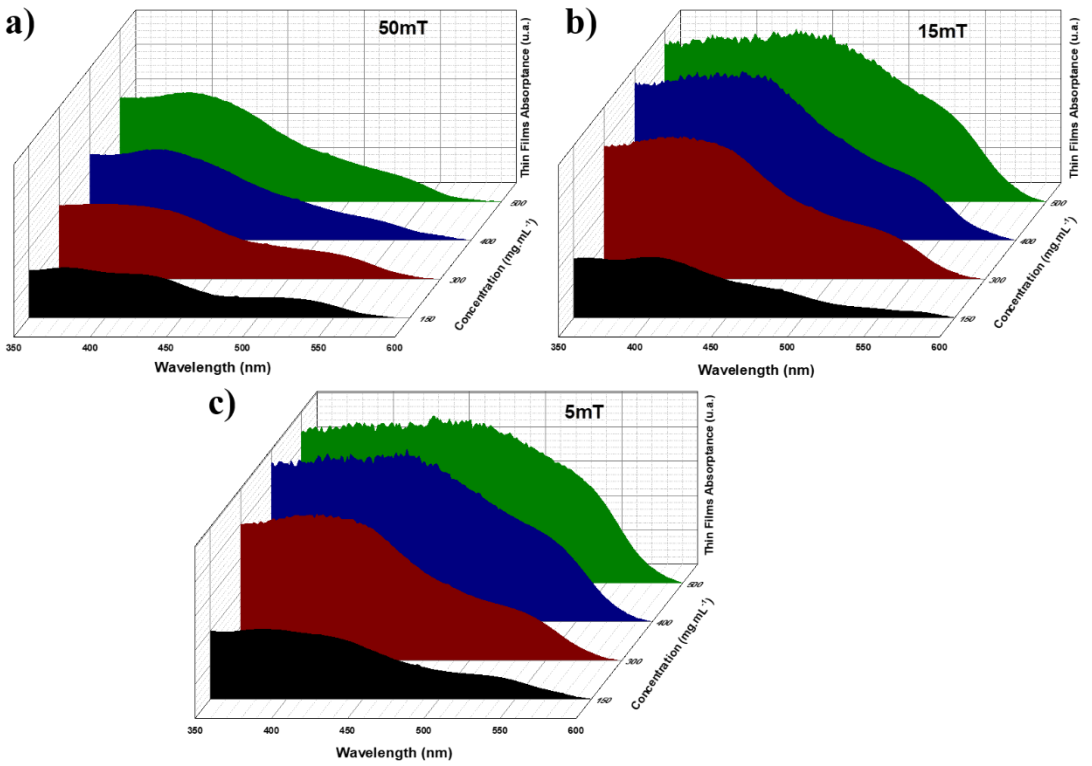

Figure 5.5. UV-vis spectra of the hematite films prepared with different nanoparticles concentration at: (a) 5 mT magnetic field; 15 mT magnetic field; and (c) 50 mT magnetic field.

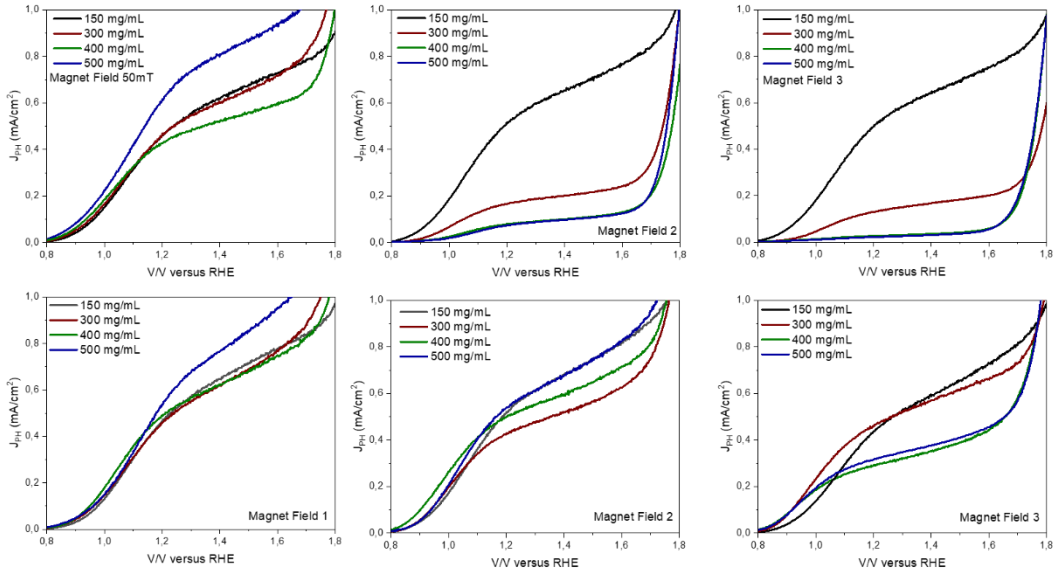

Figure 5.6. Current-potential curves of hematite thin films obtained with different nanoparticles concentration at: (a) 5 mT magnetic field under front illumination; (b) 14 mT magnetic field under front illumination; (c) 50 mT magnetic field under front illumination; (d) 5 mT magnetic field under back illumination; (e) 15 mT magnetic field under back illumination; and (f) 50 mT magnetic field under back illumination.

Table 5.2. Parameters of two-teta (2Θ), full with at half maximum (FWHM), and crystallite size of hematite thin films obtained with different concentration ate 5, 15 and 50 mT magnetic field.

	150 mg.mL^{-1}			**300 mg.mL^{-1}**			**400 mg.mL^{-1}**			**500 mg.mL^{-1}**		
	2Θ (°)	**FWHM**	**Crystallite size (nm)**	**2Θ (°)**	**FWHM**	**Crystallite size (nm**	**2Θ (°)**	**FWHM**	**Crystallite size (nm**	**2Θ (°)**	**FWHM**	**Crystallite size (nm**
5mT	35.668	0.191	43.7	35.675	0.222	37.6	35.664	0.204	40.9	35.666	0.199	42.0
15mT	35.686	0.200	41.8	35.690	0.205	40.7	35.667	0.193	43.3	35.667	0.193	43.3
50mT	35.688	0.214	38.9	35.674	0.200	42.4	35.692	0.202	41.3	35.679	0.199	42.0

Chapter 6

APPENDIX B

Supplementary information for "Ideal dopant to increase charge separation efficiency in Hematite photoanodes: Germanium"

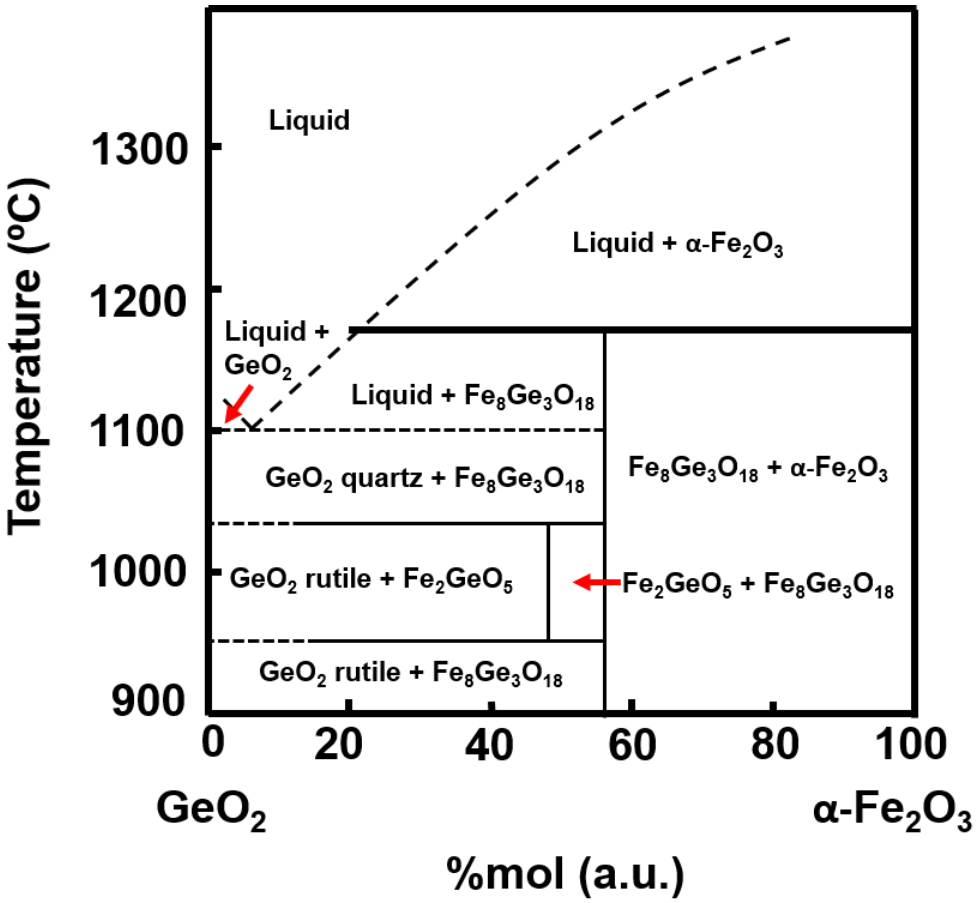

Figure 6. 1. Fe_2O_3 – GeO_2 phase diagram.[1] (Adapted and reproduced with permission. Copyright 1984, Elsevier Ltd.)

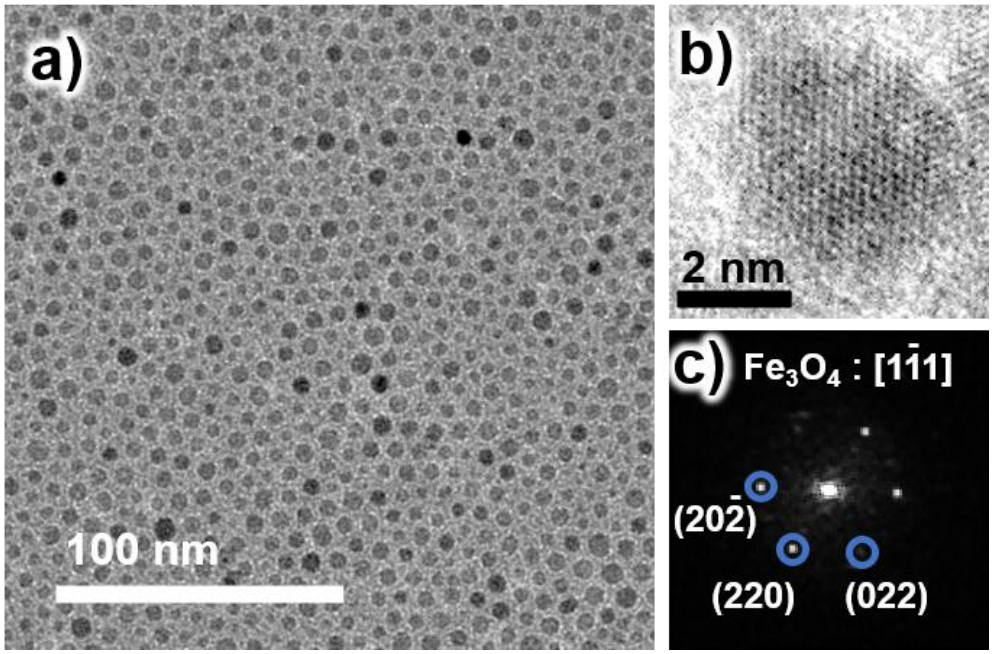

Figure 6.2. TEM characterization of the pure Fe_3O_4 nanoparticles. a) Low TEM image of the Fe_3O_4 nanoparticles; b) high resolution TEM image of Fe_3O_4 nanoparticle oriented along the [111] zone axis; c) FFT of the Figure 6.2b.

Table 6.1. Experimental results of photocurrent density of different Ge concentrations incorporated in magnetite synthesis.

[Ge] (%)	J_{photo} ***(mA cm^{-2})***
3.2	1.8
1.7	2.4
0.8	1.8
0.4	1.3

Table 6.2. Experimental results of photocurrent density of different deposited layers by spin coating method.

Layers	J_{photo} ***(mA cm^{-2})***
1 Layer	2.4
2 Layers	3.2
3 Layers	3.2
4 Layers	2.7

Table 6.3. Experimental results of photocurrent density of different sintering times of FeGe1 films at 850 ºC.

Sintering time (minutes)	J_{photo} ***(mA cm^{-2})***
1	0.1
2	1.3
3	1.8
4	3.2
5	2.8
10	2.0
15	2.2
20	1.7

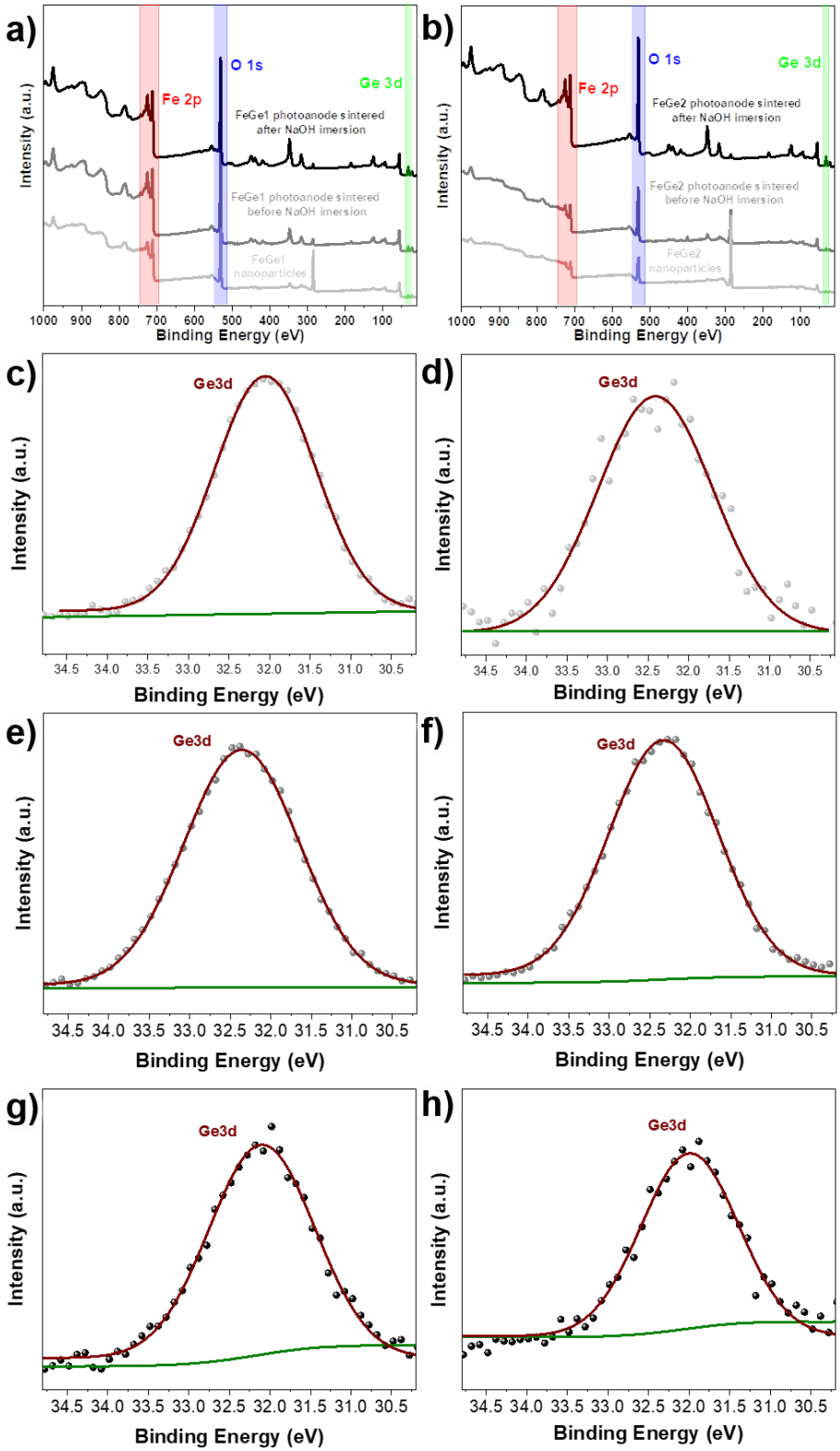

Figure 6.3. XPS spectra of the Ge–hematite: (a) survey spectrum of FeGe1 nanoparticles, FeGe1 photoanode sintered before and after the contact to NaOH solution; (b) survey spectrum of FeGe2 nanoparticles, FeGe2 photoanode sintered before and after the contact to NaOH solution; High-resolution XPS spectrum of the Ge 3d region: (c) FeGe1 nanoparticles, (d) FeGe2 nanoparticles, (e) FeGe1 photoanode before leaching with NaOH, (f) FeGe2 photoanode

before leaching with NaOH, (g) FeGe1 photoanode after leaching with NaOH, and (h) FeGe2 photoanode after leaching with NaOH.

According to the high-resolution XPS spectrum of the Ge 3d, for two films containing germanium, a shift of the spectra after the contact of NaOH solution has been observed. This shift can be related to the environmental chemistry of germanium, as seen in Figure 6.1, for lower concentrations of GeO_2 in lower temperatures occurs the presence of two phases, GeO_2 rutile, and $Fe_8Ge_3O_{18}$ and according to equation S1, the GeO_2 in the presence of OH^-, it reacts and forms a soluble complex, leaving only the germanium atoms that are inside the crystal lattice of hematite[2].

$$GeO_{2(s)} + OH^- \rightarrow HGeO_3^- \quad \text{(S1)}$$

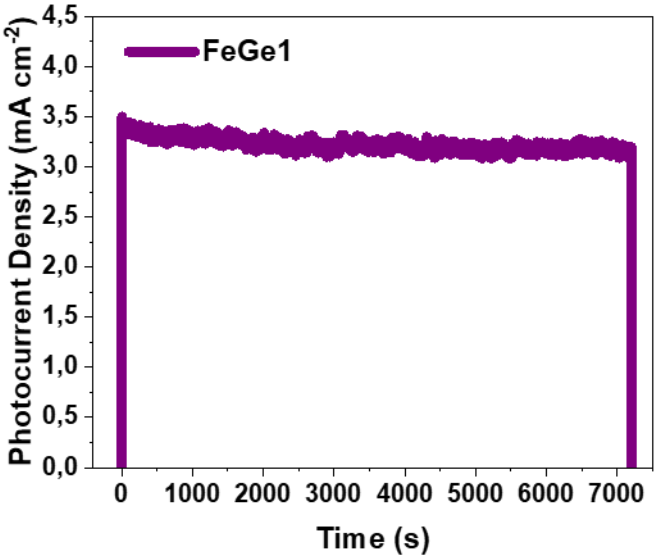

Figure 6.4. Chronoamperometry at an applied potential of 1.23 V_{RHE} under illumination (AM 1.5 – 100 mW cm^{-2}) for FeGe1 photoanodes in 1M NaOH electrolyte.

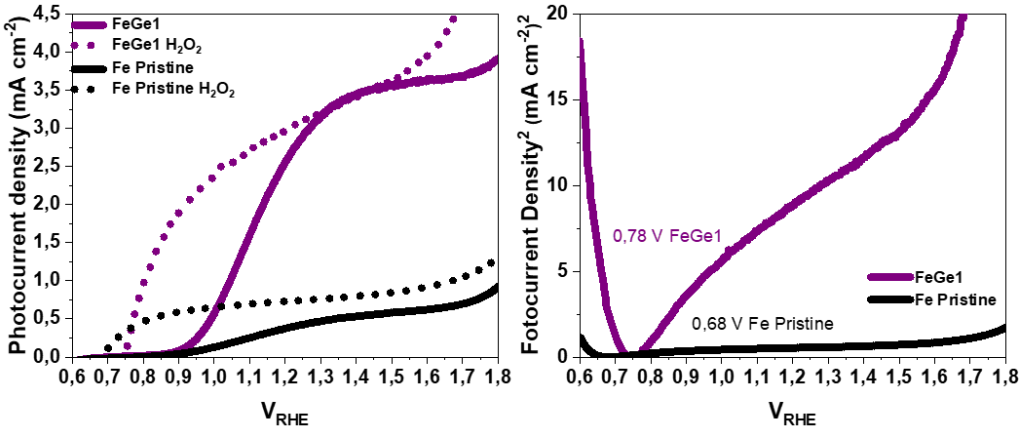

Figure 6.5. Photocurrent density x V curves under illumination for the Fe Pristine and FeGe1 films in 1M NaOH electrolyte with and without 0.5M H_2O_2.

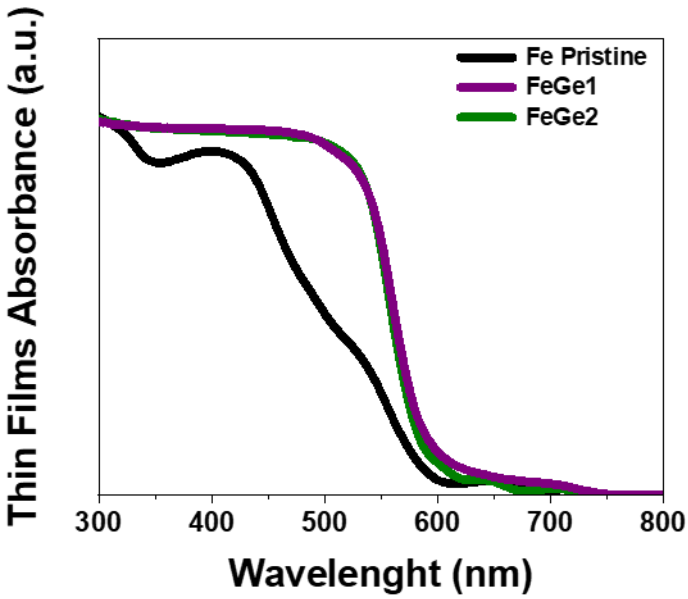

Figure 6.6. UV-Vis spectra of Fe Pristine, FeGe1, and FeGe2 films.

The width of depletion layer (W) can be calculated according the following equation:

$$W = \sqrt{\frac{2\varepsilon\varepsilon_0(V-V_{fb})}{qN_d}} \quad \text{(S2)}$$

where ε is the dielectric constant of hematite (80), V is the potential in RHE, V_{fb} is the flat-band potential, q is the elementary charge, and N_d is the donor density.

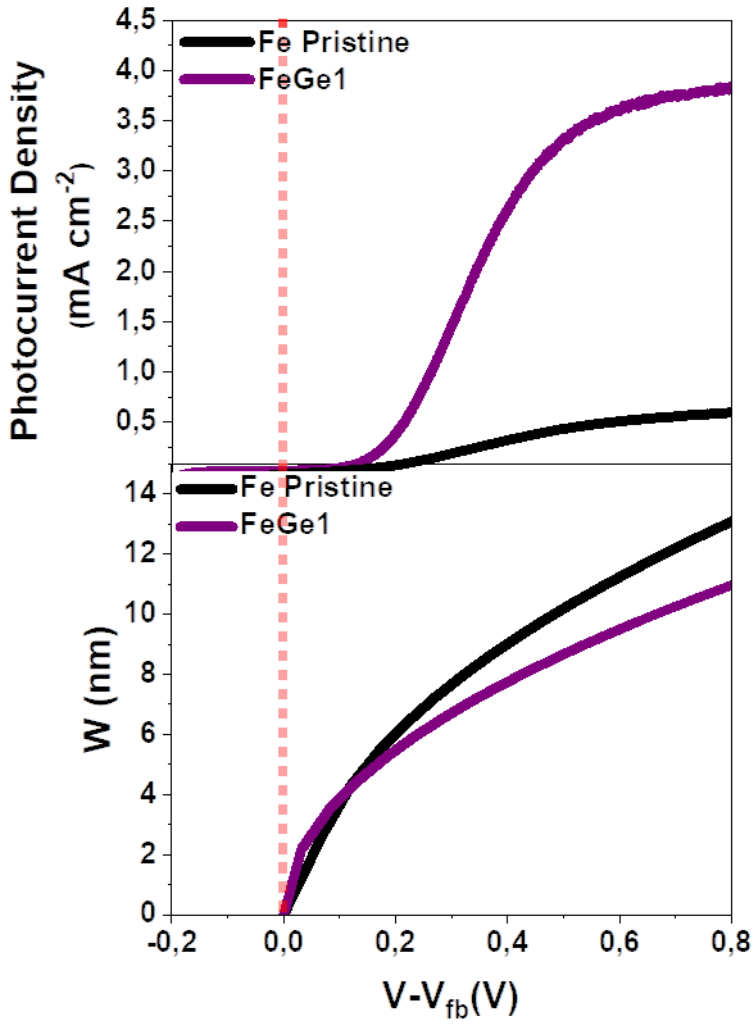

Figure 6.7. a) Photocurrent Density, and b) Depletion layer (*W*) as function of (V- V_{fb}).

References

[1] V. Agafonov, D. Michel, M. Perez, Jorba, M. Fedoroff, *Materials Research Bulletin* **1984**, 19, 233.
[2] O. H. Johnson, *Chemical Reviews* **1952**, 51, 431.